Resolving problematic luminescence chronologies for carbonate- and evaporite-rich sediments spanning multiple humid periods in the Jubbah Basin, Saudi Arabia

Laine Clark-Balzan[1*], Ash Parton[2,3], Paul S. Breeze[4], Huw S. Groucutt[5,6], Michael D. Petraglia[6]

[1] Institute for Earth and Environmental Sciences—Geology, University of Freiburg, Alberstr. 23-B, Freiburg im Breisgau, 79104, Germany

[2] Department of Social Sciences, Oxford Brookes University, Gibbs Building, Gipsy Lane, Oxford, OX3 0BP, United Kingdom

[3] Mansfield College, University of Oxford, Oxford, OX1 3TF, United Kingdom

[4] Department of Geography, King's College London, Strand, London, WC2R 2LS, United Kingdom

[5] School of Archaeology, Research Laboratory for Archaeology and the History of Art, University of Oxford, Oxford, OX1 2HU, United Kingdom

[6] Max Planck Institute for the Science of Human History, Kahlaische Strasse 10, 07745 Jena, Germany

*Corresponding author: laine.clark-balzan@geologie.uni-freiburg.de

Abstract

Most of the world's presently hyper-arid desert regions have experienced previous periods of significantly higher humidity and milder environmental conditions. The timing of these 'greening events' is critical to research upon global climatic fluctuations and for studies of hominin palaeodemography and range expansion, contraction, and extinction, but dating these climatic shifts via terrestrial sedimentary records can be difficult. Here, we outline the challenges inherent in the radiometric dating of carbonate- and evaporite-rich sediments preserved in the Jubbah basin (Nefud Desert, northern Saudi Arabia), a critical area for reconstructing the evolution of local hydrological regimes across long timescales. The Jubbah basin is surrounded by sandstone jebels (bedrock outcrops), which have prevented significant leeward dune accumulation for at least 400,000 years. The sedimentary sequences in the basin indicate repeated fluctuations between arid and humid climatic conditions, and provide key hydroclimatic records for northern Arabia. Quartz OSL and feldspar $pIRIR_{290}$ luminescence measurements and radiocarbon dating efforts are reported from four palaeoenvironmental sections in the Jubbah basin. Dates from sand-rich levels are relatively unproblematic, but significant difficulties

were encountered when calculating luminescence ages from carbonate and evaporite-rich sediments. Examination of the age-depth profiles, elemental composition, and sedimentological characteristics of these sections indicates that both secular disequilibrium and post-depositional alteration of the sediments has resulted in inaccurate dose rate assessment for multiple samples. In particular, we suggest that multiple groundwater pulses in the Jubbah basin have caused carbonate re-precipitation and concurrent uranium enrichment in subsurface deposits, whereas 'perched' sections (such as the carbonate-topped remnants reported elsewhere across the Nefud) seem to be free from such alteration. These difficulties highlight important considerations for the production of chronologies from comparable settings elsewhere. Careful evaluation of all results, however, yields a robust chronology indicating the presence of varying levels of groundwater from the Holocene, MIS 3, 5, and probably older sediments from MIS 7 through 9 or 11. We therefore provide a detailed discussion of the production of a reliable chronological framework for the Jubbah basin as an exemplar of the challenges to be overcome in such settings, and the amount of information that can be derived in so doing.

Keywords
Luminescence Dating; Quartz; Feldspar; Post-IR IRSL; Diagenetic alteration; Dose Rate

1. Introduction

Numerous recent studies focusing on the Arabian Peninsula have provided chronologically secure data for key archaeological (Armitage et al., 2011; Groucutt and Petraglia, 2012; Groucutt et al., 2015b; Richard P. Jennings et al., 2016; Petraglia et al., 2015), palaeontological (Stimpson et al., 2016), and palaeoecological and palaeoclimatic applications (Parton et al., 2015a; Rosenberg et al., 2013, 2011a). From these data, it is clear that multiple regions in the Arabian Peninsula have been considerably more humid in the past, with significant implications for biogeographical responses and population expansions into and through this region. Yet the timing and magnitude of the precipitation events related to such humid periods and their effects on the local and regional biogeography are still

known only in outline. Marine cores from the Arabian Sea (Caley et al., 2011; Des Combes et al., 2005; Ziegler et al., 2010), and speleothem records from Oman and Yemen (e.g. Fleitmann et al., 2003, 2011), have led to models of Late Pleistocene palaeoclimatic variability and environmental response at a regional scale (see Parton et al., 2015 for a full review). Alluvial, fluvio-lacustrine and aeolian records (Atkinson et al., 2011; Blechschmidt et al., 2009; Farrant et al., 2015; Parton et al., 2015a, 2013; Rosenberg et al., 2013, 2011a) have also provided insights into local hydroclimatic responses to arid-humid shifts, of significance for both human and animal range expansion and contraction, yet these records are spatially and temporally heterogeneous.

Regions that may have been important biogeographic corridors during humid periods, such as northern Saudi Arabia (Breeze et al., 2016), lack published high-resolution, terrestrial hydroclimatic archives bridging multiple humid periods. Sabhkas, low-lying areas with deposits of evaporites, carbonates, and clays that form due to repeated, short flooding events, may preserve useful proxies but have not been comprehensively studied in this region. Sedimentary records from the Tayma sabhka on the Western edge of the Nefud (Figure 1) have provided high resolution sedimentological data tracing the development of hypersaline conditions during the early Holocene humid period, however, there are no published pre-Holocene deposits at Tayma (Ginau et al., 2012). Extensive investigations in both the Nefud and the Empty Quarter (Rub' al Khali) sand seas have demonstrated that remnant Pleistocene palaeolake sediments are typically preserved as scattered outcrops of consolidated, carbonate-rich material found within interdunal basins (e.g. Rosenberg et al., 2011; 2013). These small sections, less than 0.5 m in depth to a rare maximum of nearly 3 m, range in age from the Early Holocene to at least MIS 11, however, examples of multiple stages of humidity in a single basin are infrequent (Rosenberg et al., 2013).

In this context, the Jubbah basin seems to be unique in the Nefud and possibly in Arabia as a whole (Whitney et al., 1983). Situated approximately 50 km from the southern margin of the Nefud

sand sea, this basin is bedrock-defined and thus protected from sand dune encroachment, with high potential for providing long-duration composite and/or continuous records that span multiple humid phases. Early investigations at Jubbah recorded a ca. 26 m composite section (Garrard et al., 1981) including clays, carbonates and sands. More recently, both radiocarbon dating and luminescence dating have provided data from disparate sections that indicate the presence of fresh water ecology during the Holocene (Crassard et al., 2013; Hilbert et al., 2014), while minor lacustrine deposits of Late Pleistocene age have also been reported (Petraglia et al., 2012). Several lithic scatters in the Jubbah area ranging in age from the Lower Palaeolithic (Shipton et al., 2014), through the Middle Palaeolithic (Groucutt et al., 2015a; Petraglia et al., 2012, 2011a), into the Epipalaeolithic (Hilbert et al., 2014) and Holocene (Crassard et al., 2013; Guagnin et al., 2017) also suggest that the basin provided an important and recurring long term water source in the region.

The sedimentary deposits in the Jubbah basin provide an important palaeoenvironmental record for the region. Providing a robust chronometric framework for these key sequences comprising evaporite and carbonate-rich, waterlain sediments, however, is not straightforward. Preservation of charcoals or plant macrofossils for radiocarbon dating is rare in this environment, and in any case this technique cannot be used for samples with an age greater than approximately 50-55 ka (Pigati et al., 2007). Uranium-series dating can be used to directly date lacustrine carbonates if they comprise a suitable closed system (Schramm et al., 2000). Such deposits are rare, though, with contamination and open-system behavior common in palaeolake deposits (Debaene, 2003). Photostimulated luminescence dating (Aitken, 1998), in which the burial age of sediment can be derived from the amount of absorbed energy in mineral grains, is currently the most generally applicable technique to the creation of long-range palaeoenvironmental frameworks in arid environments. This method utilizes ubiquitous quartz and feldspar grains as natural dosimeters and can potentially yield ages ranging from centuries to hundreds of thousands of years.

Dating long depositional sequences of waterlain deposits, while desirable from a palaeoenvironmental perspective, can cause several practical difficulties. First, luminescence signal saturation and age underestimation in quartz OSL dating have been encountered in multiple environments around the world. In the Arabian Peninsula, such underestimation can begin at signal levels as low as ca. 100 Gy, or ca. 50-75 ka given the environmental dose rates in this region (Rosenberg et al., 2011b). Feldspar minerals offer a brighter signal and thus may extend this age range potentially to several hundred thousand years (Huntley and Lamothe, 2001), but they are a complex mineral family, and have not yet been characterized for accuracy and precision in this region. Second, luminescence dating relies on accurate estimation of the average environmental dose rate during burial. In waterlain deposits, some of the assumptions generally used for such calculations may be invalid, due to chemical conditions at deposition (Krbetschek et al., 1994). Even more concerning is recirculation of groundwater through carbonate and evaporite-rich deposits, which can lead to significant post-depositional alterations (Dill, 2011).

In this study, we report investigations of the Jubbah basin as a high resolution palaeoenvironmental record spanning multiple humid periods. A chronometric framework including quartz and feldspar luminescence ages and radiocarbon dating results is developed for deposits from four palaeoenvironmental sequences, and we discuss the challenges entailed in this endeavor. Detailed sedimentological and palaeoenvironmental proxies will be discussed in a related publication.

2. Site Descriptions

The Nefud sand sea in northern Saudi Arabia is one of three connected sand seas, the others being the Rub' al Khali and Ad-Dahna, which together comprise approximately one-third of the land surface of the Arabian Peninsula. The Nefud itself is the second largest and most intensely studied of these, consisting of ~57,000 km^2 of predominantly barchanoid dunes in the south-west to western

regions and linear dunes elsewhere (Edgell, 2006). As shown in Figure 1A, it is bounded by Palaeozoic sandstones to the west, Cenozoic sandstones and limestones to the north, and Mesozoic formations to the east. To the south, the Nefud is bounded primarily by outcrops of the Palaeozoic Saq Sandstone formation. The Saq aquifer is one of the most important aquifers in the Arabian Peninsula, having been intensively utilized since the 1980's for agricultural development in a number of nearby provinces (Zaidi et al., 2015). The southern edge of the Nefud directly to the south of the Jubbah basin is bounded by the outcropping Precambrian Arabian shield, as well as some younger granitic plutons such as the Jabal Aja or Aja Massif (Kellogg and Stoeser, 1985).

The Jubbah depression itself is a large endorheic basin located near the southern edge of the sand sea (Figure 1B). Pale carbonate-rich sands and silty carbonates are exposed to the east of a string of outcropping Saq formation jebels running approximately N-S, which have prevented sand accumulation over an area measuring approximately 20 km long and 6 km wide. This primary basin occurs in the lee of Jebel Umm Sanman which rises ~200 m above the basin floor, but there are several smaller basins exposed at the base of other local jebels, such as in the lee of a line of jebels approximately 10 km to the southwest. Currently, the region receives less than 90 mm of precipitation annually (Edgell, 2006), and the wider region is classified as a desert (Bwh) according to the Köppen and Geiger climatic classification. The town of Jubbah itself, however, sustains a population of several hundred people and several dozen center point irrigation fields due to the lack of sand-cover and outcropping Saq formation in this region (Hussein et al., 1992). The Saq aquifer yields the only near-surface water resource for at least 50 km to the SE/SW and several hundred kilometers in other directions.

Between 2010 and 2013, the mapping, excavation and sampling of multiple palaeoenvironmental and archaeological sites within and surrounding the Jubbah basin was undertaken. New chronometric data is presented here for four palaeoenvironmental sections sampled during the

2013 season (Figure 1, Figures S1-S4): three of these are unpublished (JB1, 2, 3), and new data is presented from the previously published site of Al-Rabyah (ARY) (Hilbert et al., 2014).

Al-Rabyah (ARY): This site comprises a surface lithic scatter (approx. 200 m x 60 m) eroding from a low relief mound (Hilbert et al., 2014). A trench (8 x 1 m) excavated through this mound yielded a 2.5 m alternating sequence of discrete carbonate-rich and sand-rich sedimentary units, corresponding to lacustrine and palustrine deposition (Figure 1B, Figure S1). The trench was sampled for luminescence dating and sedimentological studies, and the recovered lithics were analysed (Hilbert et al., 2014). Published quartz multigrain ages for the sand-rich, carbonate-poor levels indicate that excavated levels were deposited between 12.2 ± 1.1 and 6.6 ± 0.7 ka. Stratified Epipalaeolithic artefacts were discovered in a unit with an age of 10.1 ± 0.6 ka. The capping carbonates were not originally dated but were thought to have been deposited soon after the underlying (ca. 6.6 ka) unit. Molluscan fauna were only recoverable from these upper carbonates; these point to the presence of a perennial, marshy water body.

JB1: This section was exposed at the base of a quarry adjacent to Jebel Ghawtar, one of the eastern jebels of the Jubbah basin (Figure 1B, Figure S2). Quarrying had exposed ca. 3 m sequence of gypsiferous, laminated sediments, and further excavations revealed a 9.5 m section, which was logged and sampled. The sedimentary sequence at JB1 comprises thick, greenish, heavily iron-stained clays with numerous root voids, overlain by coarse, poorly sorted sands and gravels. These are overlain by a series of interstratified calcareous silts, sands and marls occasionally featuring well-developed diatomite and gypsum lenses. The upper portion of the JB1 sequence displays increasing gypsum development, with the upper ca. 3 m comprising gypsiferous marls featuring well-developed, needle-like gypsum crystals. Marls and gypsum facies are finely interdigitated, with millimeter-scale laminations, particularly in the upper 2.5 m. Numerous organic-rich humic layers are also conspicuous throughout the upper ca. 3 m, with units featuring large quantities of plant and root impressions and locally calcified reed beds.

JB2: The JB2 section is located within the central Jubbah basin, approximately 5 km to the east of Jebel Umm Sanman (Figure 1B, Figure S3). Quarry excavations were extended to reveal a total depth of ca. 8.5 m of sediments, which were logged and sampled. The sedimentary sequence at JB2 is similar to JB1, having heavily iron-stained greenish clays at the base, overlain by greenish sands, and an interstratified sequence of marls throughout the lower ca. 4 m. Unlike JB1, however, these progress into well-developed gypsum beds and interdigitated gypsiferous marls from ca. 4 m, and they do not display the extensive evidence for vegetation development present at JB1. Gypsum crystals, however, are similarly well developed, though the fine marl/gypsum laminations present at JB1 are not seen in this section.

JB3: This section was identified as a consequence of road construction, in the environs of the archaeological site of Jebel Sanman-1 (JSM-1) (Petraglia et al., 2012) (Figure 1B, Figure S4). JB3 is located approximately 100 m east of JSM-1 and the base of the jebel. Recent quarrying had revealed nearly 2 m of horizontally stratified carbonate rich sands, silts, and diatomites, underlain by 20-30 cm of grey-brown sand. Although clearly horizontally bedded, the exposed sequence of sediments displays a distinct basinal structure indicative of a lake margin environment. The sequence at JB3 is underlain by a massive unit comprising well-sorted, fine-medium red sands indicative of aeolian deposition. These are overlain by an interstratified sequence of silts, muds, gypsiferous marls, diatomite, marls and silt-sands, with high concentrations of mollusc shells and shell fragments throughout the upper ca. 0.7 m.

3. Materials and Methods

3.1 Sedimentological Analyses

All four sections were excavated and logged in the field, with samples retrieved for further palaeoenvironmental analyses. A high-resolution study of these concerning lake development within the Jubbah basin is forthcoming. Analysis of carbonate content (LOI_{carb}) was conducted following the standard procedure described by Dean (1974) and Heiri et al. (2001).

3.2 Radiocarbon Dating

Seven samples from JB1 were submitted to the Oxford Radiocarbon Accelerator Unit (ORAU) for dating (Table 1). These comprised two charred plant macrofossils and five bulk sediment samples selected from layers found to be relatively rich in organic carbon by initial sedimentological analysis. Sample pretreatment and AMS protocols are described in Bronk Ramsey et al. (2002) and Ramsey et al. (2004). Uncalibrated radiocarbon dates are calculated using a half-life value of 5568 years and reported in radiocarbon years BP (AD 1950). Dates have been calibrated with the IntCal13 calibration curve (Reimer et al., 2013) via OxCal v4.2 (Ramsey, 2009).

3.3 Luminescence Dating

3.3.1 Sampling and Extract Preparation

Samples were collected by hammering segments of plastic or metal pipe into cleaned sections. Each tube was removed, and the ends were capped. Sediment samples for water content determination were also collected. Each section was sampled approximately every 50 cm, where possible. Visibly sand-rich units were preferred, followed by carbonate-rich units; visibly gypsum-rich units were avoided unless there were no alternate units to be sampled nearby. Detailed photographs of sample locations and surrounding sediments are included in the supplementary materials (Figures S1-S4). In total, we present ages or radioisotope concentrations for 10 samples from JB1, 11 from JB2, and 5 from JB3. From ARY, both quartz and feldspar results are presented for two unpublished samples, and feldspar results are given for the samples published in Hilbert et al. (2014).

All samples were transported to the Research Laboratory for Archaeology and the History of Art (University of Oxford) for preparation and measurement. Selected samples were opened and prepared in dim amber light (590 nm). Coarse grain quartz and feldspar was extracted according to the following methods. For samples collected from site ARY, 180-255 µm quartz was extracted according to the

methods previously used at this site (Hilbert et al., 2014); this procedure includes a hydrofluoric acid etch to remove quartz grains' alpha irradiated exteriors. Feldspars (125-180 and 180-255 µm) were concentrated by density separation (sodium polytungstate, $\rho = 2.58$ g cm^{-3}) after wet sieving, followed by hydrochloric acid (10%) treatment until reaction ceased, drying, and second sieving to remove any previously carbonate-coated grains < 180 µm in diameter. Sections JB1, JB2 and JB3 comprised much finer sediment with a high proportion of gypsum, therefore quartz (125-180 µm) and feldspar (180-255 µm) extraction was altered as described in Clark-Balzan (2016). Briefly, this procedure utilizes two density separations, $\rho = 2.35$ g cm^{-3} and 2.58 g cm^{-3}. Three mineral extracts are obtained: $\rho < 2.35$ g cm^{-3} (primarily gypsum, not discussed in this paper), 2.35 g cm^{-3}< $\rho < 2.58$ g cm^{-3} (feldspar), and $\rho > 2.58$ g cm^{-3} (quartz). The latter two extracts may not be pure if gypsum-coated quartz or feldspar is present, however, Clark-Balzan (2016) showed that luminescence signals from each mineral can be discriminated. Therefore, we refer to these extracts simply as quartz and feldspar in this study. Neither quartz nor feldspar grains collected from sites JB1, JB2, and JB3 were etched with hydrofluoric acid; this change in procedure both maximized the number of available grains from problematic gypsum-rich sediments, and removed concerns about heterogeneous etching and etch depth uncertainty.

3.3.2 Equivalent Dose Measurements

Due to the number of aliquots measured during this project, equivalent dose measurements for dating and residual estimates (ARY) were made on two luminescence readers, a Risø TL/OSL TL-DA-15 (Bøtter-Jensen et al., 2003, 2000) and a *lexsyg smart* (Richter et al., 2013) at the University of Oxford. Both machines incorporate automatic irradiation, optical stimulation, heating, and detection facilities. Full equipment details and measurement parameters, including illumination power, preheat parameters, and filters, are given in the Supplementary Material (Tables S1, S2). The dose recovery

experiment was performed with a *lexsyg smart* at the University of Freiburg; equipment details are identical to the Oxford *smart*.

Quartz equivalent doses (D_es) are derived from measurements made for 15 to 20 multigrain aliquots (2 mm diameter, unless otherwise noted). Luminescence signals were measured via a blue light stimulation, single aliquot regenerative protocol (Murray and Wintle, 2003, 2000), which included repeated (recycled) and zero dose steps, as well as an IR depletion step (Duller, 2003). Aliquots were preheated at 260 °C and 240 °C for 10 seconds after regeneration and test dose irradiations, respectively.

Ten multigrain feldspar aliquots (1 mm diameter) were also measured for each dating sample via the $pIRIR_{290}$ protocol of Thiel et al. (2011) if sufficient grains were present. In this protocol, the first IRSL bleach (50 °C) is intended to deplete the portion of the signal that may have been affected by anomalous fading, while the second, elevated temperature IRSL stimulation (290 °C) yields what is thought to be a more stable signal. Each SAR cycle also includes repeated and zero dose regeneration steps for quality control purposes. D_es for the calculation of luminescence ages are derived from the second stimulation ($pIRIR_{290}$). A dose recovery experiment was also conducted for sample JB1-OSL5. Sixteen aliquots (ca. 1-2 mm diameter) were bleached under an Osram Ultra-Vitalux lamp for 24 hours. Twelve aliquots were then beta irradiated (259 Gy), and the given laboratory dose was measured via the above protocol, with acceptance of aliquots and data analysis as described below. Remaining residual dose was measured from the other four aliquots.

Full $pIRIR_{290}$ signal resetting at deposition was investigated in two ways. We tested for the existence of an unbleachable $pIRIR_{290}$ signal by measuring a modern, aeolian-deposited sample from the Arabian Peninsula. This sample was collected from the top centimeter of the surface sand layer at Mundafan al-Buhayrah (see Groucutt et al., 2015 for site details). Coarse grain feldspars (180-255 µm) were extracted according to the ARY procedure described above, and twenty aliquots (1 mm diameter)

were prepared and measured. Aliquots were accepted for analysis as described below, but the zero ratio criterion was altered so that an aliquot was accepted if the normalized post-zero measurement was less than 0.4 Gy. Second, partial bleaching and the inheritance of a residual geological signal was tested. No modern depositional analogues exist in the Nefud, therefore D_es (IR_{50} and $pIRIR_{290}$) were calculated for feldspars from ARY and compared to quartz ages in an attempt to characterize possible partial bleaching in the Jubbah basin (see section 4.2.2 for further discussion).

Anomalous fading rates (IR_{50} and $pIRIR_{290}$) were measured from the ARY feldspars via the $pIRIR_{290}$ protocol according to the single aliquot regeneration method of Auclair et al. (2003). Three previously measured and accepted aliquots from each sample and each grain size were repeatedly dosed, preheated, and stored before signal measurement. Storage times ranged from immediate measurement to between 2 and 5 days for the longest storage period. For any given sample, no significant differences were noted between fading rates calculated for the two grain sizes, therefore all aliquots from each sample were grouped together to calculate final g-values. Fading-corrected ages have been calculated according to Huntley and Lamothe's (2001) procedure: sample-specific fading rates are used for samples from ARY, but an average $pIRIR_{290}$ g-value ($\mu \pm 1\ \sigma$) from all ARY feldspar aliquots was used to correct ages for samples collected from JB1, JB2, and JB3. Uncorrected ages are preferred; this will be discussed in section 4.2.2.

Luminescence signals were analysed via Luminescence Analyst v4.11. Due to the differing power outputs of the Risø and *lexsyg* LEDs (both blue and IR), signal integration ratios were adjusted for each machine so that approximately the same proportion of the total signal was used for the initial signal measurement. Late background subtraction was used for all analyses. Specific integration times are given in Table S2 (Supplementary Material). Aliquots were accepted for analysis if they met the following criteria:

1. A detectable net natural test signal greater than three sigma above the background signal,
2. Test dose error less than 20% of the calculated test dose,
3. Recycling ratios less than >10% from unity or overlapping with unity at an uncertainty level of 2σ,
4. The calculated zero-ratio less than 5% of the magnitude of the normalized natural signal (L_N/T_N) [quartz and feldspar] or not indistinguishable from 0 at an uncertainty level of 2σ [quartz only]. This is discussed in Clark-Balzan (2016);
5. The IR depletion ratio greater than 90%, or indistinguishable from unity at an uncertainty level of 2σ [quartz only].

These criteria are sufficient to reject aliquots with a signal dominated by gypsum luminescence, as shown in Clark-Balzan (2016). Sample D_es and overdispersion values were calculated from accepted aliquots using the central age model (Galbraith et al., 1999). For a few samples (see results and discussion), the minimum age model has also been applied (Galbraith et al., 1999).

3.3.3 Dose rates

All dose rates have been calculated with DRAC, the 'Dose Rate and Age Calculator' (Durcan et al., 2015; Durcan and King, 2017). Measurement procedures and assumptions for all user-input values are described in this section. Portions of each sample, including several that were not subsequently dated, were submitted for fusion ICP-MS (Activation Laboratories, Ltd., Canada) in order to obtain uranium, thorium, and potassium concentrations. External beta dose rates were calculated from these concentrations (5 % relative standard error, 'RSE') using the dose rate conversion factors of Guerin et al. (2011) and grain size attenuation factors for quartz and feldspar from Guérin et al. (2012). No external rubidium dose rate was calculated. External alpha dose rates were also calculated from the conversion

315 factors in Guerin et al. (2011), with grain size attenuation values from Brennan et al. (1991). Coarse-
316 grain alpha-efficiency factors (a-values) of 0.10 ± 0.02 and 0.15 ± 0.05 were used for quartz (Olley et al.,
317 1998) and feldspar (Balescu and Lamothe, 1994), respectively, following common practice in the
318 luminescence community (Durcan et al., 2015). For etched quartz grains (samples ARY-OSL4 and ARY-
319 OSL5), the external alpha dose was considered to be zero; the beta attenuation factors were adjusted by
320 assuming a 10-20 µm etching depth and calculated based on Brennan (2003). Potassium feldspars also
321 include an internal dose rate, arising from potassium and rubidium contained within the crystal matrix.
322 This proportion of the dose rate was calculated assuming each grain contains by mass 12.5 ± 0.5 %
323 potassium (Huntley & Baril, 1997) and 400 ± 100 ppm rubidium-87 (Huntley and Hancock, 2001).
324 Gamma dose rates were measured on site for all but one sample (ARY-OSL4), utilizing an Inspector 1000
325 gamma spectrometer. This spectrometer was calibrated using the doped concrete blocks at the
326 University of Oxford (Rhodes and Schwenninger, 2007), and dry gamma dose rates were calculated via
327 the threshold technique (Duval and Arnold, 2013; Mercier and Falguères, 2007), then corrected for on-
328 site water content. A 5 % RSE was used for all dry gamma dose rates. For sample ARY-OSL4, the
329 gamma dose rate was calculated from the measured elemental concentrations, with Guerin et al. (2011)
330 conversion factors. Cosmic dose rates are calculated using the modern day burial depths and sediment
331 overburden density of 1.8 ± 0.1 g cm^{-3}.

332 Present day water contents (%, $mass_{water}/mass_{wet\ sediment}$) were measured by weighing water
333 content sediment samples before and after oven-drying (at least 48 hours, 60 °C). Average water
334 content values during burial were then assigned in two groups: if the present day water content was
335 <5%, a 5 ± 3 % average value was used, if >5%, a 10 ± 3 % value was used. These values were chosen to
336 reflect higher water content during humid periods, but also to include heterogeneity in the moisture
337 content of the sections due to varying porosity and the influence of the complex ground water system in

the Jubbah region. Dose rate corrections were then calculated using the factors from Zimmerman (1971) and Aitken and Xie (1990).

4. Results and Discussion

4.1 Radiocarbon Dating

Six of seven samples failed due to low radiocarbon yield (Table 1). The only successful sample (OxA-30943), collected from 2.65-2.68 m depth in section JB1, yielded an uncalibrated age of 7925 ± 45 ^{14}C years BP. When calibrated via the 'IntCal13' curve (Reimer et al., 2013) using OxCal v4.2 (Ramsey, 2009), this sample dates to 8980-8609 calBP (95.4% range).

Several factors may affect the accuracy of this radiocarbon date as an estimator for the depositional age of its sedimentary unit. First, it is possible for a sample to physically move within the sediment after deposition. The dated sample, a charred plant fragment, was extracted from a distinct, dark grey organic-rich layer, approximately 3 cm thick. This region of the section consists of finely interdigitated marls and organic silts, with preservation of laminations on the scale of millimeters to centimeters and numerous plant remains. No visible evidence for bioturbation was apparent. Secondly, macrofossils from woody plants may overestimate sediment age by more than 1000 years, both because they may include much older material (up to several centuries) within their inner rings whilst living and because they may remain in the landscape for significant periods of time prior to burial (Oswald et al., 2005). Though the plant-type of the charred macrofossil could not be identified, it is highly improbable that such long-residence woods would have existed in the Nefud during the Holocene (Hoelzmann et al., 1998; Watts & Al-Nafie, 2014). Finally, and most importantly in this environment, there may be a freshwater reservoir effect due to the existence and uptake of 'ancient' carbon, depleted in ^{14}C, by plants within the Jubbah basin. Both the Saq sandstones and extensive Jubbah basin carbonate beds may function as sources of ancient carbon, and indeed the Saq Aquifer pore water has yielded a

radiocarbon age of 20,400 ± 500 14C years (Thatcher et al., 1961). The influence of this sedimentary carbon depends upon whether the plant has fixed carbon from the groundwater; fully submerged and emergent (submerged roots, some vegetation above water surface) plants will uptake different proportions of this older carbon (Marty and Myrbo, 2014), while terrestrial plants fix atmospheric carbon and will not be affected by such a reservoir (Grimm, 2011; Bronk Ramsey et al., 2012). As the plant-type has not been identified, some age overestimation due to a localized reservoir effect is possible. Finally, contamination by modern carbon, which may cause an age underestimate, is highly unlikely given the young age of this sample and the pretreatment used. Overall, in our estimation, this radiocarbon date is likely an accurate estimate of the age of sediment deposition at 2.65-2.68 m depth in JB1, with some possibility that it may overestimate the true age by up to a few centuries.

4.2 Luminescence Dating

4.2.1 Quartz Characteristics

High proportions of aliquots (up to 13 of 20, 65%) were rejected for insufficient test dose signal or high test dose error in samples with a high gypsiferous content (e.g JB2-OSL4) (Table 2a). A further, typically low but sometimes significant, number of aliquots has been rejected by the IR depletion criteria and probably contained feldspars (e.g. JB3-OSL3). Relatively few aliquots, however, were rejected for either recycling or zero ratio criteria. We conclude that the rejection criteria are appropriately excluding aliquots from which the measured luminescence signal is not emitted by quartz grains, and that this protocol and the similar SAR OSL protocols used in other studies in the region (Petraglia et al., 2011; Petraglia et al., 2012; Crassard et al., 2013) are appropriate for the extracted quartz.

Two dose regeneration curves are presented in Figure 2, one of which saturates at a typical level for the Jubbah basin, and one that saturates at a much higher dose. For the samples presented here, at least one saturated aliquot is present in all samples with a population CAM D_e > 200 Gy. Yet a number

384 of individual aliquots have been measured that yield D_e estimates in the range 400-500 Gy without
385 saturation. The highest measured sample CAM D_e, 288.62 ± 41.24 Gy (JB1-OSL4), yielded only three
386 aliquots rejected due to signal saturation. By contrast, multigrain and single grain quartz OSL
387 measurements from Mundafan Al-Buhayrah in the Empty Quarter (Groucutt et al., 2015), Jebel Faya
388 (Armitage et al., 2011), and even neighboring sites in the Jubbah Basin such as JQ-1 and JKF-1 (Petraglia
389 et al., 2011; 2012), yield grains and aliquots that saturate at much lower levels. These differences may
390 be due to variable grain sources, but the majority of sands from both the Nefud and Empty Quarter
391 seem to be derived primarily from weathering of Palaeozoic sandstone formations (Garzanti et al.,
392 2012).

393 Overdispersion values for the Jubbah sites vary between ca. 10 and 60%, with a majority of
394 values < 36% (Table 3). Overdispersion values > 36% are measured only for the lower carbonate from
395 Al-Rabyah (ARY-OSL5) and the three carbonate-rich samples from JB3 (JB3-OSL1 – JB3-OSL3).
396 Comparative overdispersion values for quartz grains from the Arabian Peninsula are relatively scarce.
397 Petraglia et al. (2011) measured values between 24 ± 3% and 29 ± 4% for small aliquots (ca. 50 grains)
398 from both a calcrete and palaeosols, and Rosenberg (2013) calculated overdispersion values between
399 12% and 28% for a suite of primarily aeolian quartz multigrain samples (unknown aliquot size) from the
400 Nefud. D_e distributions tend to by symmetric, with only three sample populations yielding positive
401 unweighted skewness values greater than 1. Both high overdispersion and skewness are present only in
402 aliquot populations ARY-OSL5 and JB3-OSL2 (Figures 6,7), which have overdispersion values of 49 and
403 57%, respectively. This combination of characteristics is likely due to the inclusion of partially bleached
404 quartz grains within these samples (Olley et al., 2004), in which case the minimum age model can be
405 used to extract the D_e corresponding to the most fully-bleached grains (Galbraith et al., 1999). The use
406 of the minimum age model will be discussed further in section 4.2.3.

407 **4.2.2 Feldspar Characteristics**

Feldspar aliquots measured from Jubbah basin sites were rejected primarily for low intensity luminescence signals (ARY) and zero ratio magnitude (JB1-3) (Table 2B). Half or more of the measured aliquots were rejected from samples ARY-OSL3, ARY-OSL7, JB1-OSL2, JB1-OSL3, JB3-OSL4, and JB1-OSL6 due to one of these criteria. Feldspar aliquots measured from other sites in the Nefud desert are rarely excluded by these criteria (e.g. 4 per 69 aliquots, in prep.) . Aliquots failing either criterion may comprise a significant proportion of gypsum-coated grains; investigation of mineral extracts from several of these samples indicated significant gypsum contamination, and the gypsum signal is both dim and characterized by significant thermal transfer (Clark-Balzan, 2016). Feldspar aliquots that passed both criteria were bright, with good recycling ratios. The natural $pIRIR_{290}$ signal is in saturation for multiple measured aliquots, including nearly half of those measured from sample JB1-OSL13 (Figure 4). Dose recovery results suggest that the $pIRIR_{290}$ protocol is generally suitable for these samples: a central age model D_e of 0.92 ± 0.05 (normalized by the given dose) was recovered from 11 accepted aliquots. Residual measurements were not considered to be reliable, as signal magnitudes for three of four aliquots were similar to the normalized zero-dose response. Individual aliquots in the dose recovery experiment are quite dim, and we think it is likely that feldspars in this highly gypsiferous sample were measured at essentially a single grain level.

Minimum fading rates measured from individual ARY aliquots are indistinguishable from zero for both IR_{50} and $pIRIR_{290}$ signals. IR_{50} g-values range up to a maximum of 20.13 ± 3.09 %/decade, with an average value of 5.63 ± 4.46 %/decade (μ ± 1σ) calculated from all measured aliquots. The $pIRIR_{290}$ signal yields much lower fading rates, with a maximum individual aliquot g-value equal to 4.81 ± 0.49 %/decade, and an average of 1.84 ± 1.32 %/decade. G-value distributions for all measured ARY aliquots can be seen for both signals in Figure S5. Such fading values are within the ranges reported in other publications for both IR_{50} and $pIRIR_{290}$ signals (see review by Li et al., 2014).

The implication of low (< 2%/decade) g-values for the $pIRIR_{290}$ signal is still under debate. Several studies have reported measurement of field saturated $pIRIR_{290}$ signals, even though finite fading values can be detected in the laboratory (Buylaert et al., 2011; Thiel et al., 2011a; Thomsen et al., 2011). Similarly, quartz grains, though apparently not suffering from signal fading in nature, yield a 1%/decade g-value when measured via standard fading tests (Buylaert et al., 2012). Buylaert et al. (2012) therefore propose that fading rates of 1-1.5% are artifacts of the measurement process. Fading-corrected $pIRIR_{290}$ ages also seem to overestimate quartz luminescence ages in some cases (Buylaert et al., 2011; Kars et al., 2012), and Li et al. (2014) suggest that many uncorrected $pIRIR_{290}$ ages (70-80% of those compiled) agree with independent age control within a two sigma range. Given that the average $pIRIR_{290}$ g-value measured in this study is less than 2 %/decade, and that up to 44% of accepted aliquots from one of the oldest samples measured are in saturation (JB1-OSL13), we suggest that $pIRIR_{290}$ equivalent doses should not be corrected for anomalous fading. In this, we follow the convention of a number of $pIRIR_{290}$ feldspar dating studies (Roskosch et al., 2012; Thiel et al., 2012, 2011b). Given the complexity of this issue (see for example Lowick et al., 2012), however, we also provide fading-corrected ages in Table 6 for the readers' information.

We have attempted to estimate the magnitude of any $pIRIR_{290}$ residual signal due to partial bleaching in these primarily low-energy, waterlain deposits. Such a residual may comprise both a fully unbleachable component (Buylaert et al., 2011), and an inherited geological signal due to the relative slowness of $pIRIR_{290}$ signal bleaching (Buylaert et al., 2012; Murray et al., 2012). Measurements of modern, aeolian-deposited feldspars from the Arabian Peninsula suggest a low magnitude for any unbleachable signal: D_es of only 0.39 ± 0.05 Gy and 1.07 ± 0.10 Gy were measured for IR_{50} and $pIRIR_{290}$ signals, respectively (Tables 2,3). These distributions have relatively high overdispersion values, with the former yielding a value of 43.80 ± 10.72 % and the latter 40.41 ± 6.94 % (Figure 5A). This estimate agrees well with the low residuals collated and published by Buylaert et al. (2012) from other coarse

455 grained, modern samples. Kars et al. (2014) have also found that residual doses continue to decrease
456 even after 2 to 11 days of bleaching with a solar simulator, suggesting that any residual measured after
457 two days of laboratory bleaching (see for example Preusser et al., 2014) is not likely to accurately
458 estimate the magnitude of a truly unbleachable signal, and Thiel et al. (2011) have also preferred not to
459 subtract laboratory-measured residuals from $pIRIR_{290}$ D_es.

460 No modern depositional analogies were available in the studied region, however, the quartz OSL
461 chronology obtained by Hilbert et al. (2014) allowed us to calculate feldspar $pIRIR_{290}$ residuals due to
462 geological signal inheritance (Table 4). Expected D_es (both internal and external) were calculated for
463 each sample based on the quartz D_e and OSL age obtained for the same sample. In the case of sample
464 ARY-OSL5, for which the luminescence age is likely underestimating the depositional age of the
465 sediment (see Section 4.2.3), we have instead used the average quartz age from samples ARY-OSL3 and
466 ARY-OSL7 to calculate the expected feldspar dose. Equivalent doses and final ages calculated via the IR_{50}
467 (fading corrected and uncorrected) and $pIRIR_{290}$ signals (fading corrected and uncorrected, uncorrected
468 preferred) are presented in Table 3. It is evident that for both IR_{50} and $pIRIR_{290}$ signals, the 180-255 µm
469 fraction yields lower equivalent doses than the 125-180 µm fraction. Several causes might explain this
470 systematic difference. First, it may be due to the differing numbers of grains on the measured aliquots,
471 with multigrain signal averaging of partially bleached single grain D_e populations producing
472 systematically different results. Second, it is possible that the size fractions comprise slightly differing
473 mineralogies with varying internal K-content, and these variable dose rates yield different D_es over time.
474 Third, a real difference in the bleachability of the grains may be indicated. Several other studies have
475 also reported better bleaching for coarser grains in both aeolian (Buylaert et al., 2011) and fluvial (see
476 review by Rittenour, 2008) depositional settings, which are likely due to differences in sedimentological
477 transport regimes. The calculated residuals for ARY range from 6 to 29 Gy for the 180-255 µm grains,
478 and 7 to 45 Gy for the 125-180 µm grains. The magnitude of the residuals does not precisely correlate

with expected partial bleaching as inferred from the quartz D_e distributions (Olley et al., 2004; Hilbert et al., 2014), but there seems to be some correlation. Nor do higher feldspar overdispersion values correlate with higher residual signals, suggesting that high overdispersion values in feldspars cannot necessarily be used to suggest the presence of partial bleaching (Figure S6). In all cases, measured residual D_es are below 50 Gy.

Poor bleaching of the feldspar $pIRIR_{290}$ signal in waterlain sediments has been noted in both coastal (Reimann et al., 2011) and lacustrine environments (Buylaert et al., 2013), with inherited signals of hundreds of grays measured in laboratory experiments simulating such conditions (Lowick et al., 2012). The magnitude of the residual signal measured in waterlain deposits for the Jubbah basin is quite variable between samples, however, the maximum measured value of ca. 50 Gy becomes negligible for older samples over the timescales considered. We do not subtract any residual correction factor from our measured $pIRIR_{290}$ D_e values, as the dominant residual component is likely to be the inherited geological signal.

Overdispersion values measured for 180-255 µm feldspars ($pIRIR_{290}$ signal) range between approximately 20 % and 60 % for samples with four or more accepted aliquots (Table 3, Figure 5). There is no clear relationship with either the samples' central equivalent dose or calculated age. Interpreting the meaning of these values is difficult and beyond the scope of the current paper as, unlike quartz, feldspar overdispersion values result from a convolution of variance in fading rate, internal dose rate variations, and residual doses, in addition to shared sources of variability such as bioturbation, residual doses due to partial bleaching, and microdosimetric effects. External microdosimetry has a small effect on coarse feldspars due to their relatively high internal dose rates, however, and fading rate variations should also be low, given the use of the $pIRIR_{290}$ methodology. Therefore, we expect primary drivers of these overdispersion values to be related primarily to variations in partially bleached residual doses,

internal dose rate variations, and possibly bioturbation. We will discuss these possibilities further in section 4.2.3.1.

4.2.3 Accuracy and Reliability of luminescence ages

Luminescence ages are presented for each of the four sections (Table 6, Figures 8 and 9). Two key observations are apparent:

1. Age depth reversals are present in all study locations, and for all mineral types (where there is more than one sample measured for comparison),
2. Independent age control via radiocarbon dating at 2.65-2.68 m for section JB1 suggests that the bracketing luminescence dating samples (JB1-OSL1, JB1-OSL2) underestimate deposition age by several thousand years.

These observations may be explained by either sample/site specific inaccuracies in the determination of equivalent doses or a failure of the standard dose rate calculation assumptions. Each of these possibilities will be discussed in turn.

4.2.3.1 D_e estimation

The effects of equivalent dose determination upon age calculation are perhaps the most often discussed reasons for unexpected luminescence age results, either in the form of age reversals with depth or offsets from independent age controls. Population D_es may yield inaccurate ages due to the use of inappropriate measurement parameters (e.g. preheat temperatures, see Murray and Wintle (2003)), inheritance of a residual geological signal ('partial bleaching') (Galbraith et al., 1999; Stokes et al., 2001), physical mixing of depositional units (Gliganic et al., 2015; Hanson et al., 2015), age underestimation due to signal saturation (Duller, 2012), or anomalous fading (Huntley and Lamothe, 2001; Wintle, 1973). We have already discussed the measurement parameters for both quartz and feldspar, and concluded that there is no evidence for a systematic inaccuracy in D_e estimation due to this

525 cause. Anomalous fading of the $pIRIR_{290}$ signal used for age calculations has also been considered and
526 assumed to be negligible (see section 4.2.2). The other issues will be discussed further here.

527 Partial bleaching

528 Partial bleaching refers to incomplete resetting of the OSL/IRSL signal during transport and
529 deposition of mineral grains (Huntley et al., 1985). The absolute magnitude (in gray) of a residual (post-
530 bleaching) signal will depend upon the magnitude of the grain's original equivalent dose, bleaching
531 stimulation intensity and wavelength, duration of bleaching, and the mineral's characteristic crystal
532 properties (Aitken, 1998; Spooner, 1994). Many of these properties are controlled by geomorphic
533 transport processes, as variations in stimulation duration, intensity, and spectrum are determined by
534 the mode of grain transport. In general, aeolian transport should result in the most complete bleaching
535 (Stokes, 1992), though it is possible to imagine scenarios such as dust/sand storms that might result in
536 deposition of incompletely bleached grains. For waterlain sediment, water depth and turbidity strongly
537 affect the amount and wavelength of electromagnetic radiation incident upon the grains, with grains
538 deposited by fast-flowing, murky waters much less likely to be fully bleached than grains transported
539 through clear, shallow waters (Berger, 1990). Mineral characteristics will also have a strong effect on
540 residual doses for a given depositional environment. Experimental sunlight bleaching of quartz causes
541 the photo-stimulated luminescence signal to decrease to a negligible level within seconds to minutes,
542 whereas feldspar may retain a significant fraction of its original signal after multiple hours of bleaching
543 (Godfrey-Smith et al., 1988). Elevated temperature infrared stimulation of feldspar, which allows de-
544 trapped electrons to enter higher energy band-tail states and recombine at luminescence centers
545 physically separated by larger distances within the crystal, allows measurement of a signal less prone to
546 anomalous fading, with the increase in temperature providing a concomitant increase in signal stability
547 (Jain and Ankjærgaard, 2011; Jain et al., 2014). The same physical process, however, results in slower

548 bleaching of elevated temperature IRSL stimulation, which may result in a high geological residual for
549 feldspar crystals (see discussion and references in section 4.2.2).

550 The four study locations preserve a variety of depositional environments. Basal clayey silt-sands
551 underlying JB1 and JB2 likely represent undisturbed deposition in still water conditions and the
552 dissolution of underlying bedrock material of the Saq sandstone. These units are also free from large
553 gravel clast inclusions, interbedding or significant bioturbation. The overlying very poorly sorted, coarse
554 sub-angular-subrounded gravelly and granulitic sands at both sites reflect the mobilization and
555 deposition of weathered material from the adjacent jebels. As such, it is possible that samples from
556 basal clayey or gravelly deposits may be affected by partial bleaching. At JB3, basal sands are very well
557 sorted with no signs of vegetation development, clast inclusions or bedding and are suggested to be of
558 aeolian origin. Dated samples have been collected primarily from overlying palustrine and lacustrine
559 contexts. Higher gypsiferous and carbonate units are likely to represent low energy waterbodies with
560 fluctuating extents and depths, typical of endorheic and seasonally variable water bodies; sedimentary
561 and palaeoecological data has been published from Al-Rabyah (Hilbert et al., 2014) and analogous site
562 JQ-200 (Crassard et al., 2013). Given the low energy setting and a lack of discernable fluvial input into
563 the water bodies, the overall probability of partial bleaching should be low in these upper units,
564 however, there is potential for the input of partially bleached mineral grains resulting from erosion of
565 the local jebels or during mass movements of sandy layers in unusual storm events. The presence of
566 wavy fine laminations of marls and gypsum throughout the upper ca. 2 m of JB1 are likely to be
567 indicative of lacustrine wave action or subaerial aeolian scour. In addition, if seasonal rainfall variability
568 were to result in lake desiccation and large-scale deflation of surface material, the subsequent
569 reworking of sediments might result in partial bleaching. It is noted, however, that there is no physical
570 evidence for substantial desiccation (i.e. curling of marl beds) within any of the sedimentary sequences

571 at Jubbah. It is likely that the presence of fine to medium sand grains within lacustrine units reflect the
572 transport and deposition of aeolian material into often shallow, low energy water bodies.

573 Two samples share some luminescence features indicative of partial bleaching in measured
574 quartz distributions. The first of these is sample ARY-OSL5, the age of which has already been closely
575 bracketed to between 11.4 ± 0.8 ka and 12.2 ± 1.1 ka by OSL ages on sand-rich units above and below
576 (Hilbert et al., 2014). The quartz D_e population measured for ARY-OSL5 is both highly scattered (σ = 57.3
577 ± 12.3%) and positively skewed, which suggests that these grains may be partially bleached (Figure 6).
578 MAM-calculated ages, however, underestimate the previously estimated depositional age, if an average
579 overdispersion for well-bleached samples from the site is used (20%, see Hilbert et al., 2014): the D_e of
580 ARY-OSL5 becomes 17.94 ± 2.50 Gy and the final age 5.4 ± 0.8 ka (see Figure S7 for D_e dependence on
581 assumed overdispersion). The CAM age (11.2 ± 2.0 ka) is stratigraphically consistent. There are two
582 possibilities that may explain the offset between MAM ages and stratigraphy. The first is that the CAM
583 D_e more accurately represents the appropriate D_e for input into the age equation. This would be the
584 case if the skewed and overdispersed population were the result of microdosimetric variations in the
585 sediment, and indeed skewness and overdispersion are known consequences of heterogeneous beta
586 radiation (Nathan et al., 2003; Mayya et al., 2006). This and other studies (Petraglia et al., 2011; Hilbert
587 et al., 2014) of analogous deposits in the Jubbah basin, however, show the magnitude of the multigrain
588 OSL overdispersion and skewness is highly unusual for similar Holocene deposits. Therefore, this does
589 not seem to be the most likely cause. Second, we can observe that the uranium concentration in this
590 unit is nearly four times that of the upper carbonate, and thus it contributes ca. 86% of the beta dose
591 rate to quartz grains (as calculated via modern elemental concentration). We suggest that this sample
592 does contain partially bleached quartz grains, making the minimum age model a more appropriate
593 choice, and that the stratigraphic reversal in the ages is instead due to an overestimation of the dose
594 rate. This will be discussed further in the next section. Second, as noted previously, all three samples

595 collected from JB3 carbonates have unusually high overdispersion values in the context of the Jubbah
596 basin samples. Assuming that partial bleaching can be identified by a combination of positive skewness
597 and high overdispersion, it was suggested that the luminescence age for sample JB3-OSL2 should be
598 calculated from the MAM D_e. By analogy with the underlying sand, and given the high overdispersions
599 of quartz from the bracketing samples, we suggest an overdispersion value of 30%, which yields a MAM
600 D_e of 55.00 ± 6.32 Gy with approx. 80% of aliquots fully bleached.

601 Considering the evidence for partial bleaching in the measured $pIRIR_{290}$ feldspar distributions, it
602 seems likely that some partial bleaching may occur on a sample-specific basis (e.g. JB1-OSL2).
603 Measurements on the modern, aeolian sample MUN-BLEACH13 indicated that a systematically
604 unbleachable residual would be ca. 1 Gy, which is negligible. ARY quartz and feldspar comparisons,
605 though, suggested that partial bleaching at deposition could lead to inherited signals of variable
606 magnitude, up to ca. 50 Gy. The same ARY data shows that distinguishing partially bleached samples via
607 distribution parameters is quite difficult. Several samples with significant residual signals (e.g. ARY-OSL3
608 and ARY-OSL7) yielded symmetric and well-grouped D_es, with overdispersion values below 10% (Figure
609 S6). By contrast, overdispersion values of 20-40 % are common for samples known to be well-bleached
610 or fairly well-bleached (Figure 5), including the modern aeolian sample, ARY-OSL2 (180-255 µm fraction),
611 and JB1-OSL3, JB1-OSL4, and JB1-OSL5 (with similar feldspar and quartz D_es). Therefore, we suggest that
612 identification of poorly bleached samples via overdispersion is not straightforward. Nevertheless, we
613 will consider the potential effects of partial bleaching for feldspar samples with overdispersion values
614 >40 % in section 4.3.

615 Generally low overdispersion and skewness values for quartz and feldspar partial bleaching
616 residuals confirm that partial bleaching is unlikely to be a significant, systematic issue in the Jubbah
617 basin. Most samples have low overdispersion values in the Holocene (around 20% or less) and
618 acceptable values for the measured Pleistocene units (30-40%). Moreover, there is no correlation

between overdispersion magnitude and the age-depth reversals apparent in sections JB1 and JB2 for either quartz or feldspar; that is, if the reversals in the sediments are due to partial bleaching, the 'overestimated' upper ages should have higher overdispersions. Finally, feldspar and quartz ages overlap at 1 sigma for two of four samples dated by both methods from section JB1, though some partial bleaching is clearly possible for the $pIRIR_{290}$ signal based on the JB1-OSL2 feldspar age.

Physical Mixing

Vertical sediment mixing through desiccation cracks in marl beds, insect and/or animal burrowing activity, or vegetative bioturbation may increase overdispersion values and cause age over- or underestimation. No visible evidence for substantial mixing of sedimentary units has been noted at any of the four sections, though root voids are present in some units at JB1 and ARY (Figures 8, 9). Horizontally bedded units are visible in each section, with clear and distinctive separation of carbonate-rich and sand rich-units (Figures S1-S4). Millimeter-scale wavy beds of small gypsum crystals are also apparent in units 18 to 22 at JB1. These are typically comprised of a few millimeters of fine calcareous silts, coupled with euhedral and prismatic to lenticular crystals that are laterally contiguous horizontally over the investigated area (several meters wide), with no evidence for post-depositional disturbance. Extremely delicate carbonate casts of reed beds have also been preserved in the upper 4 m of JB1. Mixing in basal sandy clay units is possible, due to root penetration or burrowing, particularly if significantly younger lake deposits formed above an older base. This is more difficult to rule out visually, and must be considered a possibility.

Saturation effects

Due to the length and age of the sampled sediments, underestimation of absorbed dose due to saturation of aliquots must be seriously considered as a potential confounding factor for D_e measurements. In particular, Rosenberg et al. (2011) and Groucutt et al. (2015) have suggested that

642 quartz multigrain aliquots from the Arabian Peninsula measured with a standard SAR OSL protocol may
643 systematically underestimate D_es greater than ~100 Gy. Sections JB1 and JB2 already yield saturated
644 quartz aliquots by 4 m depth: samples JB2-OSL5 and JB1-OSL5 yield 5 and 4 saturated aliquots,
645 respectively, from 18 each measured. This was a motivating factor for the measurement of both quartz
646 and feldspar grains from samples JB1-OSL1 through JB1-OSL5: because the feldspar signal saturates at a
647 much higher level (in this study near 1000 Gy), feldspar D_es should continue to grow normally even as
648 the quartz begins to saturate. Any underestimation by the quartz D_e measurement protocol would
649 therefore be apparent as a systematic offset between the quartz and feldspar ages. It is apparent from
650 Figure 9 that quartz and feldspar ages are indeed congruent at one sigma uncertainty for samples JB1-
651 OSL2- JB1-OSL5 (JB1-OSL1 yielded no accepted feldspar aliquots). This suggests that the quartz
652 measured here, which saturates at an unusually high level, still seems to yield accurate population D_es
653 even when up to a third of aliquots are saturated. For samples JB2-OSL5 and JB2-OSL9, though, where
654 no direct comparison can be made to feldspar D_es, quartz D_es must be considered a minimum value. It is
655 also possible that feldspar-derived D_es are underestimated where saturated aliquots make up a
656 significant proportion of those measured, i.e. for JB1-OSL7 and particularly JB1-OSL13. In both cases, we
657 suggest that $pIRIR_{290}$ ages should be considered, strictly speaking, as minimum ages.

658 **4.2.3.2 Dose rate estimation**

659 Dose rates may lead to inaccurate luminescence ages if the average dose rate during burial is
660 miscalculated, or D_e distributions caused by variable dose rates are misattributed to another cause (e.g.
661 partial bleaching). Given the nature of the sediments in Jubbah and the D_e measurements obtained, it
662 seems likely that beta microdosimetry may cause unusually high overdispersion in some samples. Beta
663 microdosimetry refers to variable beta doses to mineral grains within the same sample, and it arises
664 from the short (several mm) range of beta radiation. Minerals known to cause dose rate 'hotspots,'
665 such as K-rich feldspars and U-rich zircons have been reported as sparse but present in the Nefud by

Garzanti et al. (2013), with 0-2% K-feldspar by petrographic counting and 0.1%-0.5% heavy minerals by volume, of which zircons comprise approximately 1/3. Both minerals have also been identified by the authors in preliminary SEM analysis of Jubbah basin samples. Zircons in particular may have concentrations of tens to thousands of ppm U and Th (Hoskin and Schaltegger, 2003), and therefore have a significant effect on microdosimetric variation. 'Coldspots' can also occur, due to shielding effects from inert minerals, such as carbonates (Nathan et al., 2003). The combination of these microdosimetric effects will cause some amount of scatter in measured D_e, the exact amount of which is highly variable and depends upon factors including grain size, porosity, spatial distribution of radionuclides, and total dose rate (Cunningham et al., 2012; Guérin et al., 2015; Mayya et al., 2006; Nathan et al., 2003). These can result in inaccurate luminescence ages if misinterpreted as evidence for physical mixing or partial bleaching. In the Jubbah basin, large differences in overdispersion values have been noted (e.g. JB3 vs. JB1) depending on the age and composition of the sampled unit. Some of the samples with larger overdispersion values (e.g. JB3-OSL1) are likely to be affected by microdosimetry, while others, having both large overdispersion values and skewed populations (ARY-OSL5, JB3-OSL2) have been interpreted as partially bleached sediments. We believe in this case comparison of all Jubbah basin samples suggests that partial bleaching and the MAM is justified in these latter cases (see section 4.2.1 and 4.2.3.1). Larger-scale spatial heterogeneity, on the scale of centimeters to decimeters, has been accounted for by using a field gamma spectrometer to measure the gamma dose rate for all samples except ARY-OSL4.

Waterlain sediments, such as those sampled in the Jubbah Basin, are also known risks for significant temporal variability in dose rate, which may cause inaccurate luminescence ages (Krbetschek et al., 1994). This can occur via two routes: radioactive disequilibrium and post-depositional alteration of the sediment. The causes and consequences of each of these are discussed in detail below.

Disequilibrium is defined to be an imbalance in the secular equilibrium of a radioactive decay chain, i.e. that steady state in which the decay rates of all daughters and parents in a radioactive chain are equal. Disequilibrium arises due to the differential solubility of various chemical species of parents and daughters in the uranium and thorium decay series (Faure, 1986), as well as processes such as alpha particle recoil and gaseous diffusion (Olley et al, 1996). When a parent or daughter is lost or gained by any process other than radioactive decay (i.e. the system is 'open'), decay and production rates will no longer be balanced. Any unsupported excess will decrease via decay until secular equilibrium is regained, or conversely, a depleted daughter will increase. The time elapsed between initial disequilibrium and return to equilibrium will depend on the concentration introduced/removed, and the decay rates of the species involved.

For the calculation of luminescence ages, the problems caused by disequilibrium are twofold. First, dose rate conversion factors assume a concentration to energy conversion based on the presence of the entire decay chain for uranium and thorium, as well as an average 'natural' proportion between parent isotopes (e.g. ^{235}U and ^{238}U). When either parent or daughters are missing, this value becomes inaccurate. Second, disequilibrium produces a time dependent dose rate due to the ingrowth or unsupported decay of the daughter elements. The magnitude of the effect on the resulting luminescence ages depends on a number of factors: sample age, extent of disequilibrium in the decay chain, the proportion of the total dose contributed by the chain in disequilibrium, and the method of dose rate calculation. Common sources of disequilibrium relevant for luminescence include:

- $^{234}U/^{238}U$ disequilibrium: ^{234}U is a daughter of ^{238}U, which is more likely to escape from a sedimentary crystal lattice and form soluble uranyl complexes due to damage caused by alpha particles during ^{238}U decay (Faure, 1986). ^{234}U may be deficient in sediments that have been leached, and is usually in excess in water or waterlain sediments (Krbetschek et al., 1994).

- U/^{230}Th disequilibrium: This is produced by the solubility of uranium in oxidizing conditions due to production of compounds from the uranyl ion (UO2+2), and relative insolubility of thorium.
- Migration of radon.

In an environment where disequilibrium is possible, samples are more likely to yield incorrect ages if uranium levels are high and not related to the detrital mineral component.

Post-diagenetic alteration of sedimentary characteristics such as changing pore space availability or radioisotope concentrations may also cause inaccurate luminescence ages by altering the dose rate to mineral grains. Standard calculation methods assume that a dose rate calculated from modern sediment measurements provides a good estimate for the average dose rate to the grains during burial, or, in special cases, that corrections (such as attenuation by moisture in pore spaces) can be assessed and applied. Waterlain, carbonate-rich sediments such as occur commonly in the Jubbah Basin are particularly prone to temporal variation, via carbonate infilling of pore spaces and radioisotopic deposition or leaching from a sedimentary unit. Post-depositional carbonate precipitation in pore spaces and consequent decreases in sediment water content will result in modern dose rate calculations underestimating the average dose rate, as long as the carbonate infill is inert (Nathan and Mauz, 2008). Conversely, carbonate deposits are particularly prone to open system chemical behavior, as secondary carbonate infills in porous units may coprecipitate with uranyl compounds (Faure, 1986), leading to overestimates of dose rate, or soluble uranium may be leached, leading to dose rate underestimation. If significant post-depositional diagenetic alteration has occurred in the sediment, leading to uptake or leaching of radioisotopes, then modern measurements will not provide a good estimator of the average burial dose rate. This process may lead to disequilibrium, but it is more difficult to correct for, because there may be no constraints on the timing of the alteration. Radioisotopic activity ratios of Quaternary

735 lacustrine sediments cored from an endorheic basin in Syria suggest that uranium leaching and re-
736 precipitation in buried sediments is strongly linked to climatic conditions via humidity levels, and can
737 result in high concentrations of uranium in subsurface levels as uranium is preferentially leached from
738 near surface deposits and reprecipitated in deeper levels (Ghaleb et al., 1990; Li et al., 2008). Indeed, it
739 has been suggested that important sources of easily minable uranium may have been produced by the
740 Pleistocene fluvial systems of the Arabian Peninsula, which would have transported and concentrated
741 uranium deposits in near-surface uranium-rich calcretes (Dill, 2011).

742 The Jubbah basin may be significantly affected by high radioisotope levels in groundwater that
743 has chemically interacted with either the Saq aquifer or the Ha'il granites to the south. Shabana and
744 Kinsara (2014) have measured uranium and radium activities in groundwater of the Ha'il region which
745 are higher than the limits imposed by national regulations. These authors link high uranium levels to
746 leaching of granites and high radium concentrations to sandstone aquifers. The presence of 228-
747 Radium, which has a half-life of only 5.75 years, indicates a strong and ongoing chemical exchange
748 between Saq sandstone and regional groundwater. The immediate consequences of this for the Jubbah
749 Basin System may be twofold, including both disequilibrium and open system effects (diagenetic
750 alteration).

751 Open system behavior in carbonates is currently only directly detectable via disequilibrium
752 measurements (i.e. finding disequilibrium in sediments of a depositional age ca. 5x greater than the half-
753 life of the daughter in question) or petrographic studies, which can detect the precipitation of secondary
754 carbonates in pore spaces. Unfortunately, neither analysis could be applied to these samples. However,
755 we can examine closely the coherence of ages obtained on carbonate-rich levels as they compare
756 stratigraphically to bracketing sand-rich levels. And we may suggest that levels characterized by
757 particularly high uranium contents and which have been exposed to post-depositional water circulation
758 are more likely to have been 'overprinted' by secondary precipitation/absorption. The potential effects

759 of disequilibrium can also be gauged by calculating the Th/U ratio for samples; a typical crustal silicate
760 Th/U ratio is ca. 3.9 (O'Nions and McKenzie, 1993).

761 Significant variations in radioisotope concentrations are apparent in Table 5 and Figures 8 and 9,
762 and uranium concentrations and thorium/uranium ratios for all measured samples have been plotted
763 versus carbonate content in Figure S8. Elevated uranium levels (>15 ppm) occur in all sites but JB3, with
764 JB1 samples yielding the highest measured values at 2.5, 3.41, 4.16, and 6.35 m (JB1-OSL1, JB1-OSL3,
765 JB1-OSL4, and JB1-OSL7). Three of these samples (JB1-OSL1, JB1-OSL3, JB1-OSL4) also appear in the
766 lowest four Th/U ratios calculated, with samples JB2-OSL2, JB2-OSL5, and JB2-OSL3 filling out the top six
767 spots. It seems clear that carbonate-rich layers may be prone to uranium enrichment, though this is by
768 no means uniform. The upper three samples collected from JB3 had some of the greatest recorded
769 carbonate contents, but also yielded uranium contents <2.5 ppm. This is more in line with typical
770 uranium concentrations measured in the Nefud, which tend to be ≤3 ppm (Richard P Jennings et al.,
771 2016; Rosenberg et al., 2013; Stimpson et al., 2016).

772 We suggest that there is a link between high modern-day uranium contents, low Th/U ratios,
773 and luminescence age underestimation due to dose rate overestimation, leading to the age reversals
774 and disagreement independent chronological control. It is quite difficult to put constraints on the age
775 offsets caused by these processes. Given the overlying radiocarbon date as the minimum possible age
776 for sample JB1-OSL2, we can calculate that the central dose rate has been overestimated by ca. 30%.
777 Some of this overestimation may be due to an average water content value higher than the 5%
778 estimated here, but a significant increase in water content to 25-30% (water/wet sediment) would be
779 required to correct the inverted age-depth relationship. It seems more likely that a significant
780 proportion of this overestimation is due to calculating alpha and beta dose rates using standard
781 conversion factors, which assume secular equilibrium. For sample JB1-OSL2, 83% of the calculated
782 combined alpha and beta dose are due to the uranium concentration. The modern gamma dose rate

783 assessment should be less affected by current disequilibrium levels, as it has been measured via a field
784 gamma spectrometer (Guérin and Mercier, 2011), but some error will be introduced due to temporal
785 variance. If we assume that this age underestimation is entirely due to disequilibrium, given that this
786 sample is one of the youngest and has one of the highest dose contributions from uranium, it seems
787 plausible to suggest that a 30% dose rate overestimation is likely to be an upper limit for the age
788 underestimation we might expect via disequilibrium. If, however, elevated uranium levels (especially >
789 15 ppm) are due to post-diagenetic alteration, true ages become very difficult to constrain. We do not
790 believe that we have sufficient evidence for which samples may have been subject to this process, or
791 good constraints on the timing of the uranium deposition (e.g. early uptake or linear uptake) to
792 successfully propose ages based on model calculations such as those provided for open systems by
793 Zander et al. (2007) or with a model such as *Carb* developed by Mauz and Hoffmann (2014). In order to
794 provide some guidance, however, an attempt at subtraction dating (Feathers, 2002) will be discussed in
795 the next section for the samples from JB1 which have both quartz and feldspar measurements.

796 **4.3 Site Chronologies**

797 The issues raised above are discussed in detail for each of the four palaeoenvironmental
798 sections, and revised chronologies are presented.

799 **4.3.1 ARY**

800 Two quartz ages have been added to those previously published by Hilbert et al. (2014) (Figure
801 6, Table 6). Sample ARY-OSL4, collected from the upper marls, dates the formation of the fresh-water
802 body to 6.4 ± 0.4 ka. These deposits, therefore, formed soon after deposition of the top of Unit 8, which
803 was dated to 6.6 ± 0.7 ka (Hilbert et al., 2014). The age of the lower carbonate-rich level (units 4-6) has
804 already been closely bracketed to between 11.4 ± 0.8 ka and 12.2 ± 1.1 ka by dating of sand-rich units
805 above and below (Hilbert et al., 2014). Direct dating of sample ARY-OSL5 from this deposit, however,

has led to some unexpected results. In Section 4.2.1, it was noted that quartz from this sample yielded one of the highest overdispersion values measured in the Jubbah basin (57.32 ± 12.26 %), as well as a positively skewed D_e distribution. Such characteristics suggest that the sample may be partially bleached. If a typical Holocene Jubbah quartz overdispersion value (20%) is assumed in the minimum age model, the D_e of ARY-OSL5 becomes 17.94 ± 2.50 Gy and the final age 5.4 ± 0.8 ka. This is significantly younger than expected, as is the age calculated by using a less rigorous 31% overdispersion (see Figure S7), 9.2 ± 1.2 ka. The CAM age (11.2 ± 2.0 ka) is stratigraphically consistent.

There are two possibilities that may explain the offset between these MAM ages and the chronological constraints. The first is that the CAM D_e more accurately represents the appropriate D_e for input into the age equation. This would be the case if the skewed and overdispersed population were the result of microdosimetric variations in the sediment. Indeed, both skewness and overdispersion are known consequences of heterogeneous beta radiation (Nathan et al., 2003; Mayya et al., 2006). This and other studies (Petraglia et al., 2011; Hilbert et al., 2014) of analogous deposits in the Jubbah basin, however, indicate that the magnitude of the multigrain OSL overdispersion and skewness is highly unusual. Therefore, this does not seem to be the most likely cause. Second, we can observe that the uranium concentration in this unit is nearly four times that of the upper carbonate, thus it contributes ca. 86% of the beta dose rate to quartz grains as calculated in this study. We suggest that this sample does contain partially bleached quartz grains, making the minimum age model a more appropriate choice, and that the stratigraphic reversal in the ages is instead due to an overestimation of the dose rate.

4.3.2 JB1

Five quartz and seven feldspar ages are available for this stratigraphic section (Fig. 9a, Table 6). Feldspar and quartz ages increase with depth as expected for most of the measured samples, from a top

quartz age of 3.6 ± 0.3 ka (JB1-OSL1, 2.5 m) to a basal feldspar age of > 206.6 ± 49.7 ka (gravelly silt/sands, 9 m). This basal feldspar age, calculated via the central age model, must strictly be considered a minimum age due to the number of saturated aliquots measured. The D_e distribution yields a relatively high overdispersion value (ca. 48 %) and saturated aliquots. If we apply the minimum age model (overdispersion value = 40%) to this data, we calculate a D_e of 653.70 ± 151.67 Gy and an age of 151.9 ± 36.0 ka. We suspect, however, that this minimum age is underestimating the true age of the sediments, and suggest that the age of the deposits is more likely to be > 206.6 ± 49.7 ka.

Further up in the sequence, an age-depth reversal occurs between 5.5 and 9 m, with the feldspar age of sample JB1-OSL7 being significantly younger (76.3 ± 16.9 ka) than the age of the overlying sample JB1-OSL8 (135.8 ± 23.9 ka). The age reversal between these samples cannot be easily explained by the presence of partially bleached feldspars in the upper sample. While both samples have relatively high overdispersion values, applying the minimum age model with an overdispersion value of 40% (see discussion in section 4.2.3.1) yields D_es of 495.37 ± 97.57 Gy and 250.29 ± 40.08 Gy, for samples JB1-OSL7 and JB1-OSL8, respectively. These values yield ages of 54.1 ± 11.1 ka for the deeper sample and 112.4 ± 19.7 ka for the overlying sample, which does not resolve the age-depth discrepancy. If instead assuming that significant partial bleaching has occurred in the upper but not lower sample, a feldspar residual of several hundred gray would be required. This is far higher than any values calculated for the analogous site Al-Rabyah (Hilbert et al., 2014), and difficult to explain given the depositional regime. Instead, we propose that the older age found for the sand-rich sample JB1-OSL8 is more reliable than that calculated for the younger, carbonate-rich, and uranium enriched sample JB1-OSL7. The luminescence age calculated for JB1-OSL7 is likely to significantly underestimate the true burial age, and this is probably related to the OSL age underestimation higher in the sequence. As discussed above, comparison with independent chronological control in this section also suggests that some OSL quartz ages may be underestimating the true 'burial age'. The single radiocarbon date

obtained, 8980-8609 calBP (2.65-2.68 m), is significantly older than bracketing quartz OSL ages (3.6 ± 0.3 ka above and 6.4 ± 0.4 ka below). It seems probable that the carbonate-rich levels in this section are significantly affected by post-diagenetic uranium precipitation as well as disequilibrium.

In order to suggest an upper age limit for these carbonate-rich units, an equivalent dose subtraction method was used for samples JB1-OSL2, JB1-OSL3, JB1-OSL4, and JB1-OSL5. We are using a simple calculation which leverages the intrinsic difference in dose rates between quartz (no internal dose rate), and feldspar (constant internal dose rate) (see Feathers, 2002), though a number of other techniques have also been developed based on the same idea (Li et al., 2008; Vogel et al., 1999; Zhao and Li, 2002). Essentially, the quartz in each sample is used as a direct dosimeter ($D_{e,Q}$), which measures the total absorbed dose due to the external, environmental dose rate. This value can be subtracted from the feldspar, leaving only the effect of the internal dose rate. Age calculation then follows naturally:

$$\text{Age} = (D_{e,F} - D_{e,Q})/\dot{D}_{\text{F,int}}$$

This technique may be powerful when the modern dose rate is not expected to accurately reflect the average burial dose rate, i.e. in situations with extreme disequilibrium and/or secondary remobilization of radioisotopes in the sediment. In this region, however, the age results may be considered to be an upper age limit due to the potential for up to ca. 50 Gy residual doses caused by partial bleaching of the $pIRIR_{290}$ signal.

Central subtraction ages obtained for samples JB1-OSL2, JB1-OSL3, JB1-OSL4, and JB1-OSL5 are in stratigraphic order, and place these samples within MIS 5. The ages are unfortunately imprecise, however, with propagated errors of up to 70%, and a one sigma range extending from MIS 3 to 6. This is due primarily to a combination of the D_e overdispersion and the error limits on the internal dose rates calculated for the range of feldspar sizes used. Additionally, JB1-OSL2 clearly overestimates the

876 depositional age, based on comparison with the radiocarbon date. If we derive average external dose
877 rates to our measured quartz grains from the ages for samples JB1-OSL3 – OSL5, we have significant
878 error. Even given this, it is apparent that these new dose rates are far more in line with expected values
879 based on the measurement of similar sediments in the Nefud (Richard P Jennings et al., 2016; Rosenberg
880 et al., 2013; Stimpson et al., 2016). For samples JB1-OSL3 and JB1-OSL4, the central subtraction-
881 calculated dose rate is only ca. 20-27% of the dose rate values derived from modern measurements. A
882 much smaller change is calculated for sample JB1-OSL5.

883 For this site, therefore, the balance of evidence suggests the following chronology. Underlying
884 gravelly silt/sands (Unit 2) with a minimum age at least 151.9 ± 36.0 ka and probably 206.6 ± 49.7 ka,
885 were deposited initially. Units 7-8 probably represent the initial stages of MIS 5e, with the top of unit 9
886 dated to 135.8 ± 23.9. Unit 12 is most likely to have been deposited between 73.4 ± 6.8 ka (feldspar
887 age) and 117.1 ± 51.2 ka (subtraction age), therefore it attributable to MIS 5. Given the subtraction ages
888 obtained for samples JB1-OSL3 and JB1-OSL4, we suggest that potentially units 10-14 all date to MIS 5a-
889 c, though we cannot exclude the possibility of MIS 3 deposition as at the nearby site ALM 3 (Richard P
890 Jennings et al., 2016). Units 15 and above must be Holocene, based on the magnitude of the quartz D_es
891 measured, and units 17 and above were deposited after 8980-8609 calBP.

892 **4.3.3 JB2**

893 Six quartz ages and one feldspar age are available (Fig. 9b, Table 6). The two quartz ages
894 obtained for the upper 2 m, 8.6 ± 0.6 ka and 12.0 ± 1.1 ka, are in stratigraphic order, however, the next
895 four quartz ages (2 -6 m) do not yield a consistent age-depth relationship. Based on the equivalent
896 doses, it is apparent that the upper 4 m of the section represent Holocene accumulation, with a
897 significant increase in equivalent dose at approximately 4 m indicating a substantial gap in deposition.
898 Units below 4 m are likely Pleistocene in age. Finally, the lowermost sample, measured with feldspar,

yielded an age of 359.4 ± 84.3 ka. The D_e distribution for this sample is unusual, with one outlier aliquot (ca. 260 Gy) and a cluster of five aliquots at approximately 1000 Gy. Interpreting such data is problematic, as it is quite difficult to propose a mechanism by which the majority of the sediment would be partially bleached to such a degree. Physical sediment mixing via bioturbation or another process may be possible, particularly if younger sediments are building up over a much older basal sediment. In this case, we prefer the central age model results, but note this difficulty for future study.

Other anomalies in the age-depth relationship for this section indicate that multiple sample ages are problematic. Quartz D_e distributions, however, appear suitable. All of the presumably Holocene aliquot populations have low overdispersion values (maximum 21.21 ± 6.39% for sample JB2-OSL2) and acceptable values were calculated for the sampled Pleistocene units (maximum 35.73 ± 11.83%). Moreover, there is no correlation between the magnitude of the overdispersion and the age reversals, which would be expected if this were caused by partial bleaching. That is, if the reversal in the Holocene sediments is due to partial bleaching, the 'overestimated' upper ages should have higher overdispersions. In the Pleistocene sediments, there are a number of saturated aliquots (up to 5 of 18 for sample JB2-OSL5), which suggests that the calculated quartz OSL age might underestimate the true burial age. However, this does not explain the dramatic age reversal (more than 100,000 years) between samples JB2-OSL5 and JB2-OSL9.

Considering possible issues with dose rate determination, it has already been noted (section 4.2.3.2) that samples JB2-OSL2, JB2-OSL3, and JB2-OSL5 yield three of the six lowest Th/U ratios from dated samples in this study (Figure S8). Disequilibrium may therefore cause these ages to be underestimated. Interestingly, however, significant uranium enrichment is only noted at ca. 6.5 m depth, though the concentration is still less than half of that measured for shallow samples from JB1. It can also be noted that the equivalent doses measured for samples JB2-OSL5 and JB2-OSL9 are within 1

sigma uncertainty of each other, while their ages are 100,000 years offset. This also suggests potential difficulties with dose rate determination.

Given the lack of sand-rich units within this section that can be used as reliable age markers, it is very difficult to suggest a likely chronology. All waterlain sediments at the Central Quarry must have been deposited after the basal feldspar age of 359.4 ± 84.3 ka (clayey sands). A clear depositional hiatus is noted at around 4 m depth, between samples JB1-OSL4 and JB1-OSL5. Based on Th/U ratios and low U contents, we suggest that samples JB1-OSL1 and 4 are likely to be the most reliable Holocene samples. These ages are indistinguishable within 1 sigma error, suggesting the Holocene sediments were deposited around or slightly before 8.6 ka.

4.3.4 JB3

Three samples (JB3-OSL1—JB3-OSL3) have been dated with quartz OSL, while both quartz and feldspar ages have been obtained for underlying sample JB3-OSL4 (Fig. 8B, Table 6). Two anomalies are present in the calculated CAM ages: quartz ages for samples JB3-OSL3 and JB3-OSL4 are stratigraphically reversed, and there is a significant discrepancy between the quartz and feldspar ages for sample JB3-OSL4.

Some consideration has already been given to the potential for partial bleaching in this setting (Section 4.2.1). As noted previously, all three samples collected from JB3 carbonates have unusually high quartz D_e overdispersion values in the context of the Jubbah basin samples. Assuming that partial bleaching can be identified by a combination of positive skewness and high overdispersion, it was suggested that the luminescence age for sample JB3-OSL2 should be calculated from the MAM D_e. By analogy with the measurements from the underlying sand, and given the high overdispersions of quartz from the bracketing samples, we applied an overdispersion value of 30%. A MAM D_e of 55.00 ± 6.32 Gy was calculated, with approximately 80% of aliquots fully bleached.

945 Samples JB3-OSL1 and JB3-OSL3, with high overdispersion but symmetric distributions, are likely
946 to be better suited by CAM D_es, as microdosimetric variations in the sampled sediment seem to be a
947 plausible cause for such distributions. These calcretes are far more well-consolidated and have a lower
948 porosity than any others sampled in the Jubbah basin, which may indicate a differing geochemical and
949 dosimetric environment. It seems plausible that some grains from these samples will have been
950 completely overgrown by inert carbonates, perhaps unusually in the Jubbah basin, and therefore receive
951 a negligible beta dose rate (Nathan et al., 2003). Additionally, sample JB3-OSL1 was collected adjacent
952 to a well-developed shell bed and contained numerous shell fragments. Shell fragments may either
953 comprise inert carbonate, and lower dose rates to grains, or absorb uranium from the sediment and
954 increase dose rates (Kaufman et al., 1996). In combination with the known presence of heavy minerals,
955 such as zircons, significant microdosimetric variation seems likely, though a petrographic study would be
956 necessary to prove this. Depending on the size of the shell fragments, they may also cause systematic
957 errors in calculated beta dose rates (Cunningham, 2016). Again, extensive investigation of these
958 sediments would be necessary to further refine the calculated dose rates and test the effect of these
959 various confounding factors.
960 The single feldspar age obtained for this site yields an age of 105.3 ± 14.8 for unit 1, an
961 overestimate of ca. 30,000 years in comparison to the quartz age for the same sample. If this difference
962 is attributed to partial bleaching, we can calculate a residual dose of approximately 55 Gy. This is
963 certainly plausible, given the range calculated for samples from section ARY, therefore we prefer the
964 quartz OSL age for sample JB3-OSL4.
965 Age results based on a MAM D_e for JB3-OSL2 and CAM D_es for all other samples are shown in
966 Figure 8B. Given an examination of all the data, we understand that the age calculations for this site are
967 not entirely straightforward. Nevertheless, we believe that the overall weight of the evidence at the
968 moment suggests that relatively slow deposition of waterlain sediments seems to have occurred after

75.3 ± 8.1 ka, with the youngest sample dating to 56.2 ± 8.3 ka. Given the relative congruence between sample D_es, the low uranium contents, and the low porosity of the upper three samples, it seems unlikely that circulating groundwater has caused diagenetic alteration.

5. Conclusions

The Jubbah basin preserves complex, heterogeneous sedimentary records. Our work highlights that records from this basin can present some significant problems for luminescence dating, including:

- Significant temporal gaps (as at JB2) that are not visible in the field.
- Depositional ages for sediments potentially ranging from the Holocene through MIS 11 or even older.
- Mineral fractions containing significant proportions of gypsum, which may affect $pIRIR_{290}$ signals without careful application of rejection criteria (Clark-Balzan, 2016)
- Carbonate-rich subsurface sediments subject to reprecipitation of carbonate leading to significant post-depositional alteration of radioisotope concentration and disequilibrium (Ghaleb et al., 1990; Li et al., 2008).

It is likely that such difficulties are widespread in comparable settings, in which subsurface sediments have been exposed to multiple cycles of groundwater percolation. It should be noted that it is difficult *a priori* to suggest which units will have been significantly affected (e.g. significant uranium enrichment throughout JB1 and rare at JB2).

Climatically relevant chronological frameworks can still be developed, however, via the approach used in this paper, i.e. extensive sampling through the profile, luminescence dating of both quartz and feldspar, and careful consideration of correlations between elemental concentrations, sedimentary characteristics, D_es and dose rates. Even when ages cannot necessarily be estimated (e.g.

sample JB2-OSL5 in JB2), equivalent dose versus depth plots may provide important palaeoenvironmental evidence.

Studied sections preserve a remarkable record of recurrent humidity during the Holocene, MIS 3, MIS 5, and likely older basal sediments dating between MIS 7 and MIS 9 or MIS 11. Records of Holocene humidity from the interior of the Nefud are known only from Jubbah deposits, while MIS 3 deposits indicative of surface humidity have only been reported from the nearby site ALM-3 on the southern edge of the Nefud (Jennings et al., 2016). The particular environmental conditions supported by this humidity cannot be inferred without significant further analysis, which will be discussed in a subsequent publication. However, it seems likely that the groundwater in the Jubbah basin would have constituted a valuable resource, and the recurrent nature of this groundwater indicated by the dates in this study may have led to the concurrent presence of archaeological sites of various periods in this generally arid area.

Acknowledgements

We thank His Royal Highness Prince Sultan bin Salman, President of the Saudi Commission for Tourism and National Heritage (SCTH), and Prof. Ali Ghabban, Vice President for Antiquities and Museums, for permission to carry out this research. We also thank our Saudi colleagues from the SCTH, especially Jamal Omar, Sultan Al-Fagir, and Abdulaziz al-Omari for their support and assistance with the field investigations. Dr. Abdullah Alsharekh, King Saud University, has also been a key supporter of our research in Saudi Arabia. Financial support for the fieldwork and project was provided by the European Research Council (ERC) (grant number 295719, to MDP) and the SCTH. The senior author was supported by the ERC and a Marie Skłodowska-Curie Individual Fellowships (project 658005) during part of the manuscript preparation. Thanks also go to Mr. Christopher Doherty of the Research Laboratory for Archaeology and the History of Art (University of Oxford), for discussions concerning the deposition

and post-depositional alteration of carbonate-rich sediments, and to two anonymous reviewers for their helpful comments.

References

Aitken, M.J., 1998. An Introduction to Optical Dating: The dating of Quaternary Sediments by the Use of Photon-stimulated Luminescence. Oxford University Press, Oxford.

Aitken M.J., Xie, J., 1990. Moisture correction for annual gamma dose. Anc. TL 8, 6–9.

Armitage, S.J., Jasim, S. a, Marks, A.E., Parker, A.G., Usik, V.I., Uerpmann, H.-P., 2011. The southern route "out of Africa": evidence for an early expansion of modern humans into Arabia. Science 331, 453–456. doi:10.1126/science.1199113

Atkinson, O.A.C., Thomas, D.S.G., Goudie, A.S., Bailey, R.M., 2011. Late Quaternary chronology of major dune ridge development in the northeast Rub' al-Khali, United Arab Emirates. Quat. Res. 76, 93–105. doi:10.1016/j.yqres.2011.04.003

Auclair, M., Lamothe, M., Huot, S., 2003. Measurement of anomalous fading for feldspar IRSL using SAR. Radiat. Meas. 37, 487–492. doi:10.1016/S1350-4487(03)00018-0

Balescu, S., Lamothe, M., 1994. Comparison of TL and IRSL age estimates of feldspar coarse grains from waterlain sediments. Quat. Geochronol. 13, 437–444.

Berger, G.W., 1990. Effectiveness of natural zeroing of the thermoluminescence in sediments. J. Geophys. Res. 95, 12375–12397. doi:10.1029/JB095iB08p12375

Blechschmidt, I., Matter, A., Preusser, F., Rieke-Zapp, D., 2009. Monsoon triggered formation of Quaternary alluvial megafans in the interior of Oman. Geomorphology 110, 128–139. doi:10.1016/j.geomorph.2009.04.002

Bøtter-Jensen, L., Andersen, C.E., Duller, G. a T., Murray, a. S., 2003. Developments in radiation, stimulation and observation facilities in luminescence measurements. Radiat. Meas. 37, 535–541. doi:10.1016/S1350-4487(03)00020-9

Bøtter-Jensen, L., Bulur, E., Duller, G. a T., Murray, a. S., 2000. Advances in luminescence instrument systems. Radiat. Meas. 32, 523–528. doi:10.1016/S1350-4487(00)00039-1

Breeze, P.S., Groucutt, H.S., Drake, N.A., White, T.S., Jennings, R.P., Petraglia, M.D., 2016. Palaeohydrological corridors for hominin dispersals in the Middle East ~250–70,000 years ago. Quat. Sci. Rev. 144, 155–185. doi:10.1016/j.quascirev.2016.05.012

Brennan, B.J., 2003. Beta doses to spherical grains. Radiat. Meas. 37, 299–303. doi:10.1016/S1350-4487(03)00011-8

1045 Brennan, B.J., Lyons, R.G., Phillips, S.W., 1991. Attenuation of alpha particle track dose for spherical
1046 grains. Int. J. Radiat. Appl. Instrumentation. Part D. Nucl. Tracks Radiat. Meas. 18, 249–253.
1047 doi:10.1016/1359-0189(91)90119-3

1048 Bronk Ramsey, C., Higham, T.F.G., Owen, D.C., Pike, A.W.G., Hedges, R.E.M., 2002. Radiocarbon dates
1049 from the Oxford AMS system: Archaeometry Datelist 31. Archaeometry 44, 1–149.

1050 Bronk Ramsey, C., Staff, R.A., Bryant, C.L., Brock, F., Kitagawa, H., van der Plicht, J., Schlolaut, G.,
1051 Marshall, M.H., Brauer, A., Lamb, H.F., Payne, R.L., Tarasov, P.E., Haraguchi, T., Gotanda, K.,
1052 Yonenobu, H., Yokoyama, Y., Tada, R., Nakagawa, T., 2012. A complete terrestrial radiocarbon
1053 record for 11.2 to 52.8 kyr B.P. Science (80-.). 338, 370–374.

1054 Buylaert, J.P., Jain, M., Murray, A.S., Thomsen, K.J., Thiel, C., Sohbati, R., 2012. A robust feldspar
1055 luminescence dating method for Middle and Late Pleistocene sediments. Boreas 41, 435–451.
1056 doi:10.1111/j.1502-3885.2012.00248.x

1057 Buylaert, J.P., Murray, a. S., Gebhardt, a. C., Sohbati, R., Ohlendorf, C., Thiel, C., Wastegård, S.,
1058 Zolitschka, B., 2013. Luminescence dating of the PASADO core 5022-1D from Laguna Potrok Aike
1059 (Argentina) using IRSL signals from feldspar. Quat. Sci. Rev. 71, 70–80.
1060 doi:10.1016/j.quascirev.2013.03.018

1061 Buylaert, J.-P., Thiel, C., Murray, A.S., Vandenberghe, D. a. G., Yi, S., Lu, H., 2011. IRSL and post-IR IRSL
1062 residual doses recorded in modern dust samples from the Chinese Loess Plateau. Geochronometria
1063 38, 432–440. doi:10.2478/s13386-011-0047-0

1064 Caley, T., Malaizé, B., Zaragosi, S., Rossignol, L., Bourget, J., Eynaud, F., Martinez, P., Giraudeau, J.,
1065 Charlier, K., Ellouz-Zimmermann, N., 2011. New Arabian Sea records help decipher orbital timing of
1066 Indo-Asian monsoon. Earth Planet. Sci. Lett. 308, 433–444. doi:10.1016/j.epsl.2011.06.019

1067 Clark-Balzan, L., 2016. Source and characteristics of blue , infrared (IR), and post-IR IR stimulated signals
1068 from gypsum-rich samples. Anc. TL 34, 6–13.

1069 Crassard, R., Petraglia, M.D., Parker, A.G., Parton, A., Roberts, R.G., Jacobs, Z., Alsharekh, A., Al-Omari,
1070 A., Breeze, P., Drake, N. a., Groucutt, H.S., Jennings, R., Régagnon, E., Shipton, C., 2013. Beyond the
1071 Levant: First Evidence of a Pre-Pottery Neolithic Incursion into the Nefud Desert, Saudi Arabia.
1072 PLoS One 8. doi:10.1371/journal.pone.0068061

1073 Cunningham, A.C., 2016. External beta dose rates to mineral grains in shell-rich sediment. Anc. TL 34, 1–
1074 5.

1075 Cunningham, A.C., Devries, D.J., Schaart, D.R., 2012. Experimental and computational simulation of beta-
1076 dose heterogeneity in sediment. Radiat. Meas. 47, 1060–1067. doi:10.1016/j.radmeas.2012.08.009

1077 Dean, W.E., 1974. Determination of carbonate and organic matter in calcareous sediments and
1078 sedimentary rocks by loss on ignition; comparison with other methods. J. Sediment. Res. 44, 242–
1079 248.

Debaene, G., 2003. Uranium-series dating of marly sediments: application to Jaroszów fossil lake. Geochronometria 22, 15–26.

Des Combes, H.J., Pierre Caulet, J., Tribovillard, N., 2005. Monitoring the variations of the Socotra upwelling system during the last 250 kyr: A biogenic and geochemical approach. Palaeogeogr. Palaeoclimatol. Palaeoecol. 223, 243–259. doi:10.1016/j.palaeo.2005.04.007

Dietze, M., Kreutzer, S., Burow, C., Fuchs, M.C., Fischer, M., Schmidt, C., 2016. The abanico plot : Visualising chronometric data with individual standard errors. Quat. Geochronol. 31, 12–18. doi:10.1016/j.quageo.2015.09.003

Dill, H.G., 2011. A comparative study of uranium – thorium accumulation at the western edge of the Arabian Peninsula and mineral deposits worldwide. Arab. J. Geosci. 4, 123–146. doi:10.1007/s12517-009-0107-4

Duller, G. a T., 2012. Improving the accuracy and precision of equivalent doses determined using the optically stimulated luminescence signal from single grains of quartz. Radiat. Meas. 47, 770–777. doi:10.1016/j.radmeas.2012.01.006

Duller, G.A.T., 2003. Distinguishing quartz and feldspar in single grain luminescence measurements. Radiat. Meas. 37, 161–165. doi:10.1016/S1350-4487(02)00170-1

Durcan, J. a., King, G.E., Duller, G. a. T., 2015. DRAC: Dose Rate and Age Calculator for trapped charge dating. Quat. Geochronol. 28, 54–61. doi:10.1016/j.quageo.2015.03.012

Durcan, J.A., King, G.E., 2017. DRAC: Dose Rate and Age Calculator.

Duval, M., Arnold, L.J., 2013. Field gamma dose-rate assessment in natural sedimentary contexts using LaBr3(Ce) and NaI(Tl) probes: A comparison between the “threshold” and “windows” techniques. Appl. Radiat. Isot. 74, 36–45. doi:10.1016/j.apradiso.2012.12.006

Edgell, H.S., 2006. Arabian Deserts: Nature, Origin, Evolution. Springer-Verlag, Heidelberg, Germany.

Farrant, A.R., Duller, G. a T., Parker, A.G., Roberts, H.M., Parton, A., Knox, R.W.O., Bide, T., 2015. Developing a framework of Quaternary dune accumulation in the northern Rub’ al-Khali, Arabia. Quat. Int. 382, 132–144. doi:10.1016/j.quaint.2015.02.022

Feathers, J.K., 2002. Luminescence Dating in Less Than Ideal Conditions: Case Studies from Klasies River Main Site and Duinefontein, South Africa. J. Archaeol. Sci. 29, 177–194. doi:10.1006/jasc.2001.0685

Fleitmann, D., Burns, S.J., Mudelsee, M., Neff, U., Kramers, J., Mangini, A., Matter, A., 2003. Holocene forcing of the Indian monsoon recorded in a stalagmite from southern Oman. Science 300, 1737–1739. doi:10.1126/science.1083130

1112 Fleitmann, D., Burns, S.J., Pekala, M., Mangini, A., Al-Subbary, A., Al-Aowah, M., Kramers, J., Matter, A.,
1113 2011. Holocene and Pleistocene pluvial periods in Yemen, southern Arabia. Quat. Sci. Rev. 30, 783–
1114 787. doi:10.1016/j.quascirev.2011.01.004

1115 Galbraith, R.F., Roberts, R.G., Laslett, G.M., Yoshida, H., Olley, J.M., 1999. Optical dating of single and
1116 multiple grains of quartz from jinmium rock shelter, northern Australia: Part I, Experimental design
1117 and statistical models. Archaeometry 41, 339–364.

1118 Garrard, A.N., Harvey, C.P.D., Switsur, V.R., 1981. Environment and settlement during the Upper
1119 Pleistocene and Holocene at Jubba in the Great Nefud, northern Arabia. Atlal 5, 137–148.

1120 Garzanti, E., Andò, S., Vezzoli, G., Lustrino, M., Boni, M., Vermeesch, P., 2012. Petrology of the Namib
1121 Sand Sea: Long-distance transport and compositional variability in the wind-displaced Orange
1122 Delta. Earth-Science Rev. 112, 173–189. doi:10.1016/j.earscirev.2012.02.008

1123 Garzanti, E., Vermeesch, P., Andò, S., Vezzoli, G., Valagussa, M., Allen, K., Kadi, K. a., Al-Juboury, A.I. a,
1124 2013. Provenance and recycling of Arabian desert sand. Earth-Science Rev. 120, 1–19.
1125 doi:10.1016/j.earscirev.2013.01.005

1126 Ghaleb, B., Hillaire-Marcel, C., Causse, C., Gariepy, C., Vallieres, S., 1990. Fractionation and recycling of U
1127 and Th isotopes in a semi-arid endoreic depression of central Syria. Geochim. Cosmochim. Acta 54,
1128 1025–1035. doi:10.1016/0016-7037(90)90436-O

1129 Ginau, a., Engel, M., Brückner, H., 2012. Holocene chemical precipitates in the continental sabkha of
1130 Tayma (NW Saudi Arabia). J. Arid Environ. 84, 26–37. doi:10.1016/j.jaridenv.2012.03.020

1131 Gliganic, L. a., May, J.H., Cohen, T.J., 2015. All mixed up: Using single-grain equivalent dose distributions
1132 to identify phases of pedogenic mixing on a dryland alluvial fan. Quat. Int. 362, 23–33.
1133 doi:10.1016/j.quaint.2014.07.040

1134 Godfrey-Smith, D.I., Huntley, D.J., Chen, W.H., 1988. Optical dating studies of quartz and feldspar
1135 sediment extracts. Quat. Sci. Rev. 7, 373–380.

1136 Grimm, E.C., 2011. High-resolution age model based on AMS radiocarbon ages for Kettle Lake, North
1137 Dakota, USA. Radiocarbon 53, 39–53.

1138 Groucutt, H.S., Petraglia, M.D., 2012. The prehistory of the Arabian peninsula: Deserts, dispersals, and
1139 demography. Evol. Anthropol. Issues, News, Rev. 21, 113–125. doi:10.1002/evan.21308

1140 Groucutt, H.S., Shipton, C., Alsharekh, A., Jennings, R., Scerri, E.M.L., Petraglia, M.D., 2015a. Late
1141 Pleistocene lakeshore settlement in northern Arabia: Middle Palaeolithic technology from Jebel
1142 Katefeh, Jubbah. Quat. Int. 382, 215–236. doi:10.1016/j.quaint.2014.12.001

1143 Groucutt, H.S., White, T.S., Clark-Balzan, L., Parton, A., Crassard, R., Shipton, C., Jennings, R.P., Parker,
1144 A.G., Breeze, P.S., Scerri, E.M.L., Alsharekh, A., Petraglia, M.D., 2015b. Human occupation of the
1145 Arabian Empty Quarter during MIS 5: Evidence from Mundafan Al-Buhayrah, Saudi Arabia. Quat.
1146 Sci. Rev. 119, 116–135. doi:10.1016/j.quascirev.2015.04.020

Guagnin, M., Shipton, C., Martin, L., Petraglia, M., 2017. The Neolithic site of Jebel Oraf 2, northern Saudi Arabia: First report of a directly dated site with faunal remains. Archaeol. Res. Asia 9, 63–67. doi:10.1016/j.ara.2017.02.001

Guérin, G., Jain, M., Thomsen, K.J., Murray, A.S., Mercier, N., 2015. Modelling dose rate to single grains of quartz in well-sorted sand samples: The dispersion arising from the presence of potassium feldspars and implications for single grain OSL dating. Quat. Geochronol. 27, 52–65. doi:10.1016/j.quageo.2014.12.006

Guérin, G., Mercier, N., 2011. Determining gamma dose rates by field gamma spectroscopy in sedimentary media: Results of Monte Carlo simulations. Radiat. Meas. 46, 190–195. doi:10.1016/j.radmeas.2010.10.003

Guerin, G., Mercier, N., Adamiec, G., 2011. Dose-rate conversion factors: Update. Anc. TL 29, 5–8.

Guérin, G., Mercier, N., Nathan, R., Adamiec, G., Lefrais, Y., 2012. On the use of the infinite matrix assumption and associated concepts: A critical review. Radiat. Meas. 47, 778–785. doi:10.1016/j.radmeas.2012.04.004

Hanson, P.R., Mason, J. a., Jacobs, P.M., Young, a. R., 2015. Evidence for bioturbation of luminescence signals in eolian sand on upland ridgetops, southeastern Minnesota, USA. Quat. Int. 362, 108–115. doi:10.1016/j.quaint.2014.06.039

Heiri, O., Lotter, A.F., Lemcke, G., 2001. Loss on ignition as a method for estimating organic and carbonate content in sediments: reproducibility and comparability of results. J. Paleolimnol. 25, 101–110. doi:10.1023/A:1008119611481

Hilbert, Y.H., White, T.S., Parton, A., Clark-Balzan, L., Crassard, R., Groucutt, H.S., Jennings, R.P., Breeze, P., Parker, A., Shipton, C., Al-Omari, A., Alsharekh, A.M., Petraglia, M.D., 2014. Epipalaeolithic occupation and palaeoenvironments of the southern Nefud desert, Saudi Arabia, during the Terminal Pleistocene and Early Holocene. J. Archaeol. Sci. 50, 460–474. doi:10.1016/j.jas.2014.07.023

Hoelzmann, P., Jolly, D., Harrison, S.P., Laarif, F., Bonnefille, R., 1998. and the Arabian peninsula : A data set for the analysis of biogeophysical feedbacks in the climate system 12, 35–51.

Hoskin, P.W.O., Schaltegger, U., 2003. The Composition of Zircon and Igneous and Metamorphic Petrogenesis. Rev. Mineral. Geochemistry 53, 27–62. doi:10.2113/0530027

Huntley, D.J., Baril, M.R., 1997. The K content of the K-feldspars being measured in optical dating or in thermoluminescence dating. Anc. TL 15, 11–13.

Huntley, D.J., Godfrey-Smith, D.I., Thewalt, M.L.W., 1985. Optical dating of sediments. Nature 313, 105–107. doi:10.1038/313105a0

Huntley, D.J., Hancock, R.G. V, 2001. The Rb contents of the K-feldspar grains being measured in optical dating. Anc. TL.

1182 Huntley, D.J., Lamothe, M., 2001. Ubiquity of anomalous fading in K-feldspars and the measurement and
1183 correction for it in optical dating. Can. J. Earth Sci. 38, 1093–1106. doi:10.1139/e01-013

1184 Hussein, M.T., Bazuhair, A.G., Ageeb, A.E., 1992. Hydrogeology of the Saq Formation east of Hail,
1185 northern Saudi Arabia. Q. J. Eng. Geol. Hydrogeol. 25, 57–64.
1186 doi:10.1144/GSL.QJEG.1992.025.01.05

1187 Jain, M., Ankjærgaard, C., 2011. Towards a non-fading signal in feldspar: Insight into charge transport
1188 and tunnelling from time-resolved optically stimulated luminescence. Radiat. Meas. 46, 292–309.
1189 doi:10.1016/j.radmeas.2010.12.004

1190 Jain, M., Buylaert, J.P., Thomsen, K.J., Murray, a. S., 2014. Further investigations on “non-fading” in K-
1191 Feldspar. Quat. Int. 362, 3–7. doi:10.1016/j.quaint.2014.11.018

1192 Jennings, R.P., Parton, a S.H., Clark-balzan, L., White, T.O.M.S., Groucutt, H.U.W.S., Breeze, P.S., Parker,
1193 A.G., Drake, N. a, Petraglia, M.D., 2016. Human occupation of the northern Arabian interior during
1194 early Marine Isotope Stage 3 31, 953–966. doi:10.1002/jqs.2920

1195 Jennings, R.P., Parton, A., Clark-Balzan, L., White, T.S., Groucutt, H.S., Breeze, P.S., Parker, A.G., Drake,
1196 N.A., Petraglia, M.D., 2016. Human occupation of the northern Arabian interior during early Marine
1197 Isotope Stage 3. J. Quat. Sci. 31, 953–966. doi:10.1002/jqs.2920

1198 Kars, R.H., Busschers, F.S., Wallinga, J., 2012. Validating post IR-IRSL dating on K-feldspars through
1199 comparison with quartz OSL ages. Quat. Geochronol. 12, 74–86. doi:10.1016/j.quageo.2012.05.001

1200 Kaufman, A., Ghaleb, B., Wehmiller, J.F., Hillaire-Marcel, C., 1996. Uranium concentration and isotope
1201 ratio profiles within Mercenaria shells: Geochronological implications. Geochim. Cosmochim. Acta
1202 60, 3735–3746. doi:10.1016/0016-7037(96)00190-1

1203 Kellogg, K.S., Stoeser, D.B., 1985. Reconnaissance geology of the Ha ’ il Quadrangle , sheet 27 / 41B ,
1204 Kingdom of Saudi Arabia.

1205 Krbetschek, M.R., Rieser, U., Zöller, L., Heinicke, J., 1994. Radioactive disequilibria in palaeodosimetric
1206 dating of sediments. Radiat. Meas. 23, 485–489.

1207 Li, B., Jacobs, Z., Roberts, R., Li, S.-H., 2014. Review and assessment of the potential of post-IR IRSL
1208 dating methods to circumvent the problem of anomalous fading in feldspar luminescence.
1209 Geochronometria 41, 178–201. doi:10.2478/s13386-013-0160-3

1210 Li, B., Li, S.-H., Wintle, A.G., 2008. Overcoming Environmental Dose Rate Changes in Luminescence
1211 Dating of Waterlain Deposits. Geochronometria 30, 33–40. doi:10.2478/v10003-008-0003-z

1212 Lowick, S.E., Trauerstein, M., Preusser, F., 2012. Testing the application of post IR-IRSL dating to fine
1213 grain waterlain sediments. Quat. Geochronol. 8, 33–40. doi:10.1016/j.quageo.2011.12.003

1214 Marty, J., Myrbo, A., 2014. Radiocarbon dating suitability of aquatic plant macrofossils 435–443.
1215 doi:10.1007/s10933-014-9796-0

Mauz, B., Hoffmann, D., 2014. What to do when carbonate replaced water : Carb , the model for estimating the dose rate of carbonate-rich samples 32, 24–32.

Mayya, Y.S., Morthekai, P., Murari, M.K., Singhvi, a. K., 2006. Towards quantifying beta microdosimetric effects in single-grain quartz dose distribution. Radiat. Meas. 41, 1032–1039. doi:10.1016/j.radmeas.2006.08.004

Mercier, N., Falguères, C., 2007. Field gamma dose-rate measurement with a NaI(Tl) detector: re-evaluation of the “threshold” technique. Anc. TL 25, 1–4.

Murray, a. S., Thomsen, K.J., Masuda, N., Buylaert, J.P., Jain, M., 2012. Identifying well-bleached quartz using the different bleaching rates of quartz and feldspar luminescence signals. Radiat. Meas. 47, 688–695. doi:10.1016/j.radmeas.2012.05.006

Murray, A.S., Wintle, A.G., 2003. The single aliquot regenerative dose protocol: Potential for improvements in reliability. Radiat. Meas. 37, 377–381. doi:10.1016/S1350-4487(03)00053-2

Murray, A.S., Wintle, A.G., 2000. Luminescence dating of quartz using an improved single-aliquot regenerative-dose protocol. Radiat. Meas. 32, 57–73. doi:10.1016/S1350-4487(99)00253-X

Nathan, R.P., Mauz, B., 2008. On the dose-rate estimate of carbonate-rich sediments for trapped charge dating. Radiat. Meas. 43, 14–25. doi:10.1016/j.radmeas.2007.12.012

Nathan, R.P., Thomas, P.J., Jain, M., Murray, a. S., Rhodes, E.J., 2003. Environmental dose rate heterogeneity of beta radiation and its implications for luminescence dating: Monte Carlo modelling and experimental validation. Radiat. Meas. 37, 305–313. doi:10.1016/S1350-4487(03)00008-8

O’Nions, R.K., McKenzie, D., 1993. Estimates of Mantle Thorium/ Uranium Ratios from Th, U and Pb Isotope Abundances in Basaltic Melts. Philos. Trans. Phys. Sci. Eng. 342, 65–77.

Olley, J.M., Caitcheon, G., Murray, A., 1998. The distribution of apparent dose as determined by optically stimulated luminescence in small aliquots of fluvial quartz: Implications for dating young sediments. Quat. Geochronol. 17, 1033–1040.

Olley, J.M., Pietsch, T., Roberts, R.G., 2004. Optical dating of Holocene sediments from a variety of geomorphic settings using single grains of quartz. Geomorphology 60, 337–358. doi:10.1016/j.geomorph.2003.09.020

Oswald, W.W., Anderson, P.M., Brown, A., Brubaker, L.B., Hu, S., Lozhkin, A. V, Tinner, W., Kaltenrieder, P., 2005. Effects of sample mass and macrofossil type on radiocarbon dating of arctic and boreal lake sediments. The Holocene 15, 758–767.

Parton, A., Farrant, A.R., Leng, M.J., Schwenninger, J.-L., Rose, J.I., Uerpmann, H.-P., Parker, A.G., 2013. An early MIS 3 pluvial phase in Southeast Arabia: Climatic and archaeological implications. Quat. Int. 300, 62–74. doi:10.1016/j.quaint.2013.02.016

1250 Parton, A., Farrant, A.R., Leng, M.J., Telfer, M.W., Groucutt, H.S., Petraglia, M.D., Parker, A.G., 2015a.
1251 Alluvial fan records from southeast Arabia reveal multiple windows for human dispersal. Geology
1252 43, 295–298. doi:10.1130/G36401.1

1253 Parton, A., White, T.S., Parker, A.G., Breeze, P.S., Jennings, R., Groucutt, H.S., Petraglia, M.D., 2015b.
1254 Orbital-scale climate variability in Arabia as a potential motor for human dispersals. Quat. Int. 382,
1255 82–97. doi:10.1016/j.quaint.2015.01.005

1256 Petraglia, M.D., Alsharekh, A., Breeze, P., Clarkson, C., Crassard, R., Drake, N.A., Groucutt, H.S., Jennings,
1257 R., Parker, A.G., Parton, A., Roberts, R.G., Shipton, C., Matheson, C., Al-Omari, A., Veall, M.-A.,
1258 2012. Hominin dispersal into the Nefud Desert and Middle Palaeolithic Settlement along the
1259 Jubbah Palaeolake, Northern Arabia. PLoS One 7, e49840.

1260 Petraglia, M.D., Alsharekh, A., Crassard, R., Drake, N., Groucutt, H., Parker, A., Roberts, R., 2011a. Middle
1261 Paleolithic occupation on a Marine Isotope Stage 5 lakeshore in the Nefud Desert, Saudi Arabia.
1262 Quat. Sci. Rev. 30, 1555–1559.

1263 Petraglia, M.D., Alsharekh, A.M., Crassard, R., Drake, N. a., Groucutt, H., Parker, A.G., Roberts, R.G.,
1264 2011b. Middle Paleolithic occupation on a Marine Isotope Stage 5 lakeshore in the Nefud Desert,
1265 Saudi Arabia. Quat. Sci. Rev. 30, 1555–1559. doi:10.1016/j.quascirev.2011.04.006

1266 Petraglia, M.D., Groucutt, H., Parton, A., Alsharekh, A., 2015. Green Arabia: Human prehistory at the
1267 crossroads of contintents [Special Issue]. Quat. Int. 382, 1–302.

1268 Pigati, J.S., Quade, J., Wilson, J., Jull, a. J.T., Lifton, N. a., 2007. Development of low-background vacuum
1269 extraction and graphitization systems for 14C dating of old (40-60 ka) samples. Quat. Int. 166, 4–
1270 14. doi:10.1016/j.quaint.2006.12.006

1271 Preusser, F., Muru, M., Rosentau, A., 2014. Comparing different post-IR IRSL approaches for the dating
1272 of Holocene coastal foredunes from Ruhnu Island, Estonia. Geochronometria 41, 342–351.
1273 doi:10.2478/s13386-013-0169-7

1274 Ramsey, C., 2009. Bayesian analysis of radiocarbon dates. Radiocarbon 51, 337–360.

1275 Ramsey, C.B., Higham, T., Leach, P., 2004. Towards high-precision AMS: Progress and limitations.
1276 Radiocarbon 46, 17–24.

1277 Reimann, T., Tsukamoto, S., Naumann, M., Frechen, M., 2011. The potential of using K-rich feldspars for
1278 optical dating of young coastal sediments - A test case from Darss-Zingst peninsula (southern Baltic
1279 Sea coast). Quat. Geochronol. 6, 207–222. doi:10.1016/j.quageo.2010.10.001

1280 Reimer, P.J., Bard, E., Bayliss, A., Beck, J.W., Blackwell, P.G., Ramsey, C.B., Buck, C.E., Cheng, H., Edwards,
1281 R.L., Friedrich, M., Grootes, P.M., Fuilderson, T.P., Haflidason, H., Hajdas, I., Hatté, C., Heaton, T.J.,
1282 Hoffmann, D.L., Hogg, A.G., Hughen, K.A., Kaiser, K.F., Kromer, B., Manning, S.W., Niu, M., Reimer,
1283 R., Richards, D.A., Scott, E.M., Southon, J.R., Staff, R.A., Turney, C.S.M., van der Plicht, J., 2013.
1284 IntCal13 and Marine13 Radiocarbon Age Calibration Curves 0–50,000 Years cal BP. Radiocarbon 55,
1285 1869–1887. doi:10.2458/azu_js_rc.55.16947

Rhodes, E.J., Schwenninger, J.L., 2007. Dose rates and radioisotope concentrations in the concrete calibration blocks at Oxford. Anc. TL 25, 5–8.

Richter, D., Richter, A., Dornich, K., 2013. Lexsyg — A new system for luminescence research. Geochronometria 40, 220–228. doi:10.2478/s13386-013-0110-0

Rittenour, T.M., 2008. Luminescence dating of fluvial deposits: applications to geomorphic, palaeoseismic and archaeological research. Boreas 37, 613–635. doi:10.1111/j.1502-3885.2008.00056.x

Rosenberg, T.M., Preusser, F., Fleitmann, D., Schwalb, a., Penkman, K., Schmid, T.W., Al-Shanti, M. a., Kadi, K., Matter, a., 2011a. Humid periods in southern Arabia: Windows of opportunity for modern human dispersal. Geology 39, 1115–1118. doi:10.1130/G32281.1

Rosenberg, T.M., Preusser, F., Risberg, J., Plikk, A., Kadi, K. a., Matter, A., Fleitmann, D., 2013. Middle and Late Pleistocene humid periods recorded in palaeolake deposits of the Nafud desert, Saudi Arabia. Quat. Sci. Rev. 70, 109–123. doi:10.1016/j.quascirev.2013.03.017

Rosenberg, T.M., Preusser, F., Wintle, a. G., 2011b. A comparison of single and multiple aliquot TT-OSL data sets for sand-sized quartz from the Arabian Peninsula. Radiat. Meas. 46, 573–579. doi:10.1016/j.radmeas.2011.03.020

Roskosch, J., Tsukamoto, S., Meinsen, J., Frechen, M., Winsemann, J., 2012. Luminescence dating of an Upper Pleistocene alluvial fan and aeolian sandsheet complex: The Senne in the M??nsterland Embayment, NW Germany. Quat. Geochronol. 10, 94–101. doi:10.1016/j.quageo.2012.02.012

Schramm, A., Stein, M., Goldstein, S.L., 2000. Calibration of the 14C time scale to >40 ka by 234U–230Th dating of Lake Lisan sediments (last glacial Dead Sea). Earth Planet. Sci. Lett. 175, 27–40. doi:10.1016/S0012-821X(99)00279-4

Shabana, E.I., Kinsara, A.A., 2014. Radioactivity in the groundwater of a high background radiation area. J. Environ. Radioact. 137, 181–189. doi:10.1016/j.jenvrad.2014.07.013

Shipton, C., Parton, A., Breeze, P., Jennings, R., Groucutt, H.S., White, T.S., Drake, N., Crassard, R., Alsharekh, A., Petraglia, M.D., 2014. Large Flake Acheulean in the Nefud Desert of Northern Arabia. PaleoAnthropology 446–462. doi:10.4207/PA.2014.ART85

Spooner, N.A., 1994. On the optical dating signal from quartz. Radiat. Meas. 23, 593–600. doi:10.1016/1350-4487(94)90105-8

Stimpson, C.M., Lister, A., Parton, A., Clark-Balzan, L., Breeze, P.S., Drake, N.A., Groucutt, H.S., Jennings, R., Scerri, E.M.L., White, T.S., Zahir, M., Duval, M., Grün, R., Al-Omari, A., Al Murayyi, K.S.M., Zalmout, I.S., Mufarreh, Y.A., Memesh, A.M., Petraglia, M.D., 2016. Middle Pleistocene vertebrate fossils from the Nefud Desert, Saudi Arabia: Implications for biogeography and palaeoecology. Quat. Sci. Rev. 143, 13–36. doi:10.1016/j.quascirev.2016.05.016

1320 Stokes, S., 1992. Optical dating of young (modern) sediments using quartz: Results from a selection of
1321 depositional environments. Quat. Sci. Rev. 11, 153–159. doi:10.1016/0277-3791(92)90057-F

1322 Stokes, S., Bray, H.E., Blum, M.D., 2001. Optical resetting in large drainage basins: Tests of zeroing
1323 assumptions using single-aliquot procedures. Quat. Sci. Rev. 20, 879–885. doi:10.1016/S0277-
1324 3791(00)00045-7

1325 Thatcher, L., Rubin, M., Brown, G.F., 1961. Dating Desert Ground Water. Science (80-.). 134, 105–106.

1326 Thiel, C., Buylaert, J.P., Murray, A., Terhorst, B., Hofer, I., Tsukamoto, S., Frechen, M., 2011a.
1327 Luminescence dating of the Stratzing loess profile (Austria) - Testing the potential of an elevated
1328 temperature post-IR IRSL protocol. Quat. Int. 234, 23–31. doi:10.1016/j.quaint.2010.05.018

1329 Thiel, C., Buylaert, J.P., Murray, A.S., Elmejdoub, N., Jedoui, Y., 2012. A comparison of TT-OSL and post-IR
1330 IRSL dating of coastal deposits on Cap Bon peninsula, north-eastern Tunisia. Quat. Geochronol. 10,
1331 209–217. doi:10.1016/j.quageo.2012.03.010

1332 Thiel, C., Buylaert, J.-P., Murray, A.S., Tsukamoto, S., 2011b. on the Applicability of Post-Ir Irsl Dating To
1333 Japanese Loess. Geochronometria 38, 369–378. doi:10.2478/s13386-011-0043-4

1334 Thomsen, K.J., Murray, A.S., Jain, M., 2011. Stability of IRSL signals from sedimentary K-feldspar samples.
1335 Geochronometria 38, 1–13. doi:10.2478/s13386-011-0003-z

1336 Vogel, J.C., Wintle, A.G., Woodborne, S.M., 1999. FOCUS: Luminescence dating of coastal sands:
1337 overcoming changes in environmental dose rate. J. Archaeol. Sci. 26, 729–733.
1338 doi:10.1006/jasc.1999.0450

1339 Watts, D., Al-Nafie, A.H., 2014. Vegetation and Biogeography of the Sands Seas of Saudi Arabia.
1340 Routledge, London.

1341 Whitney, J.W., Faulkender, D., Rubin, M., 1983. The environmental history and present condition of
1342 Saudi Arabia's northern sand seas. USGS Open-File report 83-749. Environ. Hist. Durh. N. C.

1343 Wintle, a. G., 1973. Anomalous Fading of Thermo-luminescence in Mineral Samples. Nature 245, 143–
1344 144. doi:10.1038/245143a0

1345 Zaidi, F.K., Kassem, O.M.K., Al-Bassam, A.M., Al-Humidan, S., 2015. Factors Governing Groundwater
1346 Chemistry in Paleozoic Sedimentary Aquifers in an Arid Environment : A Case Study from Hail
1347 Province in Saudi Arabia. Arab. J. Sci. Eng. 40, 1977–1985. doi:10.1007/s13369-014-1534-4

1348 Zander, A., Degering, D., Preusser, F., Kasper, H.U., Brückner, H., 2007. Optically stimulated
1349 luminescence dating of sublittoral and intertidal sediments from Dubai, UAE: Radioactive
1350 disequilibria in the uranium decay series. Quat. Geochronol. 2, 123–128.
1351 doi:10.1016/j.quageo.2006.04.003

1352 Zhao, H., Li, S.H., 2002. Luminescence isochron dating: a new approach using different grain sizes.
1353 Radiat. Prot. Dosimetry 101, 333–338.

Ziegler, M., Lourens, L.J., Tuenter, E., Reichart, G.-J., 2010. High Arabian Sea productivity conditions during MIS 13 - odd monsoon event or intensified overturning circulation at the end of the Mid-Pleistocene transition? Clim. Past 6, 63–76. doi:10.5194/cp-6-63-2010

Zimmerman, D.W., 1971. Thermoluminescent dating using fine grains from pottery. Archaeometry 13, 29–52.

Table Captions

Table 1. Radiocarbon dating samples (all collected from section JB1): depths and dating results.

Table 2. Rejection criteria results for aliquots measured for age calculations. A) Quartz, B) Feldspar (dating, residuals, and DRE reported).

Table 3. Equivalent doses measured for all mineral fractions used to calculate luminescence ages.

Table 4. Feldspar equivalent dose measurements and residuals for a) Fading corrected IR_{50} and b) Uncorrected $pIRIR_{290}$ measurements; all samples were collected from site ARY.

Table 5. Values measured for external dose rate estimation and calculated total dose rates via 'standard model.' Dose rates for feldspars include an internal component of 0.63 ± 0.10 Gy ka^{-1} or 0.89 ± 0.15 Gy ka^{-1} for grain sizes 125-180 µm and 180-255 µm, respectively. Samples ARY-OSL2,3,7 are also included as their dose rates have been recalculated via DRAC in order to calculate feldspar residual doses.

Table 6. Ages measured for quartz and feldspar fractions, via standard and isochron methods. Both uncorrected and fading corrected (g-value = 1.84 ± 1.32 %/decade) feldspar $pIRIR_{290}$ ages are included, but uncorrected ages are preferred (see text for discussion).

Figure Captions

Figure 1. [2 column] Landscape and geological setting of studied region. (A) Geological map of the Nefud Desert and surroundings, redrawn from Whitney et al. (1983). (B) Location of the studied sections within the Jubbah basin. Roads, buildings, and center pivot irrigation fields comprising the town of Jubbah now cover the dune-free area.

Figure 2. [1.5 column] Quartz regeneration curves from sample JB1-OSL5, unsaturated (A) and saturated (B). Natural decay curves are shown inset.

Figure 3. [1.5 column] Abanico plots (Dietze et al., 2016) for accepted quartz aliquots from representative Holocene (A, B) and Pleistocene (C, D) samples. These plots combine a radial plot (left) with a kernel density estimate curve ('KDE', right), so that distribution parameters and relationships between error and D_e can be analysed visually. Automatically determined bandwidth ('bw') values used to determine the smoothness of the KDE are given underneath each plot. The central age model D_e for each distribution is shown with a dotted line.

Figure 4. [1.5 column] Feldspar regeneration curves ($pIRIR_{290}$) from sample JB1-OSL13, unsaturated (A) and saturated (B). Natural decay curves are shown inset.

Figure 5. [1.5 column] Abanico plots with accepted aliquot distributions for $pIRIR_{290}$ feldspar measurements: a) MUN-BLEACH13 residuals, b) dose recovery experiment results (normalized to the given dose), and distributions with overdispersion > 40 % (c-f). Central age model D_es (a-f) and minimum age model D_es (c-f, assigned overdispersion=40 %) are indicated with dotted and solid black lines, respectively.

Figure 6. [1.5 column] Accepted quartz aliquot distributions from a) ARY-OSL4 and b) ARY-OSL5, with CAM D_es indicated by the dotted lines.

Figure 7. [1.5 column] Accepted quartz aliquots from section JB3 samples, with CAM D_es indicated by the dotted lines.

Figure 8. [2 column] Stratigraphy, sediment composition, and geochronology for sections ARY (A) and JB3 (B). Unit 1 of JB3 continues below the presented section for 1 m, but it is unvarying and has been cropped for display. Feldspar dates shown for ARY are calculated from the $pIRIR_{290}$ signal (125-180 µm). Note that the depths for site JB3 are in relationship to the undisturbed surface.

Figure 9. [2 column] Stratigraphy, sediment composition, and geochronology for sections JB1 (A) and JB2 (B).

Supplementary Material

Table S1. Details of equipment used to measure luminescence signals. Quartz OSL was measured with both the Risø TL/OSL-DA-15 (Bøtter-Jensen et al., 2000; Bøtter-Jensen et al., 2003) and *lexsyg smart (Richter et al., 2015)*, and all feldspar aliquots were measured with the *lexsyg smart*.

Table S2. SAR protocol parameters used for quartz OSL and feldspar IR_{50}/$pIRIR_{290}$ measurements.

Figure S1. ARY section and dated luminescence sample locations. See Hilbert et al. (2014) for locations of other measured samples.

Figure S2. JB1 section and dated luminescence sample locations: an overview is shown in (A), with approximate locations of detailed views (B-D).

Figure S3. JB2 section and dated luminescence sample locations: overviews of the upper (A) and lower (B) sections, with approximate locations of detailed views (C-F).

Figure S4. JB3 section and dated luminescence sample locations.

Figure S5. Histograms of g-values measured for IR_{50} and $pIRIR_{290}$ signals from ARY aliquots (n=42), with estimates (including uncertainty) for each aliquot displayed in rank order. Negative g-values have been treated as 0 %/decade estimates in the histogram.

Figure S6. Abanico plots displaying accepted feldspar aliquots from ARY samples (125-180 µm, $pIRIR_{290}$ signal). Central age model D_es are indicated via the dotted lines, and expected D_es as calculated from quartz ages are indicated by the blue lines.

Figure S7. MAM D_e as a function of assigned overdispersion (σ = 0.1 – 0. 6) for samples ARY-OSL5 (A) and JB3-OSL2 (B). For each sample, a histogram of obtained D_es is shown to the left, and D_e vs. relative overdispersion to the right.

Figure S8. Sedimentary carbonate content versus uranium concentration (A) and Th/U ratio (B). See text for discussion.

1431 Table 1.

ORAU Sample Code	Sample Type	Depth (m)	Results	
			Uncalibrated (^{14}C years BP)	Calibrated (calBP, 95.4% range)
OxA-30943	Plant fragment (charred)	2.65-2.68	7925 ± 45	8980-8609
P-37215	Plant fragment (charred)	2.58	Failed	NA
P-38476	Bulk Sed.	0.40-0.50	Failed	NA
P-38477	Bulk Sed.	0.85-0.90	Failed	NA
P-38478	Bulk Sed.	3.05-3.15	Failed	NA
P-38479	Bulk Sed.	3.40-3.50	Failed	NA
P-38480	Bulk Sed.	4.26-4.28	Failed	NA

1432

1433

1434 Table 2.

1435 A) Quartz (2 mm aliquots, except where noted)

Field Code	Lab Code	Measured (#)	Signal Strength	Tx err	Zero Ratio	Recycling Ratio	IR depletion	Saturated	Accepted Aliquots (#)
ARY-OSL4[1]	X6141	15		1					14
ARY-OSL5[1]	X6142	15				1	2		12
JB1-OSL1	X6246	18	2	5		1	1		9
JB1-OSL2	X6247	18				3	1		14
JB1-OSL3	X6248	18					3	2	14
JB1-OSL4	X6249	18			2	3	2	3	9
JB2-OSL1	X6216	18		6					12
JB2-OSL2	X6217	18	2	4	1		1		10
JB2-OSL3	X6218	18	2	5					11
JB2-OSL4	X6219	20	3	10					7
JB2-OSL5	X6220	18	1	1	1	2	1	5	7
JB2-OSL9	X6223	18		2			2	3	11
JB3-OSL1	X6231	18			3	1			14
JB3-OSL2	X6232	18				2	2		14
JB3-OSL3	X6233	18					8		10
JB3-OSL4	X6234	18				2	5		11

1436 [1]4 mm aliquots

1437 B) Feldspar (1 mm aliquots)

Field Code	Lab Code	Grain Size (μm)	Measured (#)	Signal Strength	Tx err	Zero Ratio	Recycling Ratio	Saturated	Accepted Aliquots (#) [IR_{50}][1]
ARY-OSL2	X6139	125-180	10			1	[1]		9 [9]
		180-255	6	1 [2]	[2]		[1]		5 [1]
ARY-OSL3	X6140	125-180	10			1	1 [1]		8 [9]
		180-255	10	8 [8][2]					2 [2]
ARY-OSL4	X6141	125-180	10				[1]		10 [9]
		180-255	--						--

ARY-OSL5	X6142	125-180	10			1 [3]	[2]		9 [7]
		180-255	--						--
ARY-OSL7	X6144	125-180	10						10 [10]
		180-255	24	14 [16][2]		3 [1]	1 [1]		6 [6]
JB1-OSL1	X6246	180-255	3	3					0
JB1-OSL2	X6247	180-255	10	1	1	5	1		2
JB1-OSL3	X6248	180-255	10			5	1		5
JB1-OSL4	X6249	180-255	7		1				6
JB1-OSL5	X6250	180-255	10						10
DRE			12		1				11
Residual			6						
JB1-OSL6	X6251	180-255	7	1	1	5			0
JB1-OSL7	X6252	180-255	10					2	8
JB1-OSL8	X6253	180-255	10				1	1	8
JB1-OSL13	X6258	180-255	10		1			4	5
JB2-OSL14	X6228	180-255	8				1	1	6
JB3-OSL4	X6234	180-255	10			4	1		4
MUN13-BLEACH	--	180-255	20				[3]		20 [17]

[1]Aliquots accepted for pIRIR$_{290}$ D_e analysis and IR$_{50}$ analysis were sometimes different populations.

[2]Aliquots were first screened for a measurable natural signal, then those with a signal were measured (in addition to the standard Tx signal strength criterion). This procedure should not affect the measured D_e's, as residual measurements on the modern surface sample indicated that D_e's as low as ca. 1 Gy could be measured with good signal strength.

Table 3.

Field Code	Depth (m)	Quartz			Feldspar		
		Accepted	D_e (Gy)	Overdispersion (%)	Accepted	D_e (Gy)	Overdispersion (%)
ARY-OSL4	0.45	14	9.22 ± 0.50	19.21 ± 4.00			
ARY-OSL5	0.56	12	17.94 ± 2.50[1] (37.19 ± 6.30)	57.32 ± 12.26			
JB1-OSL1	2.50	9	24.94 ± 1.64	13.83 ± 6.09			
JB1-OSL2	2.96	14	21.5 ± 1.07	16.13 ± 4.03	2	93.02 ± 6.12[2]	NA
JB1-OSL3	3.41	14	213.52 ± 16.43	21.38 ± 6.82	5	299.73 ± 43.24	31.37 ± 10.49
JB1-OSL4	4.16	9	288.62 ± 41.24	35.56 ± 11.74	6	376.02 ± 53.82	32.29 ± 10.85
JB1-OSL5	4.51	8	262.49 ± 28.55	26.46 ± 8.74	10	357.06 ± 28.46	19.43 ± 6.79
JB1-OSL7	6.35				8	698.34 ± 149.38	58.08 ± 15.68
JB1-OSL8	5.50				8	302.45 ± 48.79	43.49 ± 11.9
JB1-OSL13	9.00				5	889.16 ± 209.98	47.96 ± 18.18
JB2-OSL1	0.77	12	5.93 ± 0.32	14.43 ± 4.62			
JB2-OSL2	1.57	10	8.52 ± 0.67	21.21 ± 6.39			
JB2-OSL3	3.25	11	5.07 ± 0.26	10.67 ± 4.89			
JB2-OSL4	3.94	7	9.78 ± 0.79	18.24 ± 6.62			
JB2-OSL5	4.15	7	258.26 ± 38.91	35.73 ± 11.83			
JB2-OSL9	5.95	11	236.03 ± 23.01	25.82 ± 8.47			
JB2-OSL14	8.65				6	844.81 ± 189.89	54.11 ± 16.17
JB3-OSL1	1.20	14	61.63 ± 8.79	52.18 ± 10.31			
JB3-OSL2	1.67	14	55.00 ± 6.32[1] (68.44 ± 9.20)	48.08 ± 9.90			
JB3-OSL3	2.07	10	83.60 ± 16.75	62.22 ± 14.42			
JB3-OSL4	2.50	11	94.98 ± 9.64	30.83 ± 7.77	4	224.75 ± 26.87	22.54 ± 8.95

[1]MAM D_e preferred; CAM D_e given in parentheses.

[2]Calculated via weighted mean due to small number of accepted aliquots.

Table 4.

a) IR_{50}

Field Code	Depth (m)	Fading Rate, *g* (% per decade)	Grain Size Fraction: 125-180 µm			Grain Size Fraction: 180-255 µm		
			CAM D_e	Uncorrected Age (ka)	Corrected Age (ka)	CAM D_e	Uncorrected Age (ka)	Corrected Age (ka)
ARY-OSL2	0.87	2.46 ± 0.09	21.25 ± 0.78	10.4 ± 0.7	13.3 ± 0.9	17.00 ± 0.65	7.6 ± 0.6	9.6 ± 0.7
ARY-OSL3	1.07	1.55 ± 0.06	50.19 ± 4.50	15.8 ± 1.6	18.3 ± 1.8	40.41 ± 5.79	12.2 ± 1.9	14.1 ± 2.2
ARY-OSL4	0.45	2.07 ± 0.58	12.49 ± 0.92	5.5 ± 0.5	6.7 ± 0.7			
ARY-OSL5	1.26*	5.40 ± 0.82	43.52 ± 8.52	9.2 ± 1.9	16.3 ± 3.9			
ARY-OSL7	1.80*	3.85 ± 0.13	52.12 ± 2.50	13.5 ± 1.0	20.0 ± 1.5	45.85 ± 11.68	11.7 ± 3.0	17.3 ± 4.8

*Depths measured from stratigraphic zero, rather than from sloped surface directly above (see Figure S1).

b) $pIRIR_{290}$

Field Code	Depth (m)	Grain Size Fraction: 125-180 µm			Grain Size Fraction: 180-255 µm		
		CAM D_e	Overdispersion (%)	Residual	CAM D_e	Overdispersion (%)	Residual
ARY-OSL2	0.87	39.35 ± 2.35	17.8 ± 4.3	18.98 ± 2.86	28.02 ± 4.63	31.0 ± 12.6	5.64 ± 5.04
ARY-OSL3	1.07	80.79 ± 2.73	8.7 ± 2.6	44.87 ± 3.96	68.99 ± 7.23	12.4 ± 8.7	31.5 ± 7.87
ARY-OSL4	0.45	21.38 ± 1.30	18.7 ± 4.4	6.88 ± 1.82			
ARY-OSL5	1.26*	83.95 ± 4.97	16.6 ± 4.4	28.97 ± 6.88			
ARY-OSL7	1.80*	82.67 ± 1.89	5.9 ± 2.0	36.16 ± 5.16	76.42 ± 12.91	40.8 ± 12.1	29.09 ± 13.79

*As note above.

Table 5.

Field Code	K (%)	Th (ppm)	U (ppm)	Water Content		Gamma, Dry (Gy/ka)	Burial Depth (m)	Total Dose Rate (wet)			
				Measured (% of wet)	Burial Avg.			Quartz		Feldspar	
								125-180 µm	180-255 µm	125-180 µm	180-255 µm
ARY-OSL2	0.32	2.85	2.32	0.36	5 ± 3	0.53	0.87		1.26 ± 0.05[2]	2.03 0.12	2.23 ± 0.16
ARY-OSL3	1.08	4.9	4.6	0.79	5 ± 3	0.72	1.07		2.26 ± 0.08[2]	3.18 0.16	3.32 ± 0.18
ARY-OSL4	0.29	0.46	4.09	0.49	5 ± 3	--[1]	0.45		1.44 ± 0.05[2]	2.27 0.13	
ARY-OSL5	0.38	1.97	16.04	0.42	5 ± 3	0.96	0.56		3.32 ± 0.15[2]	4.71 0.32	
ARY-OSL7	0.70	5.03	9.1	0.65	5 ± 3	0.93	1.10		2.74 ± 0.11[2]	3.86 0.21	3.92 ± 0.21
JB1-OSL1	0.04	0.40	41.20	4.35	5 ± 3	0.59	2.50	6.89 ± 0.45			
JB1-OSL2	0.24	6.40	11.60	2.13	5 ± 3	1.18	2.96	3.35 ± 0.15			4.21 ± 0.23
JB1-OSL3	0.25	1.00	45.40	10.88	10 ± 3	2.69	3.41	9.03 ± 0.48			9.82 ± 0.61
JB1-OSL4	0.12	0.60	39.80	1.75	5 ± 3	3.23	4.16	9.2 ± 0.47			9.99 ± 0.60
JB1-OSL5	0.79	3.20	10.00	9.43	10 ± 3	2.11	4.51	4.01 ± 0.16			4.86 ± 0.23
JB1-OSL7	0.43	15.30	35.90	1.53	5 ± 3	2.29	6.35				9.15 ± 0.54
JB1-OSL8	0.29	1.60	2.10	0.42	5 ± 3	0.71	5.50				2.23 ± 0.16
JB1-OSL13	2.39	11.40	3.50	14.32	10 ± 3	1.12	9.00				4.30 ± 0.20
JB2-OSL1	0.03	0.50	2.40	1.80	5 ± 3	0.09	0.77	0.69 ± 0.03			
JB2-OSL2	0.05	<0.1	2.80	1.08	5 ± 3	0.08	1.57	0.71 ± 0.04			
JB2-OSL3	0.02	0.10	1.80	0.66	5 ± 3	0.07	3.25	0.51 ± 0.03			
JB2-OSL4	0.17	3.50	3.60	0.84	5 ± 3	0.30	3.94	1.14 ± 0.05			
JB2-OSL5	0.08	0.20	4.80	1.10	5 ± 3	0.44	4.15	1.32 ± 0.06			
JB2-OSL9	0.48	2.30	7.30	7.72	10 ± 3	1.19	5.95	2.56 ± 0.10			
JB2-OSL14	0.80	3.50	1.30	14.32	10 ± 3	0.66	8.65				2.35 ± 0.16
JB3-OSL1	0.28	1.70	2.40	0.77	5 ± 3	0.31	1.20	1.10 ± 0.04			
JB3-OSL2	0.12	0.60	1.80	0.74	5 ± 3	0.29	1.67	0.83 ± 0.03			
JB3-OSL3	0.07	0.30	2.00	0.75	5 ± 3	0.32	2.07	0.83 ± 0.03			
JB3-OSL4	0.42	3.00	2.50	0.47	5 ± 3	0.36	2.50	1.26 ± 0.05			2.13 ± 0.16

[1]On-site gamma dose rate not available.

[2]Samples etched with hydrofluoric acid according to method in Hilbert et al. (2014), therefore no alpha dose rate included.

Table 6.

Field Code	Depths (m)	Standard Ages (ka)			Isochron Ages[2] (ka)	Average $\dot{D}$[3] (Gy ka^{-1})
		Quartz	Feldspar			
			Uncorrected	Corrected		
ARY-OSL4	0.45	6.4 ± 0.4				
ARY-OSL5	0.56	5.4 ± 0.8[2] (11.2 ± 2.0)				
JB1-OSL1	2.50	3.6 ± 0.3				
JB1-OSL2	2.96	6.4 ± 0.4	22.1 ± 1.9	26.6 ± 4.5	81.9 ± 15.4	0.26 ± 0.05
JB1-OSL3	3.41	23.6 ± 2.2	30.5 ± 4.8	36.8 ± 7.7	111.6 ± 57.4	1.91 ± 0.99
JB1-OSL4	4.16	31.4 ± 4.8	37.6 ± 5.8	45.5 ± 9.8	116.5 ± 80.3	2.48 ± 1.74
JB1-OSL5	4.51	65.4 ± 7.6	73.4 ± 6.8	89.3 ± 16.1	117.1 ± 51.2	2.24 ± 1.01
JB1-OSL7	6.35		76.3 ± 16.9	92.8 ± 26.5		
JB1-OSL8	5.50		135.8 ± 23.9	166.1 ± 38.9		
JB1-OSL13	9.00		206.6 ± 49.7	253.6 ± 74.8		
JB2-OSL1	0.77	8.6 ± 0.6				
JB2-OSL2	1.57	12.0 ± 1.1				
JB2-OSL3	3.25	10.0 ± 0.7				
JB2-OSL4	3.94	8.6 ± 0.8				
JB2-OSL5	4.15	195.2 ± 30.7				
JB2-OSL9	5.95	92.0 ± 9.7				
JB2-OSL14	8.65		359.4 ± 84.3	443.5 ± 135.3		
JB3-OSL1	1.20	56.2 ± 8.3				
JB3-OSL2	1.67	66.3 ± 8.0[2] (82.5 ± 11.6)				
JB3-OSL3	2.07	100.5 ± 20.5				
JB3-OSL4	2.50	75.3 ± 8.1	105.3 ± 14.8	128.5 ± 27.3		

[1]Minimum age model preferred, CAM age given in parentheses.

[2]Calculated based on uncorrected feldspar ages.

[3]Quartz grains, 125-180 µm.

Supplementary Material:

Table S1. Details of equipment used to measure luminescence signals. Quartz OSL was measured with both the Risø TL/OSL-DA-15 (Bøtter-Jensen et al., 2000; Bøtter-Jensen et al., 2003) and *lexsyg smart (Richter et al., 2015)*, and all feldspar aliquots were measured with the *lexsyg smart*.

Facilities	Risø TL/OSL-DA-15	*lexsyg smart*
Irradiation	$^{90}Sr/^{90}Y$ beta source (~0.04 Gy s^{-1})	$^{90}Sr/^{90}Y$ beta source ('flat', ~0.15 Gy s^{-1})
Blue Stimulation	NSPB-500S LEDs, 470Δ20 nm	Unknown type, 458Δ5 nm
Infrared Stimulation	Vishay TSFF 5200 LEDs, 870Δ40 nm	Unknown type, 850Δ20 nm
PMT	EMI Electronics (9235/0158/19747.0020)	Hamamatsu (H7360-02)
Filter Set	Hoya U-340 (7.5 mm)[1]	Hoya U-340 (2.5 mm) + BP 365/50[1] BG 39 (3 mm) + HC414/46[2]

[1]Quartz blue stimulated OSL
[2]Feldspar IRSL

Table S2. SAR protocol parameters used for quartz OSL and feldspar IR_{50}/$pIRIR_{290}$ measurements.

	Mineral	
Regeneration Step	Quartz	Feldspar
1	Irradiation (regeneration only)	Irradiation (regeneration only)
2	Preheat *260 °C (ramp 5 °C s^{-1}, hold 10 s)*	Preheat *320°C (ramp 5°C s^{-1}, hold 60 s)*
3	IRSL (IR depletion step only) *50 °C, 100 s stimulation*	IRSL[2] *50 °C, 200 s stimulation*
4	Blue stimulated OSL[1] *125 °C*	IRSL[2] *290 °C, 200 s stimulation*
5	Irradiation (Test dose)	Irradiation (regeneration only)
6	Preheat *240 °C (ramp 5 °C s^{-1}, hold 10 s)*	Preheat *320°C (ramp 5°C s^{-1}, hold 60 s)*
7	Blue stimulated OSL[1] *125 °C*	IRSL[2] *50 °C, 200 s stimulation*
8	--	IRSL[2] *290 °C, 200 s stimulation*
9	--	IRSL *325 °C, 100 s stimulation*

[1]Risø TL/OSL-DA-15 -- 100 s stimulation, signal: first 1.2 s, background: last 20 s
lexsyg smart -- 60 s stimulation, signal: first 0.2 s, background: last 20 s
[2]*lexsyg smart* -- signal: first 2.0 s, background: last 50 s

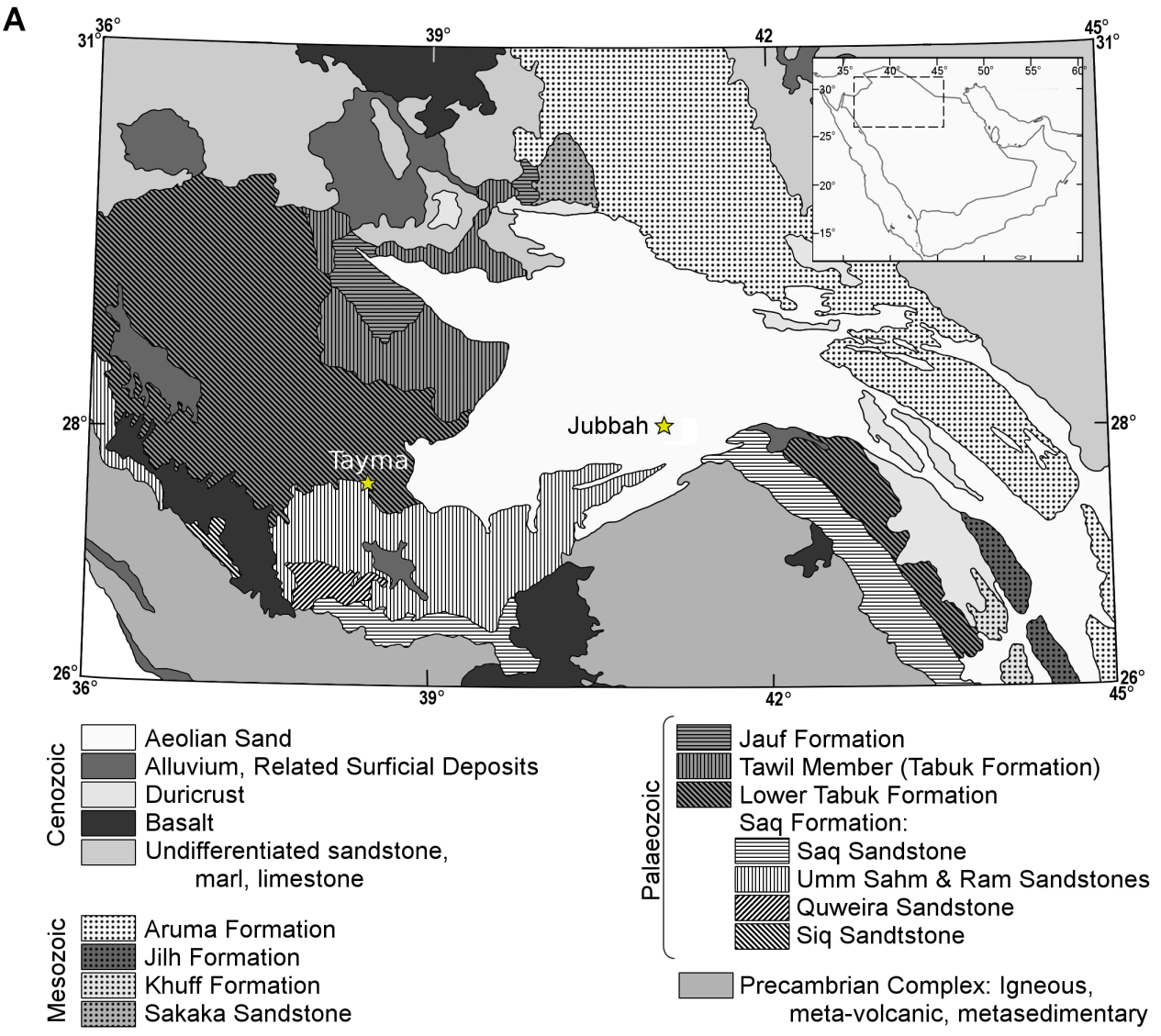
A
36°
39°
42
45°
31°
28°
26°
Jubbah
Tayma
35°
40°
45°
50°
55°
60°
30°
25°
20°
15°
Cenozoic
Aeolian Sand
Alluvium, Related Surficial Deposits
Duricrust
Basalt
Undifferentiated sandstone, marl, limestone
Mesozoic
Aruma Formation
Jilh Formation
Khuff Formation
Sakaka Sandstone
Palaeozoic
Jauf Formation
Tawil Member (Tabuk Formation)
Lower Tabuk Formation
Saq Formation:
Saq Sandstone
Umm Sahm & Ram Sandstones
Quweira Sandstone
Siq Sandtstone
Precambrian Complex: Igneous, meta-volcanic, metasedimentary

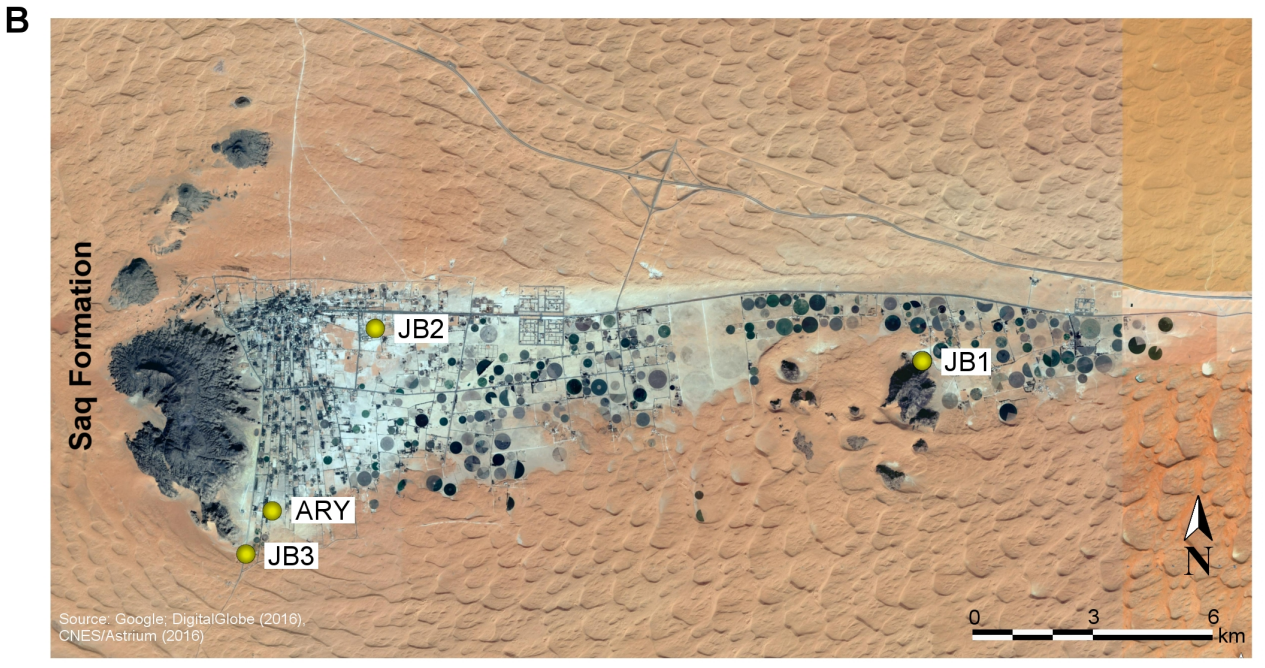
B
Saq Formation
JB2
JB1
ARY
JB3
N
0
3
6
km
Source: Google, DigitalGlobe (2016), CNES/Astrium (2016)

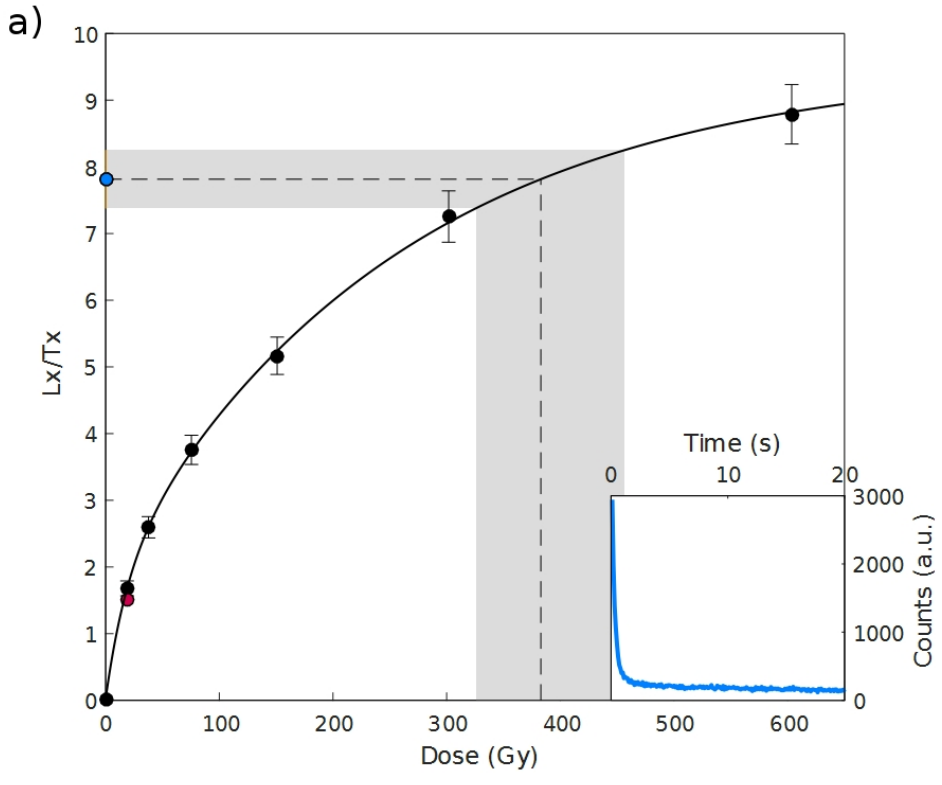
a)
Lx/Tx
Dose (Gy)
Time (s)
Counts (a.u.)

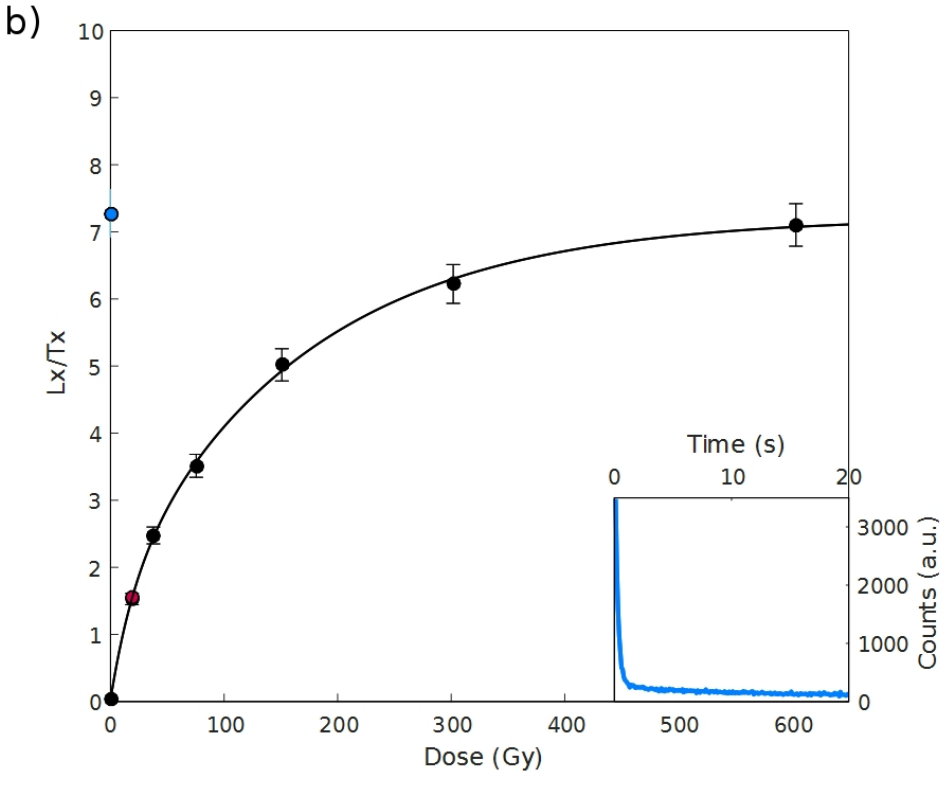
b)
Lx/Tx
Dose (Gy)
Time (s)
Counts (a.u.)

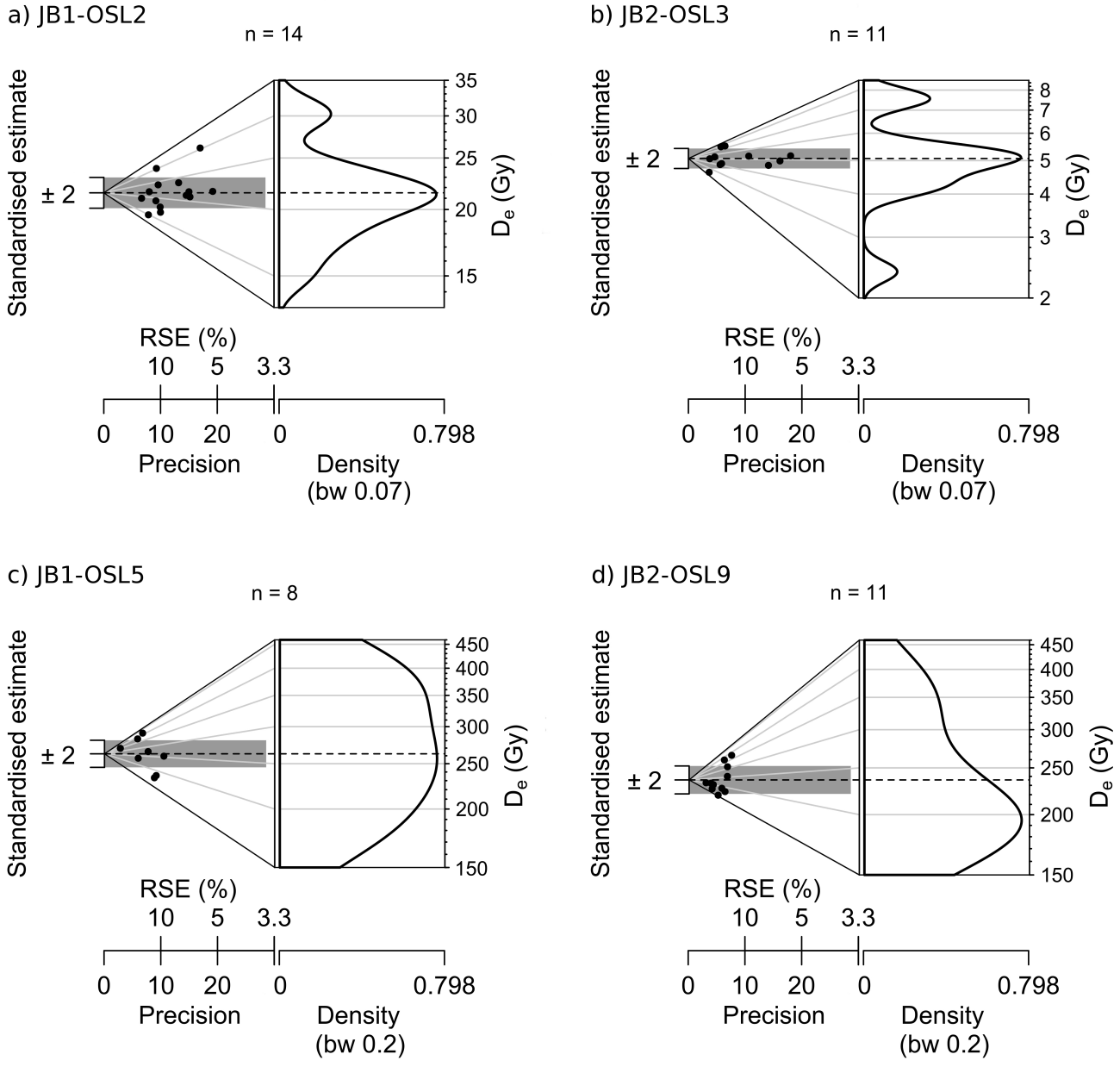
a) JB1-OSL2
n = 14
Standardised estimate
± 2
35
30
25
20
15
De (Gy)
RSE (%)
10
5
3.3
0
10
20
0
0.798
Precision
Density
(bw 0.07)
b) JB2-OSL3
n = 11
Standardised estimate
± 2
8
7
6
5
4
3
2
De (Gy)
RSE (%)
10
5
3.3
0
10
20
0
0.798
Precision
Density
(bw 0.07)
c) JB1-OSL5
n = 8
Standardised estimate
± 2
450
400
350
300
250
200
150
De (Gy)
RSE (%)
10
5
3.3
0
10
20
0
0.798
Precision
Density
(bw 0.2)
d) JB2-OSL9
n = 11
Standardised estimate
± 2
450
400
350
300
250
200
150
De (Gy)
RSE (%)
10
5
3.3
0
10
20
0
0.798
Precision
Density
(bw 0.2)

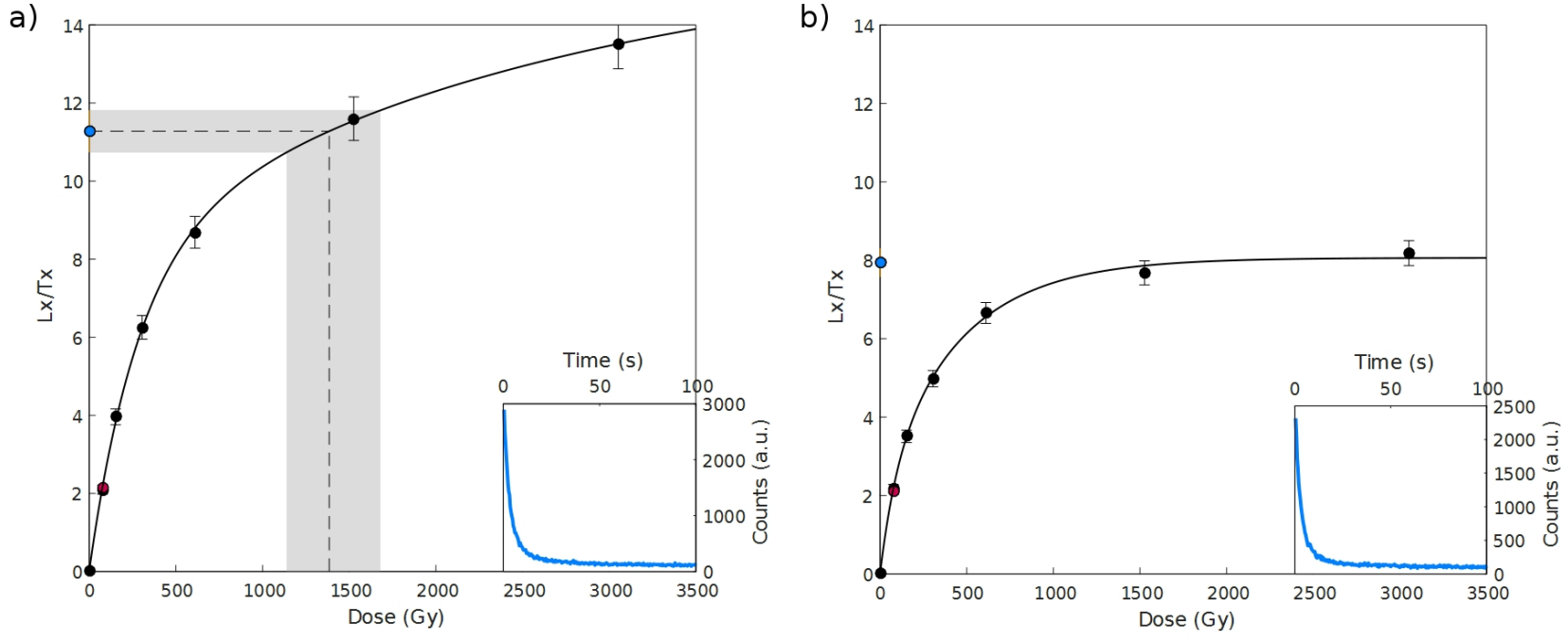
a)
b)
Lx/Tx
Dose (Gy)
Time (s)
Counts (a.u.)

a) Modern aeolian

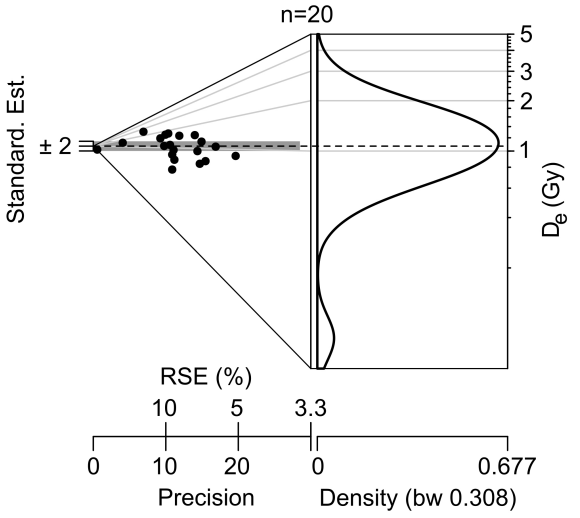

b) Dose Recovery (JB1-OSL5)

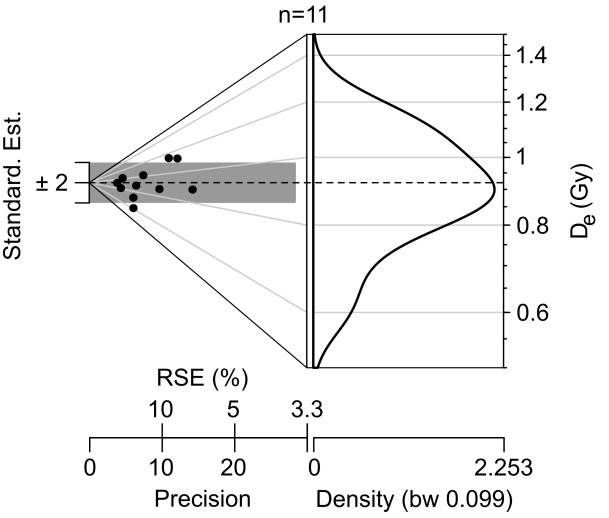

c) JB1-OSL7

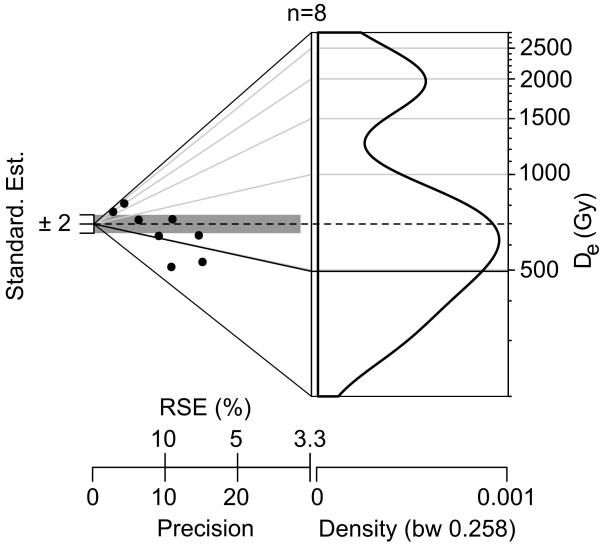

d) JB1-OSL8

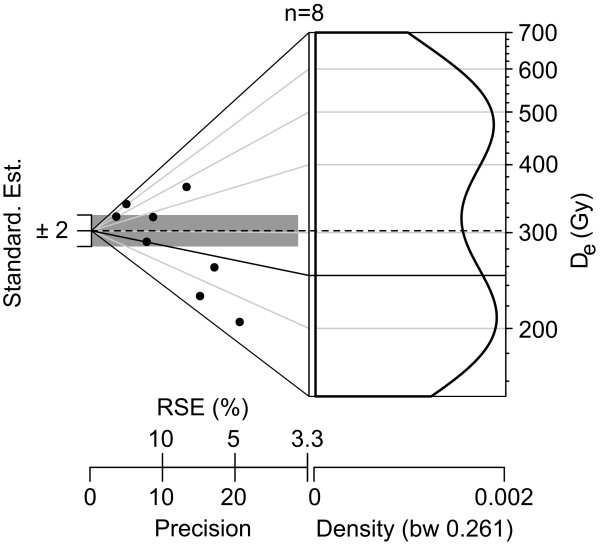

e) JB1-OSL13

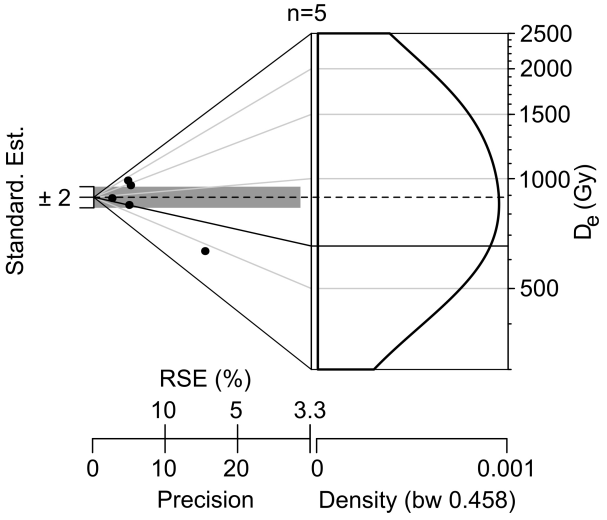

f) JB2-OSL14

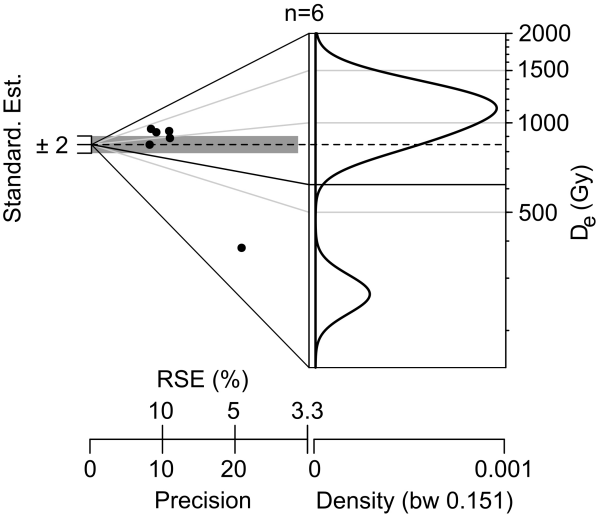

a) ARY-OSL4

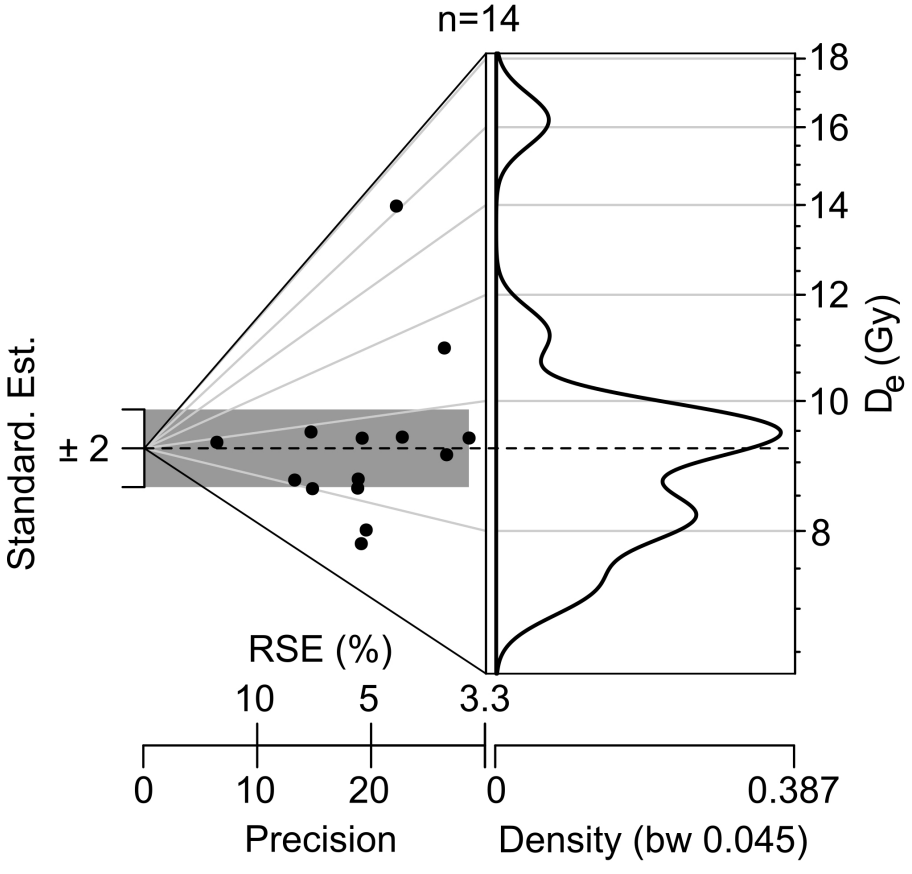

b) ARY-OSL5

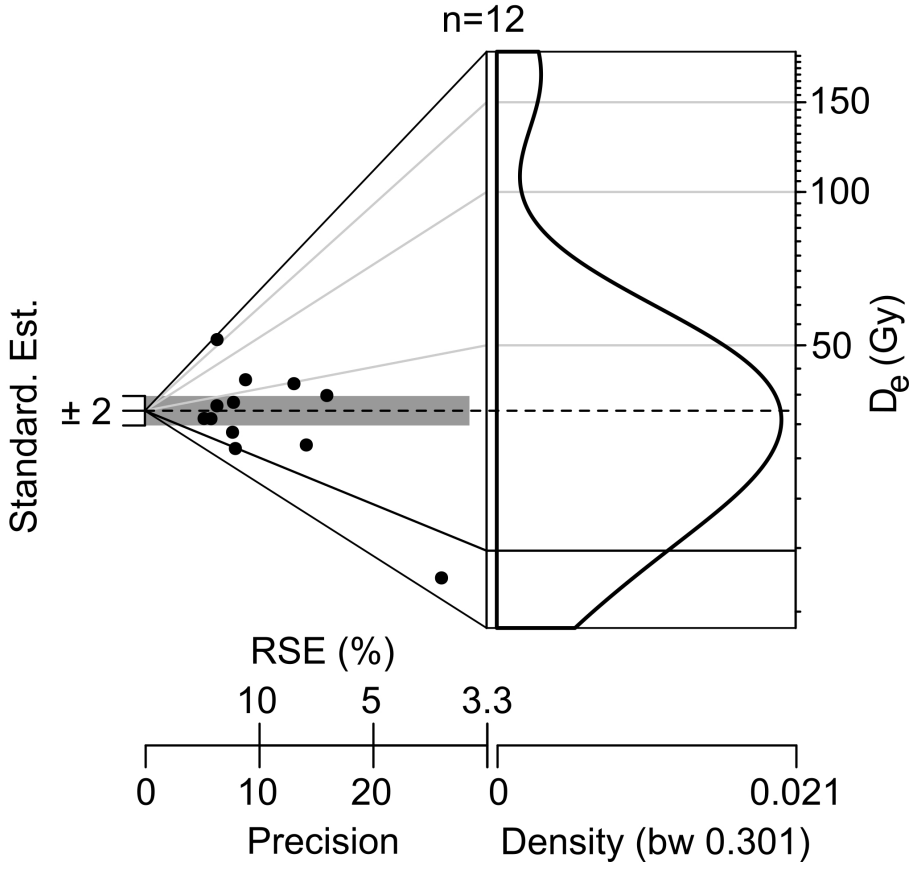

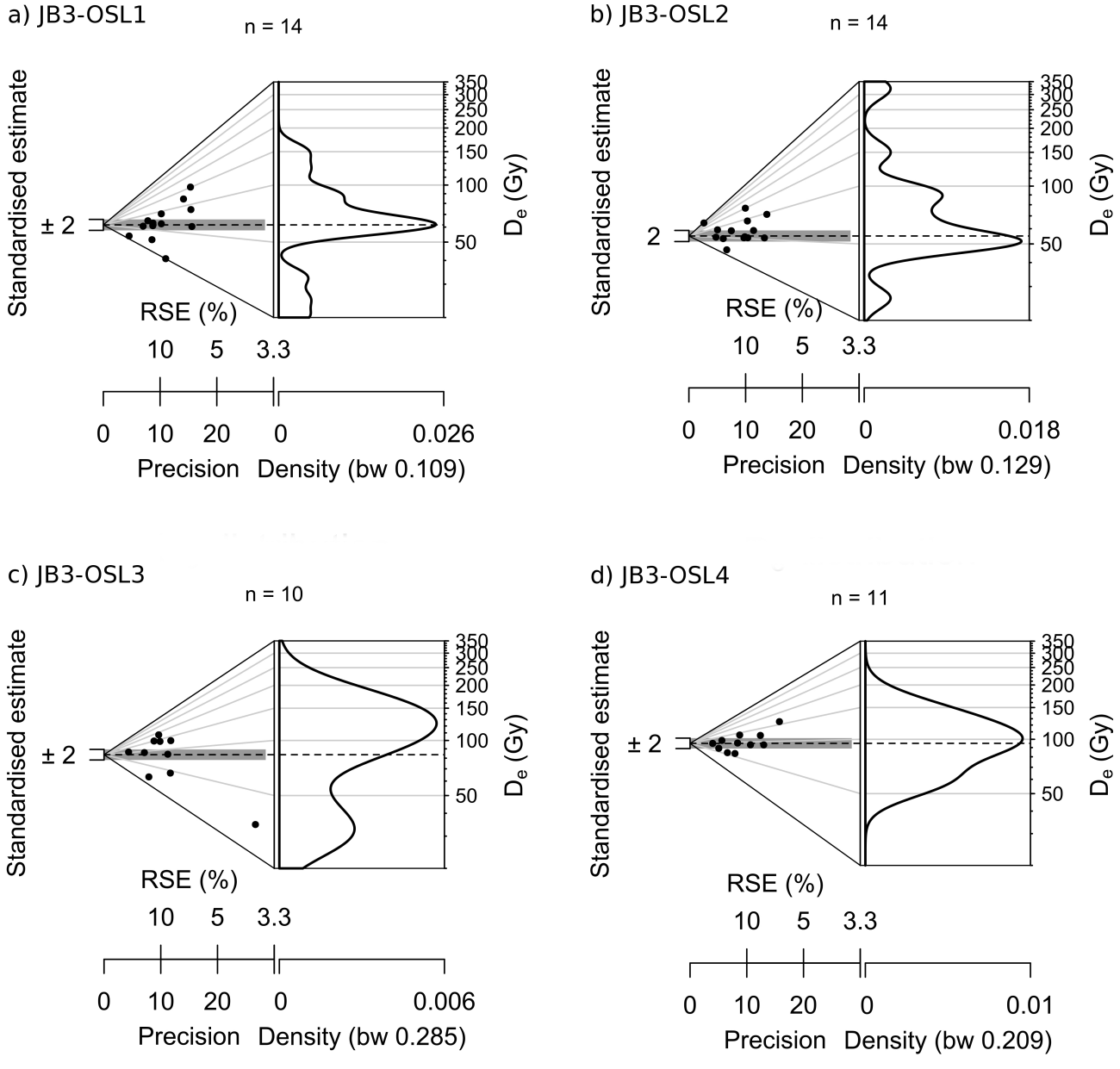
a) JB3-OSL1
n = 14
Standardised estimate
± 2
RSE (%)
10 5 3.3
0 10 20 0 0.026
Precision Density (bw 0.109)
D$_e$ (Gy)
350 300 250 200 150 100 50
b) JB3-OSL2
n = 14
Standardised estimate
2
RSE (%)
10 5 3.3
0 10 20 0 0.018
Precision Density (bw 0.129)
D$_e$ (Gy)
350 300 250 200 150 100 50
c) JB3-OSL3
n = 10
Standardised estimate
± 2
RSE (%)
10 5 3.3
0 10 20 0 0.006
Precision Density (bw 0.285)
D$_e$ (Gy)
350 300 250 200 150 100 50
d) JB3-OSL4
n = 11
Standardised estimate
± 2
RSE (%)
10 5 3.3
0 10 20 0 0.01
Precision Density (bw 0.209)
D$_e$ (Gy)
350 300 250 200 150 100 50

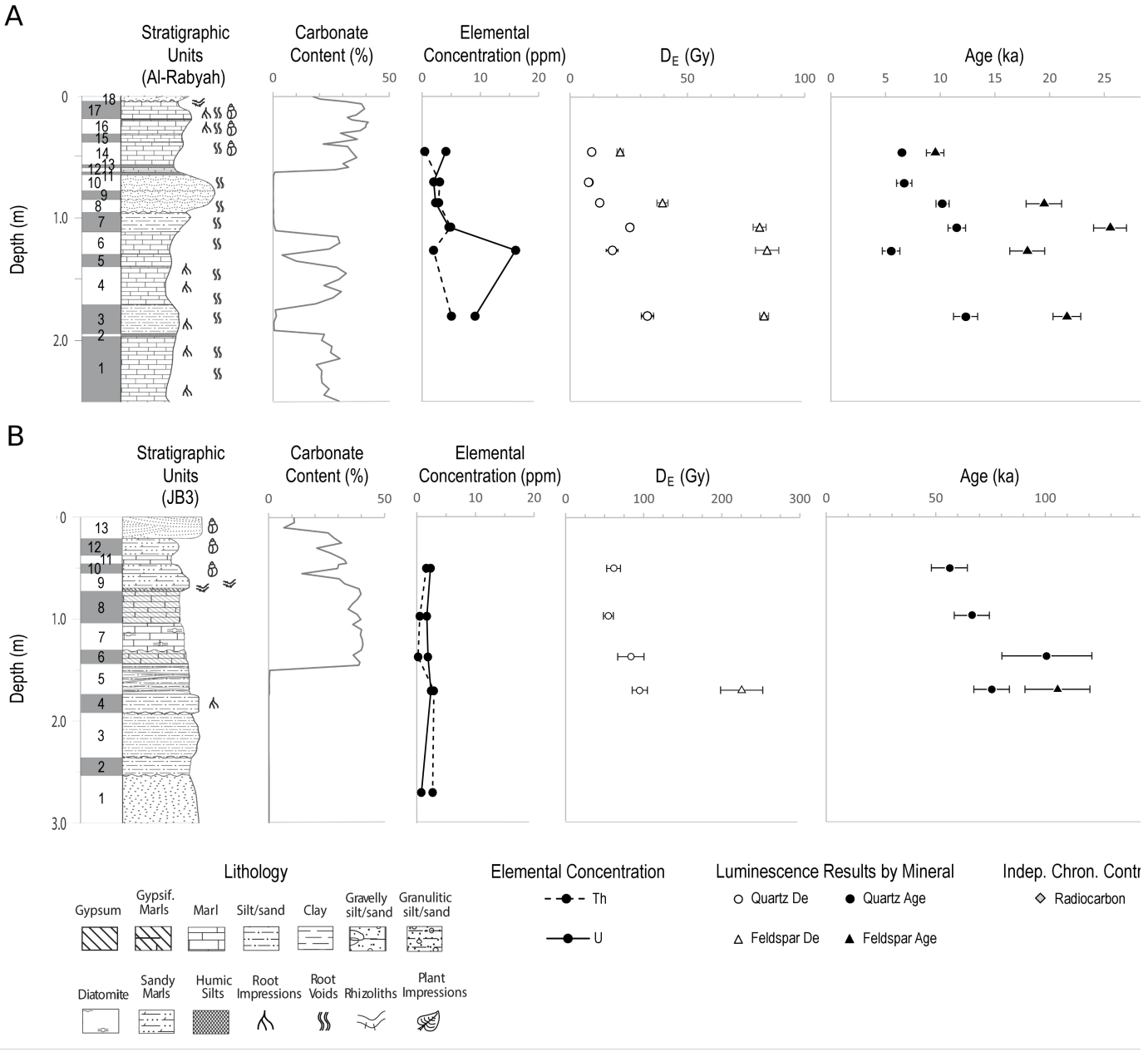
A
Stratigraphic Units (Al-Rabyah)
Carbonate Content (%)
Elemental Concentration (ppm)
D_E (Gy)
Age (ka)
Depth (m)
B
Stratigraphic Units (JB3)
Carbonate Content (%)
Elemental Concentration (ppm)
D_E (Gy)
Age (ka)
Depth (m)
Lithology
Gypsum
Gypsif. Marls
Marl
Silt/sand
Clay
Gravelly silt/sand
Granulitic silt/sand
Diatomite
Sandy Marls
Humic Silts
Root Impressions
Root Voids
Rhizoliths
Plant Impressions
Elemental Concentration
Th
U
Luminescence Results by Mineral
Quartz De
Quartz Age
Feldspar De
Feldspar Age
Indep. Chron. Contr
Radiocarbon

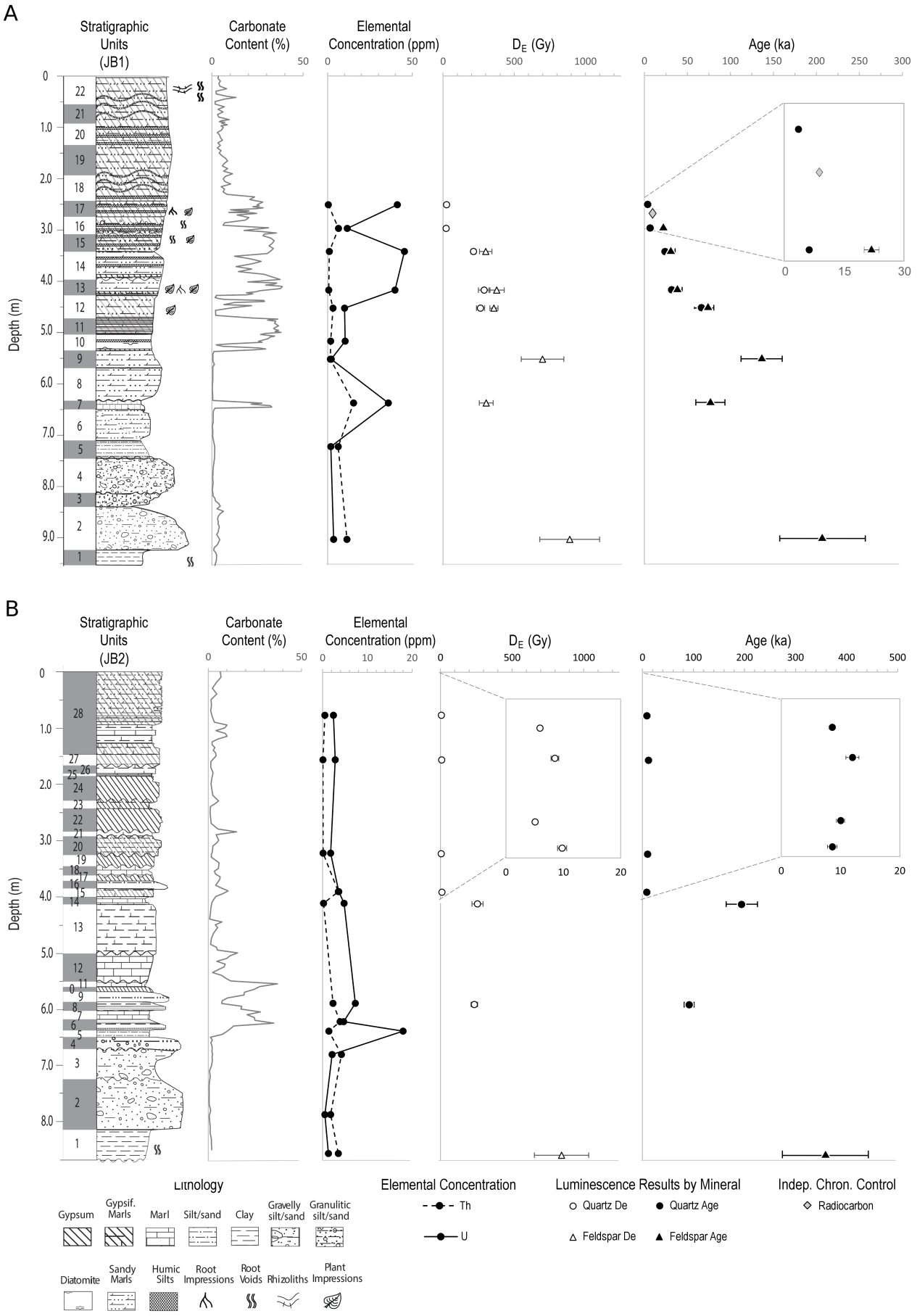
A
Stratigraphic Units (JB1)
Carbonate Content (%)
Elemental Concentration (ppm)
D_E (Gy)
Age (ka)
Depth (m)
B
Stratigraphic Units (JB2)
Carbonate Content (%)
Elemental Concentration (ppm)
D_E (Gy)
Age (ka)
Depth (m)
Lithology
Gypsum
Gypsif. Marls
Marl
Silt/sand
Clay
Gravelly silt/sand
Granulitic silt/sand
Diatomite
Sandy Marls
Humic Silts
Root Impressions
Root Voids
Rhizoliths
Plant Impressions
Elemental Concentration
Th
U
Luminescence Results by Mineral
Quartz De
Quartz Age
Feldspar De
Feldspar Age
Indep. Chron. Control
Radiocarbon


ARY-OSL4
ARY-OSL5

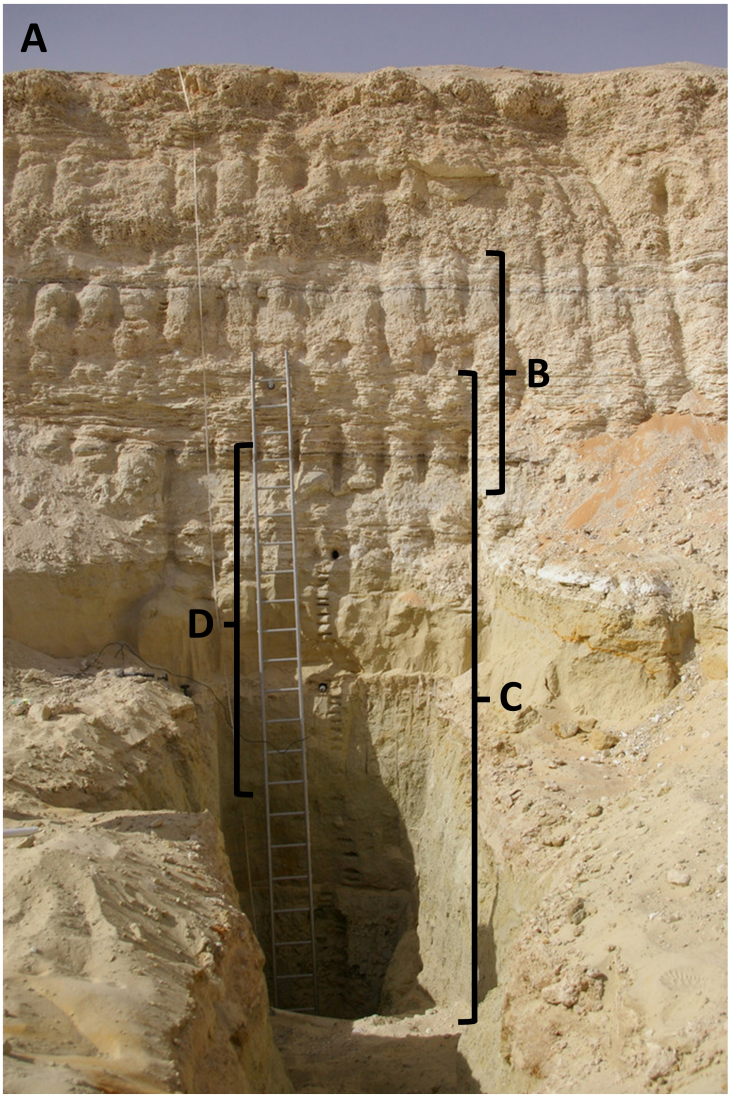
A
B
D
C

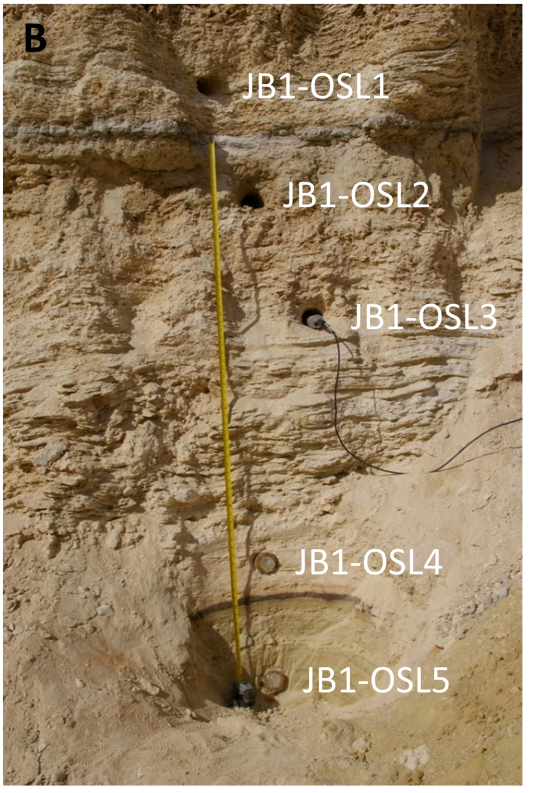
B
JB1-OSL1
JB1-OSL2
JB1-OSL3
JB1-OSL4
JB1-OSL5


C
JB1-OSL8
JB1-OSL7
JB1-OSL11
JB1-OSL13


D
JB1-OSL6
JB1-OSL8
JB1-OSL7

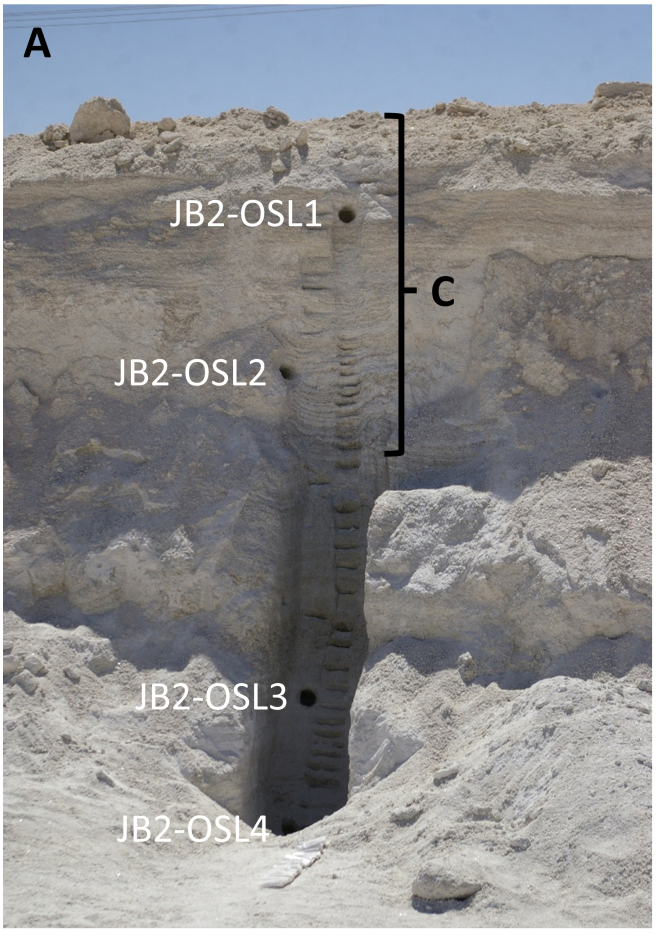
A
JB2-OSL1
C
JB2-OSL2
JB2-OSL3
JB2-OSL4

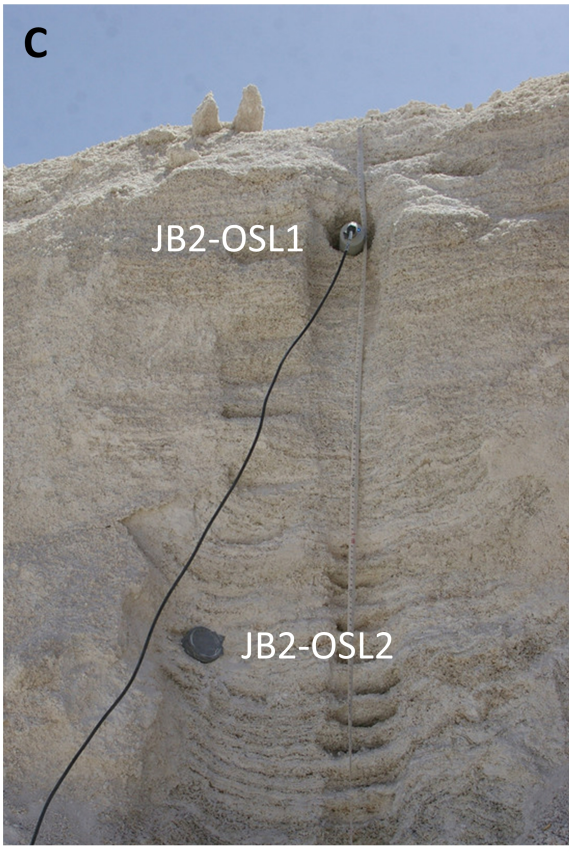
C
JB2-OSL1
JB2-OSL2

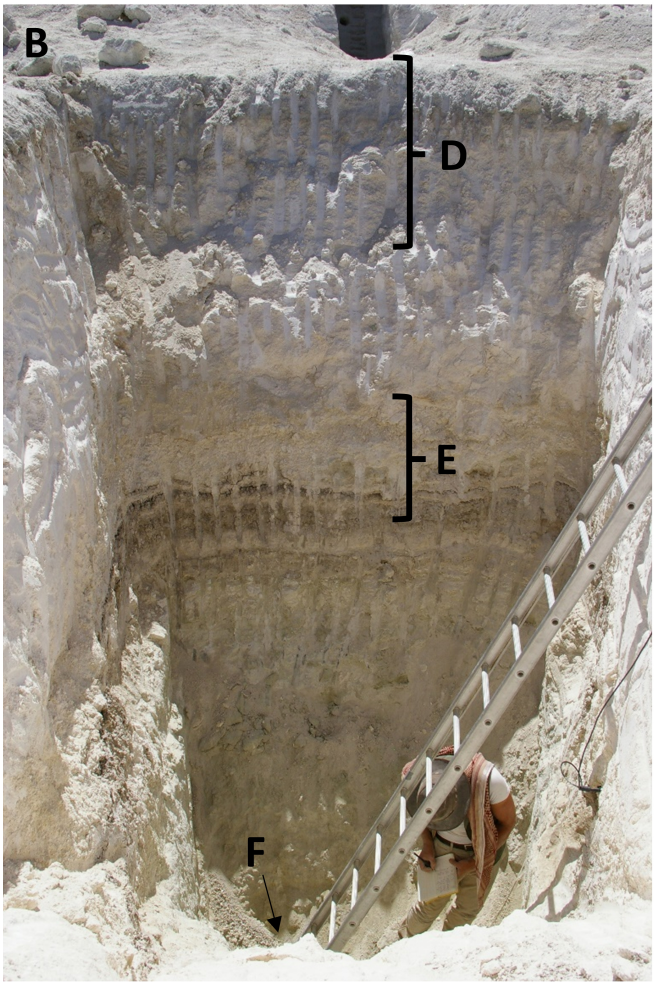
B
D
E
F


D
JB2-OSL5


E
JB2-OSL9


F
JB2-OSL14

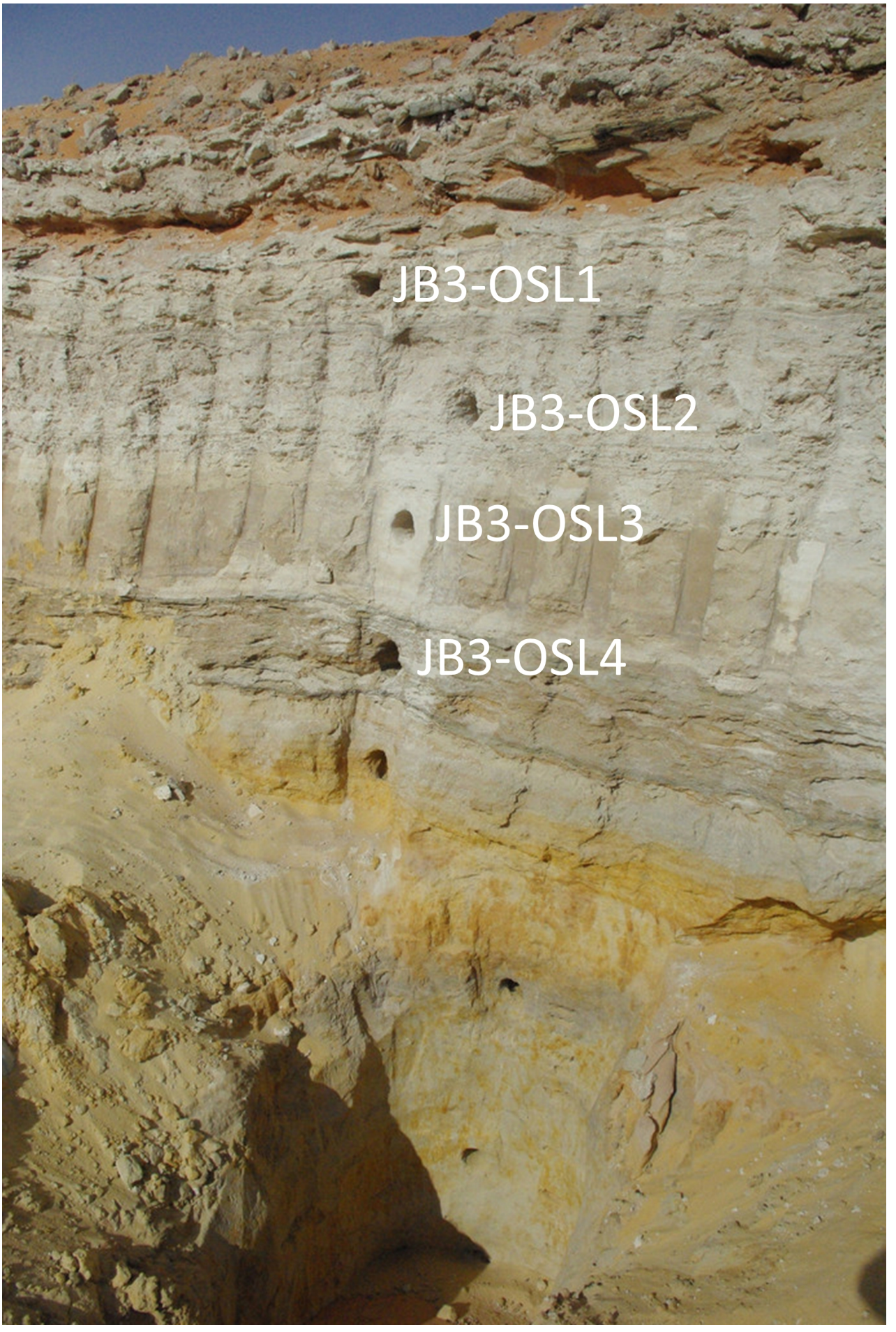
JB3-OSL1
JB3-OSL2
JB3-OSL3
JB3-OSL4

a) ARY-OSL2

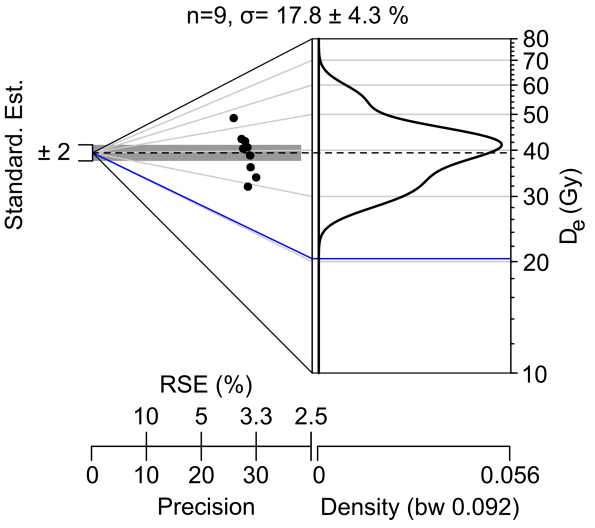

b) ARY-OSL3

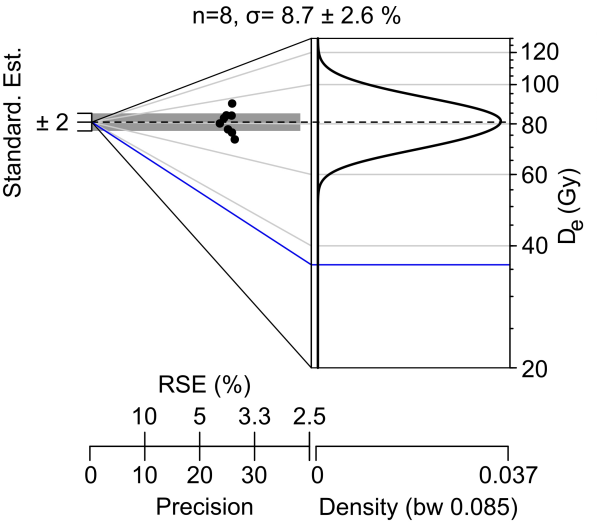

c) ARY-OSL4

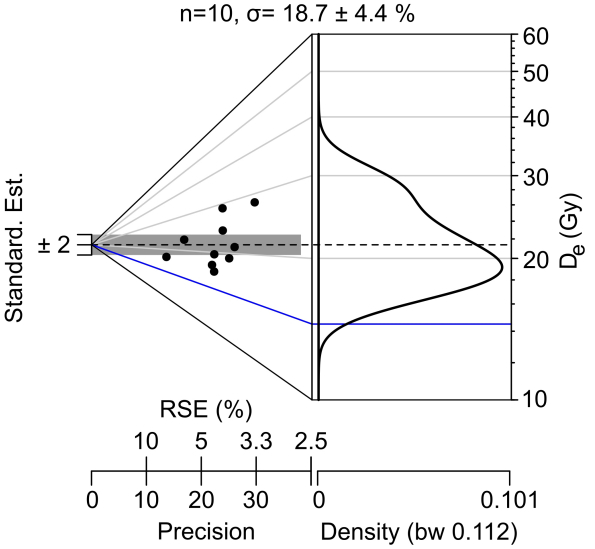

d) ARY-OSL5

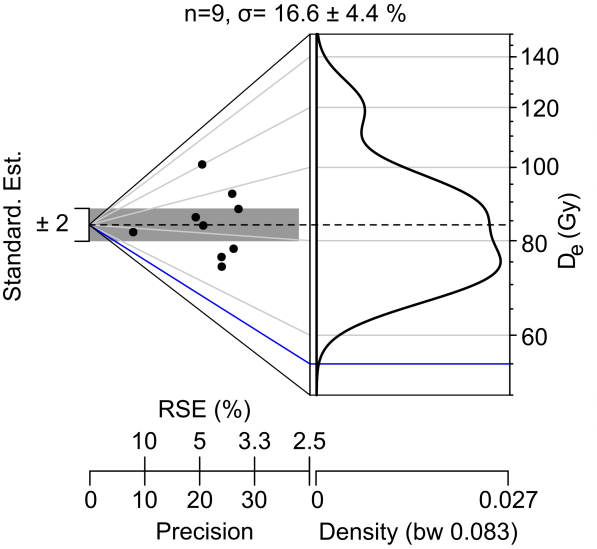

e) ARY-OSL7

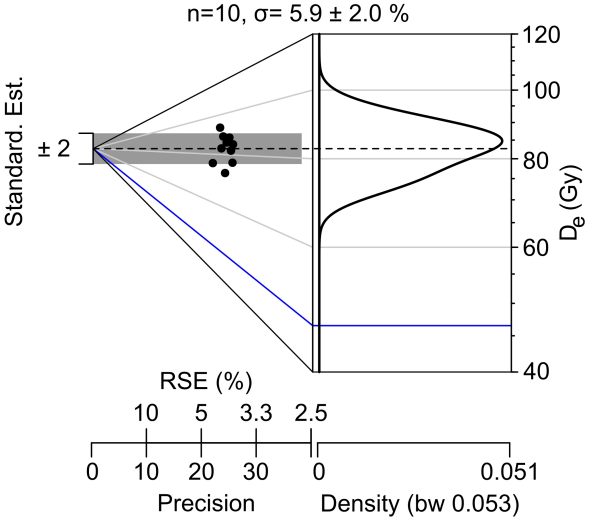

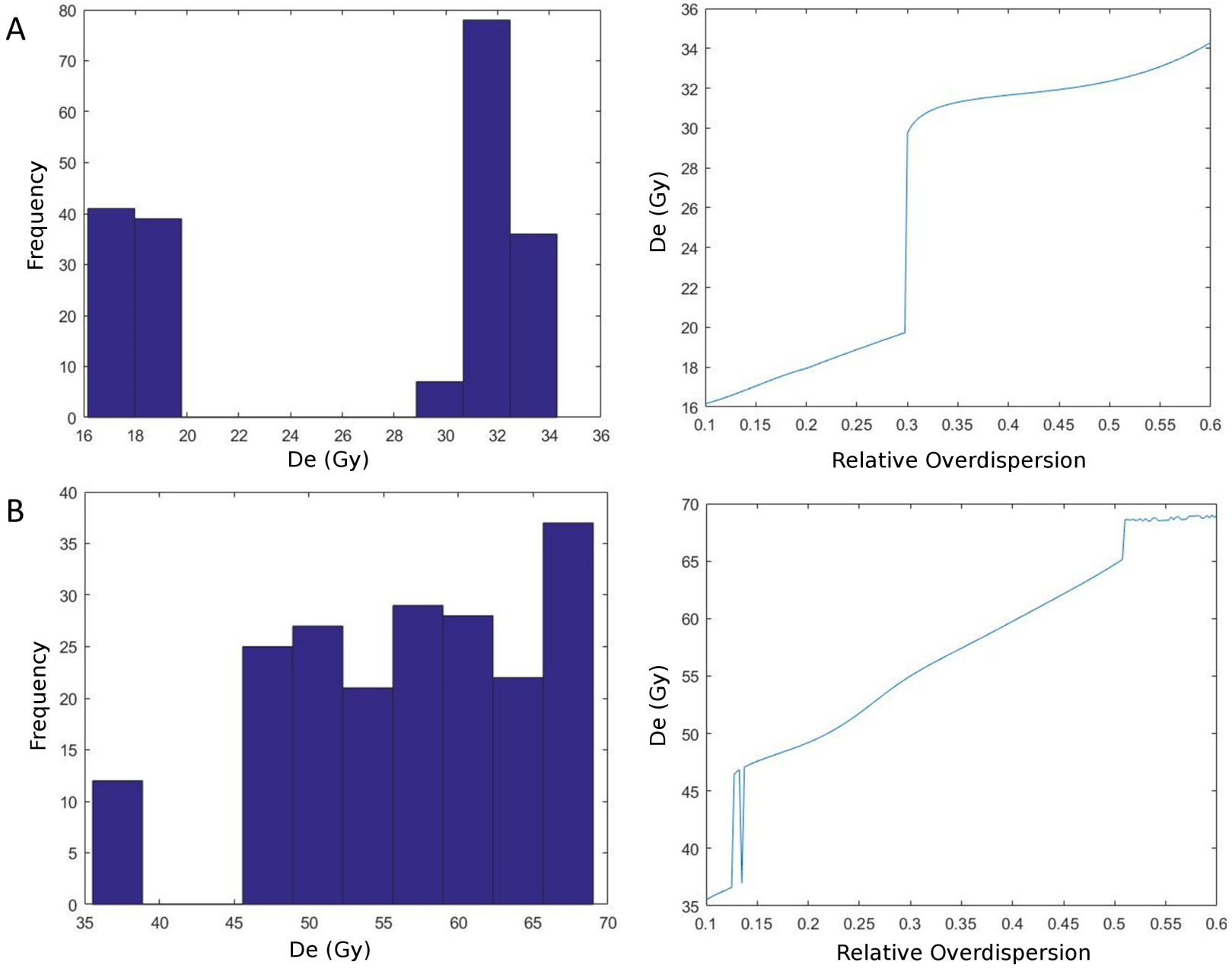
A
Frequency
De (Gy)
De (Gy)
Relative Overdispersion
B
Frequency
De (Gy)
De (Gy)
Relative Overdispersion

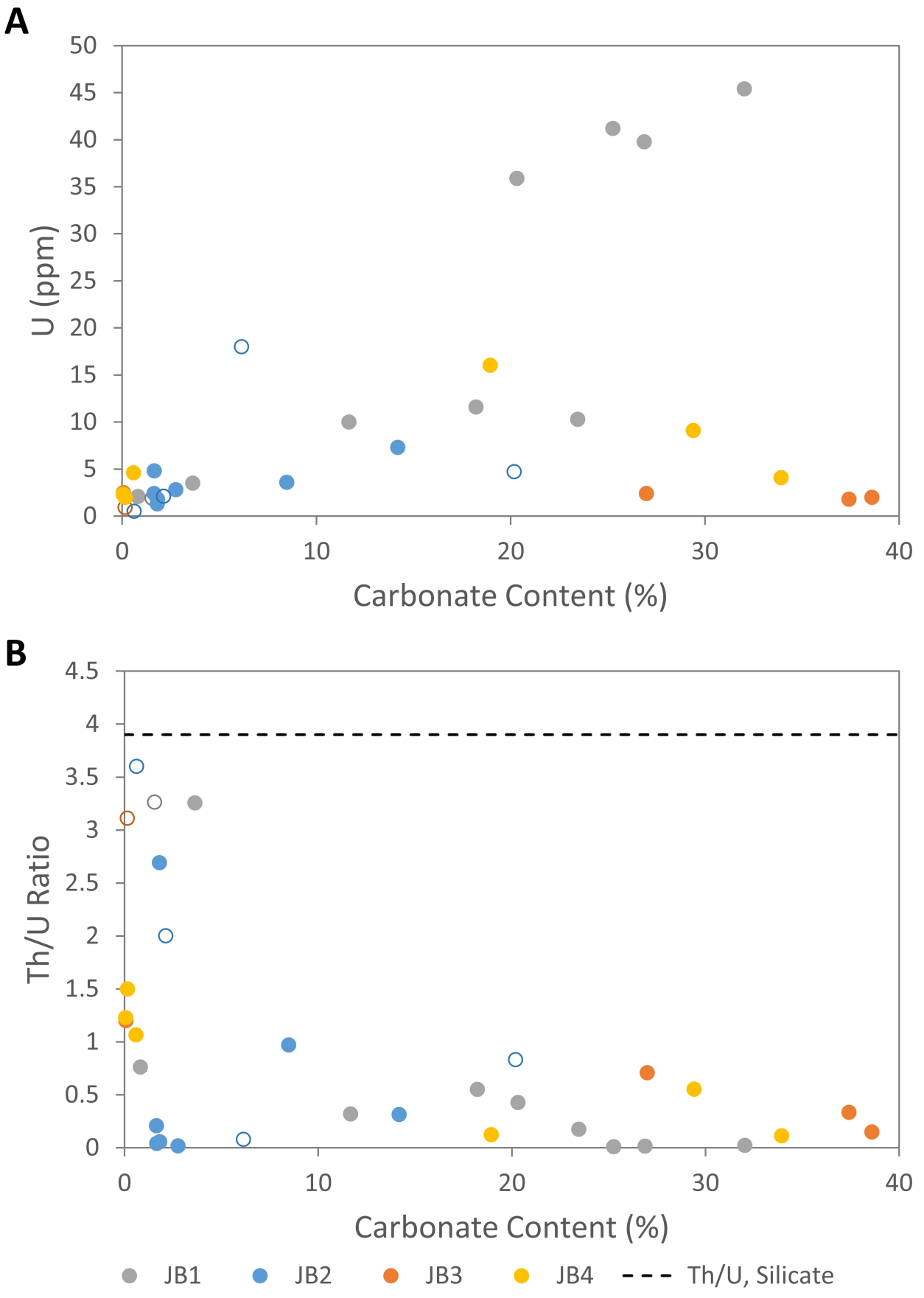
A
U (ppm)
Carbonate Content (%)
B
Th/U Ratio
Carbonate Content (%)
JB1
JB2
JB3
JB4
Th/U, Silicate

a) IR_{50}

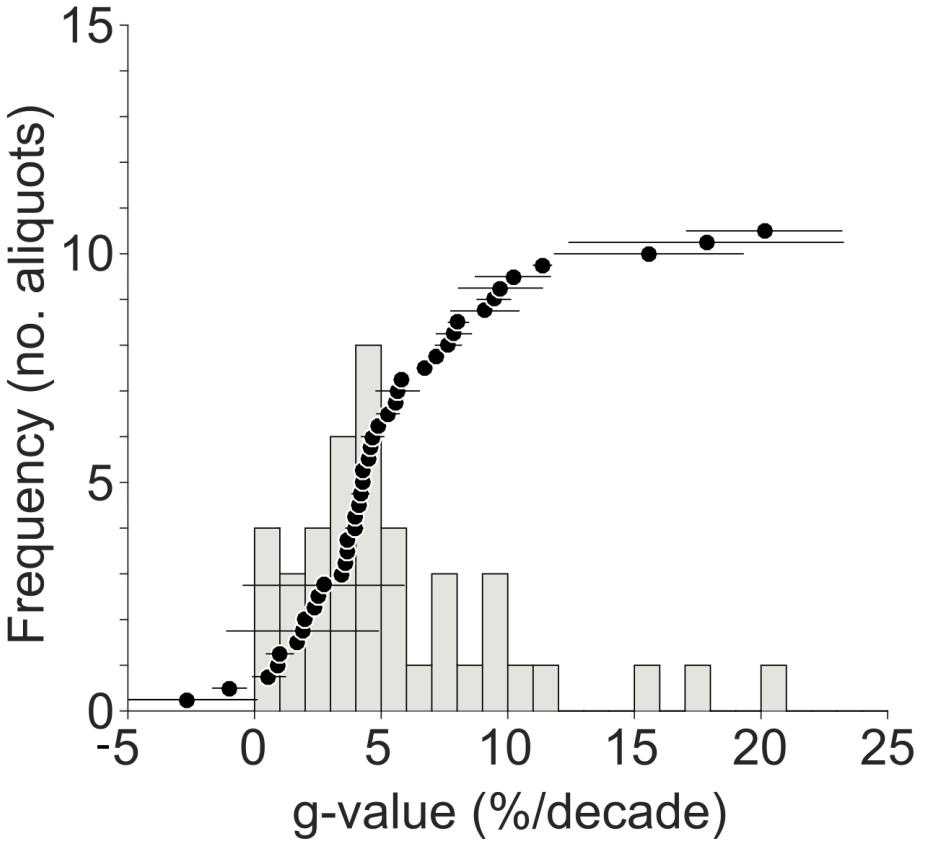

b) $pIRIR_{290}$